



UNIVERSITY OF NAIROBI

**DYE SENSITIZED SOLAR CELLS BASED ON HIGHLY POROUS TiO₂
FILMS**

BY

**DOMTAU DINFA LUKA
I80/97168/2015**

**A Thesis Submitted for Examination in Fulfillment of the Requirements for
the Award of the Degree of Doctor of Philosophy (PhD) in Physics at the
University of Nairobi**

2017

DECLARATION

I declare that this thesis is my original work and has not been submitted elsewhere for examination, award of a degree. Where other people's work or my own work has been used, this has properly been acknowledged and referenced according to the University of Nairobi's policy requirements.

Signature:.......... Date29/09/17.....

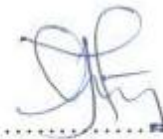
Domtau Dinfa Luka
180/97168/2015
Department of Physics
University of Nairobi

This thesis has been submitted for examination with our approval as supervisors:

Dr. Justus Simiyu
Department of Physics
University of Nairobi

Signature:

Date:



29/9/2017

Dr. Elijah Omollo Ayieta
Department of Physics
University of Nairobi



29.9.2017

Prof. Julius Mwakondo Mwabora
Department of Physics
University of Nairobi



29.9.2017

DEDICATION

This work is dedicated to my Lord and Savior, Jesus Christ for the amazing grace upon my life all through this study. Secondly, to my foster father and uncle, Late Pastor Luka Domtau for his selfless sacrifices for my early education.

ACKNOWLEDGEMENTS

Having given all the glory to God, let me attempt to appreciate people who facilitated the successful completion of this work. First, I am grateful to my supervisors, Dr. Justus Simiyu, Dr. Elijah. O. Ayieta and Professor Julius. M. Mwabora for giving me insights which helped shape and direct my research undertaking right from the proposal stage. I thank you for always making available for me the crucial reading and research materials. You were also patient and tolerant because I could discuss my work with you in your offices or even corridors. Your constant reminder that I needed to get done with research really encouraged and kept me on my toes.

I am greatly indebted to TETFUND and DAAD for the provision of sponsorships for this study. I also appreciate the University of Jos for the study leave and continuous payment of my full salaries. I am thankful to International Science Programme Uppsala, Sweden for the provision of research equipment in the laboratories.

I am so thankful to other members of staff of the Department of Physics at the University of Nairobi. Mr. Boniface Muthoka who took me round the research laboratories on the very first day and explained to me what could be achieved and what could not be. He introduced me to nearly all the people who became very helpful to me in the course of my work. I am indebted to him for his guidance and motivation. I have also had invaluable support from other members of the condensed matter group especially Dr. Robinson J. Musembi and Dr. Sabastian Waita. I also appreciate members of the post graduate committees of the Department of Physics and School of Physical Sciences for their worthy contributions which added value to this research. Mary and Lucy were also wonderful at the Chairman's office. Thank you for your patience.

My colleagues in the condensed matter group were also very helpful. Their day to day observations made on all the results from the laboratory really guided my path. Let me single out Godwin Asimwe who could brave the cold and late nights to assist in one way

or the other in the course of this research. To Victor Odari, Charles Opiyo, John Nguu, Jorim Okoth and Ziporah, I say a big thank you.

The encouragements and support of other people not near the laboratories also worked wonders. My spiritual fathers, Pastors Yakubu Kezi, Josheph Ikechukwu, Victor Adeniji and Precious Umwagbai, I say thank you for the prophecies from the altar and I appreciate your personal declarations over my life. I am equally grateful to Mr. Nansak Nimckak of the University of Jos for the support. I deeply appreciate all the staff of the Department of Physics at the University of Jos for all the support. My very good friend Nannim Nanvyat, you are more than a friend and may God reward you in hundred folds. I appreciate the friendship of Dotun Bobadoye, Denis Ayilah (senior brother), Nimkur Timkat, Dr Nanring Kamdip, Kumchak Densing, Olembe Emmanuel, Babawo Benedict, Hon. Prince Vincent Bulus, Nanpon Dadi, Nanbol Lar, Yohana Madaki, Florence Walbe and Willis Talala. My former Boss, Hon Joyce Ramnap was very supportive and kind hearted.

Finally, I express my profound gratitude to my family: My dear wife, Maureen Singkat Domtau for the shared pressure. I appreciate all the patience, endurance and the good care given to Zhannan and Yinan while I was away. Zhan always called to ask when I was coming back. My mother who gave me every kobo she had since primary school, I love you mama. My brother, Nanman Domtau who labored to pay my fees during undergraduate studies, may God bless you richly. I appreciate my kid sister, Nana Obey and my half-brothers, Thomas John and Danlami John. My cousin, Hon, Bendel Nancwat immensely supported my family while I was away. Thank you sincerely.

ABSTRACT

Light harvesting efficiency in dye sensitized solar cell is currently enhanced by the employment of an additional TiO₂ scattering layer among other means. However, this approach raises the overall photoelectrode thickness hence imposes limitations on effective charge transport especially in dense electrolyte media. The additional film layer further reduces light intensity on the adsorbed dye consequently decreasing photocurrent generation. In light of this, there is still the challenge of light scattering optimization versus charge transport and photocurrent generation. In addition, though TiO₂ is a relatively cheap material, the addition of TiO₂ layer raises the production cost of the dye sensitized solar cell effectively and rendering it not cost effective. In this study, TiO₂ thin films of thicknesses; 3.21, 8.23, 13.52 and 18.93 μm were coated onto FTO/glass by screen printing method, annealed at 500 °C in a tube furnace for 30 minutes in air. Films with same thickness, 3.21 μm were coated with the incorporation of carbon black at varying weight percentages; 0.5, 1.0, 1.5, 2.0 and 3.0 wt % which decomposed upon annealing to create artificial pores in the films. Transmittance and reflectance spectra were measured using a double beam Shimadzu UV-Vis-NIR spectrophotometer in the photon wavelength range of 300-900 nm. The results showed the films to be generally highly transparent in the visible with an average value of 68 % in the wavelength range of 500 and 700 nm. However, transmittance dropped from 79 % at 3.21 μm to 59 % at 18.93 μm . On the other hand, at 400 nm, reflectance rose from 16 % at 3.21 μm to its peak of 27 % at 18.93 μm . Absorbance spectra of the films studied by the UV-Vis-NIR spectrophotometer in the wavelength range of 300-900 nm were relatively low though observed to directly depend on film thickness. At 400 nm, the estimated optical band gap and refractive index rose from 3.49 eV and 1.38 with thickness, 3.21 μm to 3.81 eV and 1.68 with thickness 18.93 μm respectively. With the incorporation of carbon black, average transmittance for film of 0 wt % was 79 % and drastically dropped to an average of 10 % at 3 wt %. The measured absorbance spectra was found to be above the quantity absorbed by bare TiO₂ and the absorption increased all through as the concentration of carbon was increased. It was observed that the presence of artificial pores had no effect on TiO₂ band gap. In another case, refractive index was affected by the porosity of the films. The refractive index of the films increased from 1.35 to 1.60 at 400 nm with carbon black concentrations of 0 wt%

and 3 wt% respectively. Scanning Electron Microscopy (SEM) and Atomic Force Microscopy (AFM) studies revealed a dependence of increasing porosity with increase in the concentrations of carbon black. X-ray diffraction spectroscopy showed the film with and without carbon black to be crystalline and anatase phase. The effects of porosity and film thickness on the electrical properties of TiO₂ thin films were studied. The films were found to be generally conductive and the conductivity depended on the porosity and film thickness. The conductivity ranges from 4.4 to 384.61 Semiens/cm with film thickness ranging from 3.21 to 18.93 μm. Conductivity was observed to decrease as the porosity of the films increased. Resistivity increased from 2.6 x 10⁻³ to 22.63 x 10⁻² Ω.cm as film thick rose to 18.93 μm. Dye Sensitized Solar Cells Sensitized (DSSCs) fabricated with N719 dye and TiO₂ thicknesses; 3.21, 8.23, 13.52 and 18.93 μm were characterized using a solar simulator at 100 mW/cm² solar irradiance. The active area of the cells was 0.48 cm². Current densities, J_{sc} of 5.0, 6.8, 8.2 and 7.5 mA/cm² and open circuit voltage, V_{oc} of 0.731, 0.708, 0.711 and 0.687 V respectively were recorded. The results showed current density to increase as the films became thicker due to increased dye adsorption but decreased at 18.9 μm as a result of reduced light intensity. Therefore the optimum film thickness obtained for DSSCs was 13.52 μm with the maximum conversion efficiency of 3.5 %. A simple experiment to study the effect of reflection on the photovoltaic properties was carried out. Another dye sensitized solar cell was characterized with and without a mirror beneath the cell. Current density of cell improved from 3.65 mA/cm² to 4.81 mA/cm² by placing a mirror behind the platinum (Pt) counter electrode. *I-V* characteristics of DSSCs with varying electrolyte concentrations were also recorded: cells with Redox concentrations of 0.03, 0.1 and 0.15 mol/dm³ had J_{sc} of 8.2, 7.8 and 6.6 mA/cm²; and V_{oc} of 0.734, 0.681 and 0.679 V, respectively. 0.03 mol/dm³ was found to be the optimum electrolyte concentration. The influence of porosity on the photovoltaic performance of DSSC was studied. DSSCs with 0 and 1.5 wt % carbon black were fabricated. The cells had electrode thickness of 13.5 μm, sensitized with N719 ruthenium complex and triiodide electrolyte solution of 0.03 mol/dm³. There was a significant improvement in the photovoltaic performance of the 1.5 wt% DSSC. The cell with 0 wt % of carbon black had J_{sc} and V_{oc} of 8.2 and 0.711 V respectively. In the case of 1.5 wt % based DSSC, J_{sc} and V_{oc} were found to be 9.9 mA/cm² and 0.711 V. The overall cell conversion efficiencies of

0 wt% and 1.5 wt% based DSSCs were 3.5 and 4.3 %, respectively. This represents an increase of 22.8 % in efficiency due to increased photocurrent generation by the artificial pores created by decomposition of carbon black. Finally, the electrochemical impedance spectroscopy of TiO₂ based DSSCs with electrode thicknesses 3.2, 8.2, 13.5 and 18.9 μm were studied. The interfacial reactance at the FTO/TiO₂ interface (R_{FT}) were found to rise as the electrode became thicker due to higher trap sites.

TABLE OF CONTENTS

DECLARATION	Error! Bookmark not defined.
DEDICATION	ii
ACKNOWLEDGEMENTS	iv
ABSTRACT	vi
LIST OF FIGURES	xiii
LIST OF TABLES	xvii
LIST OF PUBLICATIONS	xviii
LIST OF SYMBOLS	xix
LIST OF ABBREVIATIONS	xxiii
LIST OF CHEMICAL FORMULAE	xxv
CHAPTER ONE: INTRODUCTION	1
1.1 Background of study.....	1
1.2 Photovoltaics (PV).....	3
1.2.1 The photovoltaics market	3
1.2.2 Solar cell technologies.....	5
1.3 Problem statement.....	10
1.4 Objective of study.....	10
1.5 Justification and significance of the study	11
CHAPTER TWO: LITERATURE REVIEW	13
2.1 Introduction.....	13
2.2 Historical development of dye-sensitized solar technology	13
2.3 Components of dye sensitized solar cell.....	14
CHAPTER THREE: THEORETICAL BACKGROUND	26
3.1 Introduction.....	26
3.2 Structure and basic components of a dye sensitized solar cell	26
3.3 Operational principles of dye-sensitized solar cell	28
3.4 Electrochemistry of Semiconductor in photovoltaic.....	31

3.4.1	Semiconductor-electrolyte Interface (SEI)	31
3.4.2	Processes of charge transfer at the semiconductor electrolyte interface (SEI).	37
3.4.3	Band bending	37
3.5	Dye sensitization	38
3.6	Electrical characterization	40
3.7	Optical characterization	42
3.7.1	Transmittance and reflectance	42
3.7.2	Absorption	44
3.8	Characterization methods	47
3.8.1	X-ray diffraction (XRD)	47
3.8.2	Current-voltage characterization	49
3.8.2.1	Open-circuit voltage (V_{oc})	51
3.8.2.2	Short-circuit current (I_{sc})	52
3.8.2.3	Fill factor (FF)	52
3.9	Electrochemical impedance spectroscopy	53
 CHAPTER FOUR: EXPERIMENTAL METHODS		56
4.1	Introduction	56
4.2	Samples preparation	57
4.2.1	Preparation of mixed TiO_2 and carbon black paste	57
4.2.2	Thin film preparation	57
4.2.3	Dye preparation	58
4.2.4	Dye characterization	58
4.2.5	Preparation of counter-electrode	58
4.2.6	Complete solar cell assembly	59
4.3	Thin film characterization	60
4.3.1	UV-vis spectroscopy	60
4.3.2	Scanning Electron Microscopy (SEM)	60
4.3.3	Atomic force microscopy (AFM)	61
4.3.4	X-ray diffraction (XRD)	61
4.3.5	Electrical measurements of films for studying resistivity and conductivity	61

4.4 Solar cell characterization.....	62
4.4.1 Current-voltage characterization of complete solar cell.....	62
4.4.2 Electrochemical Impedance Spectroscopy (EIS)	62
CHAPTER FIVE: RESULTS AND DISCUSSIONS	64
5.1 Introduction.....	64
5.2 Optical Characterization	64
5.2.1 Effect of film thickness on the transmittance of TiO ₂ films	64
5.2.2 Effect of porosity on the transmittance of TiO ₂ thin films.....	66
5.2.3 Effect of film thickness on the reflectance of TiO ₂ thin films.....	68
5.2.4 Effect of porosity on UV-vis reflectance of TiO ₂ thin films	70
5.2.5 Effect of film thickness on the UV-vis absorbance of TiO ₂ thin films	72
5.2.6 Effect of porosity on the UV-vis absorbance of TiO ₂ thin films.....	75
5.2.7 Effect of dyes on the UV-vis absorbance of TiO ₂ thin films.....	76
5.2.8 Effect of film thickness on the refractive index of TiO ₂ thin films.....	77
5.2.9 Effect of porosity on the refractive index of TiO ₂ thin films	79
5.2.10 Effect of film thickness on the estimated optical band gap of TiO ₂ thin films	81
5.2.11 Effect of porosity on the optical band gap of TiO ₂ thin films	83
5.3 Electrical Characterization.....	84
5.3.1 Effect of thickness on resistivity and conductivity of TiO ₂ thin film.....	84
5.3.2 Effect of TiO ₂ thin film porosity on resistivity and conductivity	85
5.4 Morphological and structural characterizations.....	87
5.4.1 Morphological characterizations (SEM and AFM)	87
5.4.2 Structural characterizations (XRD).....	92
5.5 Solar cells characterization	93
5.5.1 Effect of film thickness on <i>I-V</i> characteristics of DSSC.....	93
5.5.2 Effect of electrolyte concentration on <i>I-V</i> characteristics of DSSC	96
5.5.3 Effect of light scattering (multi-reflection) on <i>I-V</i> characteristics of DSSC	98
5.6 Electrochemical impedance spectroscopy (EIS) of DSSC	103

CHAPTER SIX: CONCLUSION AND SUGGESTIONS FOR FURTHER STUDIES	105
6.1 Conclusion	105
6.2 Suggestions for Further Studies	108
REFERENCES.....	110
APPENDICES	123
Publication 1	123
Publication 2	130
Publication 3	137

LIST OF FIGURES

Figure 1.1: Global energy demand by fuel type	2
Figure 1.2: Photovoltaic Global capacity, by country 2005-2015	4
Figure 1.3: Solar cell efficiency timeline from 1975 to 2015	9
Figure 2.1: Molecular structure of N3, N719 and N749 (“black dye”) sensitizers	15
Figure 2.2: Incident Photon-to-electron Conversion Efficiency of DSSCs sensitized by N3 and N749 (“black dye”) dyes	16
Figure 2.3: Molecular structures of dyes of varying species of organic sensitizers: a) coumarin, b) indoline, c) cyanine and d) squaraine	17
Figure 3.1: Structure of dye TiO ₂ dye sensitized solar cell	27
Figure 3.2: The operation principle of the dye-sensitized nanostructured solar cell	29
Figure 3.3: Schematic energy diagram of a semiconductor/chromophore interface	30
Figure 3.4: Schematic energy levels diagram for a metal, an insulator and a semiconductor	32
Figure 3.5: Schematic energy diagram of semiconductor-electrolyte interface	34
Figure 3.6: Electrochemical measurement system showing the working electrode (WE), reference electrode (RE) and counter electrode (CE)	35
Figure 3.7: An ideal cyclic voltamogram for a reversible single electrode transfer reaction showing important peak parameters. E_{pc} and E_{pa} are cathodic and anodic peak potentials, respectively while i_{pc} and i_{pa} are cathodic and anodic peak currents respectively	36
Figure 3.8: Band bending at the semiconductor-electrolyte interface for n-type semiconductor	38
Figure 3.9: Dye sensitized semiconductor-electrolyte interface electrode illumination ..	39
Figure 3.10: Simple model of electricity flowing through a material under an applied voltage.	40
Figure 3.11: Model for the four point probe resistivity measurement	41
Figure 3.12: A typical transmission and reflection of a unidirectional beam.....	43
Figure 3.13: Absorption transitions between two direct valleys that are allowed	45
Figure 3.14: Plot of $(ahv)^2$ against (hv) for the estimation of the direct gap energy value	46

Figure 3.15: Plot of $(\alpha hv)^{1/2}$ against (hv) for the estimation of the indirect gap energy value .	47
Figure 3.16: A typical I - V curve showing variation of current with voltage and corresponding power curve .	51
Figure 3.17: An equivalent circuit for a solar cell showing the series (R_s) and shunt (R_{sh}) resistances.	53
Figure 4.1: Fabrication process of complete DSSC unit cell	59
Figure 4.2: Schematic Diagram of Electrochemical Impedance Spectroscopy Set Up	63
Figure 5.1: UV-Vis transmittance spectra of screen printed TiO_2 thin films at thicknesses of 3.21, 8.23, 13.52 and 18.93 μm from 300-900 nm.	65
Figure 5.2: Variation of transmittance spectra with film thickness at wavelengths of 600 and 850 nm	66
Figure 5.3: UV-Vis transmittance versus wavelength spectra of screen printed TiO_2 thin films (3.21 μm) at varying carbon black concentrations (i.e. 0, 0.5, 1.0, 1.5, 2.0 and 3.0 wt %) from 300-900 nm.	67
Figure 5.4: Variation of transmittance with carbon black concentrations at wavelengths of 600 and 850 nm for TiO_2 thin films (3.21 μm)	68
Figure 5.5: UV-Vis reflectance versus wavelength spectra of bare TiO_2 thin films for various thicknesses	69
Figure 5.6: Variation of reflectance with film thickness at the wavelengths of 400 and 800 nm.	70
Figure 5.7: Variations of reflectance with wavelength spectra for TiO_2 thin films (3.21 μm) with varying wt % carbon black concentrations (0, 0.5, 1.0, 1.5, 2.0 and 3.0 wt %).	71
Figure 5.8: Variation of the reflectance with wt % of carbon black concentrations for TiO_2 thin films (3.21 μm) with carbon black concentrations at wavelengths of 400 and 800 nm.	72
Figure 5.10: Absorbance versus wavelength spectra for dye (N719) sensitized TiO_2 thin films at different film thicknesses.	74
Figure 5.11: Variation of absorbance with film thickness for dye sensitized TiO_2 films at 400 and 800 nm	75

Figure 5.12: Absorbance versus wavelength spectra for TiO ₂ thin films (3.21 μm) at different concentrations of carbon black.	76
Figure 5.13: Absorbance versus wavelength spectra of bare TiO ₂ , N719 sensitized and N749 sensitized TiO ₂ thin films (13.5 μm)	77
Figure 5.14: Refractive index versus wavelength for TiO ₂ thin films at different thicknesses obtained from MATLAB model.	78
Figure 5.15: Refractive index versus wavelength for TiO ₂ thin films at varying carbon black concentrations obtained from a MATLAB model.	80
Figure 5.16: Variation of Estimated optical band gap with TiO ₂ film thickness.....	81
Figure 5.17: Estimated optical band gaps of TiO ₂ thin films at varying wt % carbon black	83
Figure 5.18: Resistivity and conductivity for TiO ₂ thin films of various thicknesses	85
Figure 5.19: Resistivity and conductivity of TiO ₂ thin films (3.21 μm) with different wt% of carbon black	86
Figure 5.21: SEM micrographs for TiO ₂ thin films with (a) 0, (b) 0.5, (c) 1.0, (d) 1.5, (e) 2.0 and (f) 3 wt% carbon black.	89
Figure 5.23: AFM images of TiO ₂ thin films at varying wt % carbon black: (a) 0, (b) 0.5, (c) 1.0, (d) 1.5, (e) 2.0 and (f) 3.0.....	91
Figure 5.24: X-Ray diffraction pattern for TiO ₂ thin films (13.52) at 0 and 1.5 wt% carbon black	92
Figure 5.25: J-V characteristics for DSSC at varying film thickness.	94
Figure 5.26: Dependence of photovoltaic parameters; J_{sc} , V_{oc} , FF and η on film thickness	95
Figure 5.27: J-V characteristics for DSSC at different redox (I^-/I_3^-) concentrations.	96
Figure 5.28: Dependence of J_{sc} and V_{oc} on the redox (I^-/I_3^-) concentration in iodide/tri-iodide electrolyte	98
Figure 5.29: J-V characteristics for DSSC with and without reflection	99
Figure 5.30: J-V characteristics for DSSC at varying concentrations of carbon black... ..	101
Figure 5.31: Dependence of cell efficiency on the porosity of films.....	102
Figure 5.32: J-V characteristics for the best 0 wt% and 1.5 wt% carbon black based TiO ₂ DSSCs	103

Figure 5.33: Nyquist plots of DSSCs based on film electrodes of different thicknesses.

..... 104

LIST OF TABLES

Table 5.1: Dependence of refractive index on film thickness at wavelengths of 400, 500, 600, 700 and 800 nm.....	79
Table 5.2: Refractive index versus wavelength for TiO ₂ thin films (3.21 μm) of different carbon black concentrations at 400, 500, 600, 700 and 800 nm.	80
Table 5.3: Variation of estimated optical band gap of TiO ₂ with film thickness	82
Table 5.4: Resistivity and conductivity dependence on film thickness of TiO ₂ thin films	84
Table 5.5: Resistivity and conductivity of TiO ₂ thin films (3.21 μm) with varying wt% carbon black	86
Table 5.6: Table showing peak list and particle size for TiO ₂ film	93
Table 5.7: Cell parameters dependence on film thicknesses	94
Table 5.8: Photovoltaic parameters versus redox (I ⁻ /I ₃ ⁻) concentration in iodide/tri-iodide electrolyte.....	97
Table 5.9: Dependence of cell parameters on multiple light scattering.....	99
Table 5.10: Parameters for DSSC at varying films pore size	101
Table 5.11: Photovoltaic parameters for best DSSCs with and without carbon black ...	102

LIST OF PUBLICATIONS

- I. Effects of Film Thickness and Electrolyte Concentration on the Photovoltaic Performance of TiO₂ Thin Films. *Surface Reviews and Letters*, 24, 5(2016) doi: 10.1142/S0218625X17500652
- II. Influence of Pore Size on the Optical and Electrical Properties of Screen Printed TiO₂ Thin Films, *Advances in Materials Science and Engineering*, vol. 2016, Article ID 7515802, 7 pages, 2016. doi:10.1155/2016/7515802.
- III. Optical and Electrical Properties Dependence on Thickness of Screen-Printed TiO₂ Thin Films. *Journal of Materials Physics and Chemistry*. Vol. 4, No. 1, 2016, pp. 1-3. <http://pubs.sciepub.com/jmpc/4/1/1>.

LIST OF SYMBOLS

e^-	charge of an electron
$\Delta\Phi_{sc}$	total band bending at the semiconductor-electrolyte interface
μm	Micrometer
μs	Microsecond
A	area of cell exposed to light
c	speed of light in air
C_i	concentration species i in a solution
c_o	speed of light in the atmosphere
C_{ox}	concentration of oxidation species
C_{red}	concentration of reduction species
D	film thickness
de_γ	energy density
d_{hkl}	crystal's inter-planar spacing
D_i	diffusion coefficient
$d\Omega$	solid angle element
E	energy of states
E^0	standard redox potential
E_B^V	electron binding energy
E_c	energy of conduction band
E_f	energy of Fermi level
$E_{f,redox}$	Fermi level of the redox electrolyte
E_K	kinetic energy of the emitted electron
E_{pa}	anodic peak potential
E_{pc}	cathodic peak potential
E_v	energy of the valence band
$F(E)$	Fermi-Dirac distribution function
H	Plank's constant

$H\nu$	energy of an electron or photon
I	current
I_{dark}	dark current
I_{mp}	current at maximum power point
I_{pa}	anodic peak current
I_{pc}	cathodic peak current
I_{ph}	photogenerated current
I_s	saturation current
I_{sc}	short circuit current
$J_i(x)$	flux of species i
J_{sc}	short circuit photocurrent density
k_B	Boltzmann's constant
L	diffusion length
l	radiation path length
L_D	Debye length
l_o	thickness of the atmosphere
M	ideality factor
m^*_{dos}	effective electron mass
Ms	Millisecond
$N(E)$	density of states
N_c	effective density of conduction band states
n_c	density of electron in conduction band
N_D	density of donor states
N_e	distribution of states
nm	Nanometer
nE_f	quasi Fermi level of electrons under illumination
$N_{electrons}$	number of electrons
$N_{photons}$	number of photons

N_s	Nanosecond
$N_{trap}(E)$	density of trap states
O_x	oxidized species
P_{in}	power of incident radiation
P_{max}	Maximum
P_s	Picosecond
Q	quantity of charge
Q_{oc}	charge accumulation at open circuit
Q_{photo}	photogenerated charge
Q_{trap}	charge residing in trap states
R	crystal radius
R_{FT}	charge transfer resistance at FTO/TiO ₂ interface
R_s	series resistance
R_{sh}	shunt resistance
R_{TDE}	charge transfer resistance at FTO /dye/electrode interface
S	dye molecule in ground state
s	Second
S^*	dye molecule in excited state
S^+	dye molecule in oxidized
S_i	instrument broadening constant for x-ray diffractometer temperature
T	Temperature
t_e	electron lifetime
t_{max}	time it takes for a v_{sc} to rise to a maximum value
t_{rec}	time constants recombination
t_{tr}	time constant for transport
V	applied voltage or bias potential
$v(x)$	velocity with which a volume element in a solution moves along the axis

V_{mp}	voltage at maximum power
V_{oc}	open circuit voltage
V_T	thermal voltage
Z_i	charge on the species i
A	incident angle of sun's radiation relative to the earth's surface
B	constant representing exponential power in open circuit decay
E	dielectric constant of a material
ϵ_o	permittivity in free space
H	solar to electric power conversion efficiency
η_{abs}	light absorption efficiency
n_c	conduction band electrons
N_c	conduction band states
η_{coll}	charge collection efficiency
η_{inj}	charge injection efficiency
K	Scherrer constant
λ	Wavelength
λ_{max}	maximum density per wavelength
ν	frequency of light
π	pi=3.14 radians
π^*	transition state for ligand
Φ_{sc}	semiconductor band bending
V	voltage
I	current
V_T	thermal voltage
E	Electron
\hbar	Plank's constant divided by h

LIST OF ABBREVIATIONS

ACN	Acetonitrile
AFM	Atomic Force Microscopy
AM	Air mass
AM0	Air mass zero
AM1.5	Air mass 1.5
BE	Binding energy
Btu	British thermal unit
CB	Conduction band
CCD	Charged couple device
CDCA	Chenodeoxycholic
CE	Common electrode
CV	Cyclic voltammetry
DSSC	Dye sensitized solar cell
DTA	Differential thermal analysis
EE	Electrolyte electrode illumination mode
E_g	Energy band gap
<i>EIS</i>	Electrochemical impedance spectroscopy
<i>eV</i>	Electron volt
<i>FF</i>	Fill factor
FWHM	Full width at half maximum
HOMO	Highest occupied molecular orbital
I/O	Input/output
IPCC	International panel for climate change
<i>IPCE</i>	Incident photon-to-current conversion efficiency
IR	Infrared
ITO	Indium tin oxide

<i>I-V</i>	Current-voltage
LED	Light emitting diode
LHE	Light harvest efficiency
LUMO	Lowest unoccupied molecular orbital
M	Molarity
MLCT	Metal-to-ligand charge transfer
N3	Commercial name for RuI ₃ (NCS) ₂ dye complex
N719	Commercial name for RuI ₂ (NCS) ₂ complex
N749	Commercial name for RuL'(NCS) ₂ :3TBA
NHE	Normal hydrogen electrode
NREL	National Renewable Energy Laboratory
Oc	Open circuit
OPV	Optoelectronic photovoltaic
PDF	Powder diffraction file
PV	Photovoltaic
RE	Reference electrode
Red	Reduced species
SEI	Semiconductor-Electrolyte Interface
SEM	Scanning Electron Microscopy
TCO	Transparent conducting oxide
TW	Terawatt
UV	Ultraviolet
Vis	Visible
WE	Working Electrode
XRD	X-Ray Diffraction

LIST OF CHEMICAL FORMULAE

Al	Aluminum
Cds	Cadmium sulphide
CdTe	Cadmium telluride
CO ₂	Carbon dioxide
COOH	Carboxylic groups
F:SnO ₂	Fluorine-doped tin oxide
GaAs	Gallium arsenide
InO ₃	Indium oxide
K	Potassium
Nb ₂ O ₂	Niobium dioxide
OH	Hydroxyl radicals
Pt	Platinum
SnO ₃	Tin trioxide
TiO ₂	Titanium dioxide
Y ₂ O ₃	Yttrium trioxide
ZnO	Zinc oxide

CHAPTER ONE

INTRODUCTION

1.1 Background of study

In the twenty first century, the worldwide energy concern is caused by the increasing need to content the energy demand of developed nations and the obligation to produce energy through techniques that have low negative environmental impact. Probably the biggest challenge that faces the global society today is the means of devising a replacement for the gradually but unavoidably depleting fossil fuel with renewable and sustainable energy sources and, at the same time, circumvent harmful consequences due to existing energy processes on environment and health (Grätzel, 2009). As a result of global technological and economic advancement, the consumption of energy has increased to sustain the development therefore the demand for energy has grown in recent years. It has been reported that the increase in world primary energy consumption is 1.4% annually and from estimations, it is expected to hit 815 quadrillion BTUs by the year 2040 (U.S Energy Information Administration, 2016). Presently, the energy economy remains vastly reliant on coal, natural gas and oil (which accounts for over 85% of the total energy production). However, it is estimated that global demand for fossil fuels will soon exceed yearly production and scarcities of the same may result to worldwide economic and political crises and conflicts. It is a scientific fact that burning of fossil fuels discharge harmful emissions to the environment and the combustion products have not only local but also global effects. According to the International Energy Outlook of 2016, the world energy related CO₂ emissions will reach 43.2 billion metric tons in 2040 (EIA, 2016). The consumption processes of fossil energy is a major cause of the so-called greenhouse effect. The rise in the quantity of CO₂ from fossil based energy combustion and then released in air, in addition to other greenhouse gasses, result to a reduction of the airflow with the resultant isolation of the warm air within the atmosphere, hence generating an overall rise in the temperature on the Earth.

There is a prediction that in the next one hundred years, average global temperature will rise to about 4.0 °C, subject to model parameters which include world population growth, primary energy source, and economic growth (Intergovernmental Panel on Climate

Change, 2014). On this note, the Paris climate change conference 2015, COP 21 agreed as follows: “Holding on holding the increase in the global average temperature to well below 2°C above pre-industrial levels and pursuing efforts to limit the temperature increase to 1.5°C above pre-industrial levels, recognizing that this would significantly reduce the risks and impacts of climate change”. The global energy demand in 2011 and the prediction for 2040 is reported in figure 1.1 below.

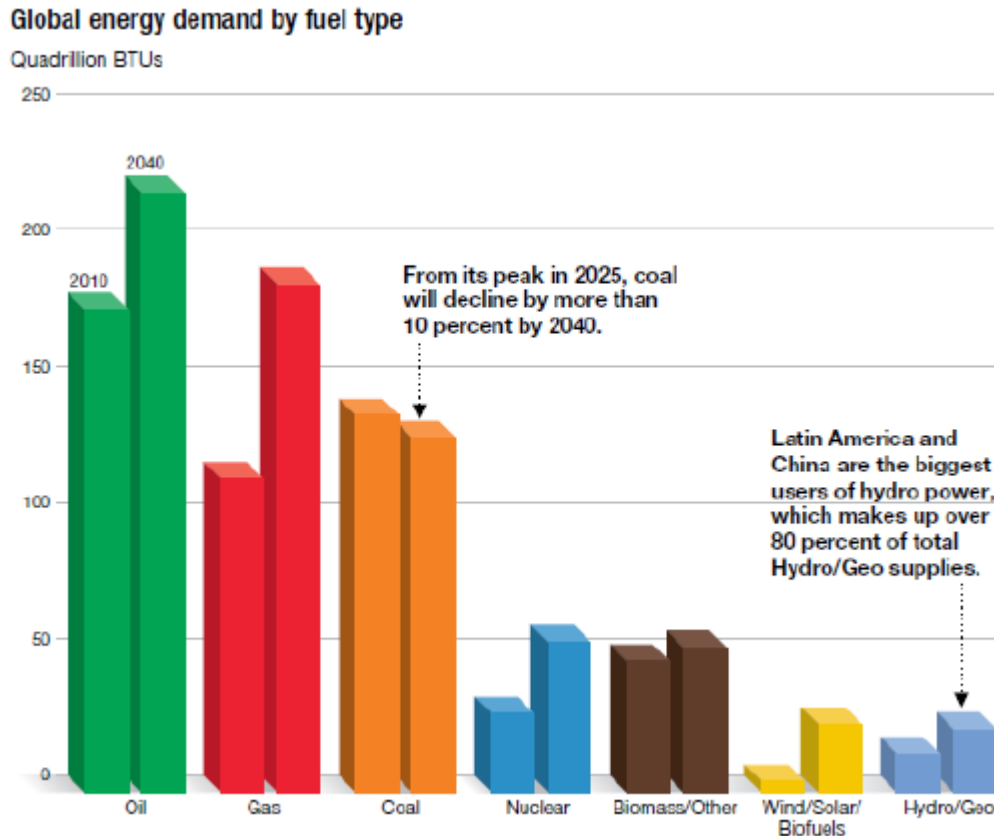


Figure 1.1: Global energy demand by fuel type (ExxonMobil Energy outlook, 2012).

The interpretation is that there is a very high possibility of stored energies’ continuous domination of the market though coal is predicted to diminish a bit, renewable energy will tremendously escalate.

The concept “renewable energy” connotes energy derived from a wide spectrum of sources that are based on self-renewing and sustaining domain that include sunlight, wind, water fall, geothermal, biomass such as energy crops and industrial, agricultural and municipal

wastes. All these can be used to generate electricity for all sectors of our economy, fuels for transportation, and heat for buildings and industries.

For a self-reliant and competitive economy, alternative energy sources must be efficient and sustainable, low cost and environmentally friendly. For instance energy source such as nuclear power is not environmentally friendly because nuclear plants have waste disposal and public safety related issues due to the use of radioactive nuclei and production of radioactive wastes.

Among all the available technologies for producing renewable energy, photovoltaics (PV) remain the most promising. This is because the annual solar radiation reaching the earth is 3×10^{24} J implying it can meet our current global energy demand by covering just 0.13% of the Earth's surface with PV cells that are 10% efficient (Grätzel, 2001). Apart from the advantage that solar energy is potentially abundant, photovoltaic cells require little care, off-grid operation and no noise, which are best for application in rural areas or portable applications.

1.2 Photovoltaics (PV)

1.2.1 The photovoltaics market

The development of semiconductor electronics based on silicon paved way for a major breakthrough in photovoltaic devices. This was via the fabrication of a p-n junction boron doped silicon wafers which yielded a conversion efficiency of about 6% in the mid-20th century (Chapin, *et. al.*, 1954). The solar cells based on the silicon technology were classified as the first generation of solar cells.

Since the pioneering silicon technology in early fifties, photovoltaic devices had been employed principally in space applications till second half of the last decade that grid connected photovoltaic systems began to have a substantial impact on the terrestrial market. The most important benefit of PV is clean source of energy, which allows for the mitigation of atmospheric pollution.

PV technology has over the last decade demonstrated its promising ability to become a major source of energy generation for the world with drastic growth even in the face of global economic crisis. That promising growth is expected to last in the years to come as global awareness of the benefits of PV intensifies. The world's PV aggregate installed capacity was reaching 138 GW at the end of 2013. In 2014, it was already 177 GW and up to 50 GW were added in 2015 bringing a total Global capacity to 227 GW. This could produce 280 TWh of electricity per year as seen in figure 1.2 (Wetstone *et. al.*, 2016) which is enough to power over 65 million households.

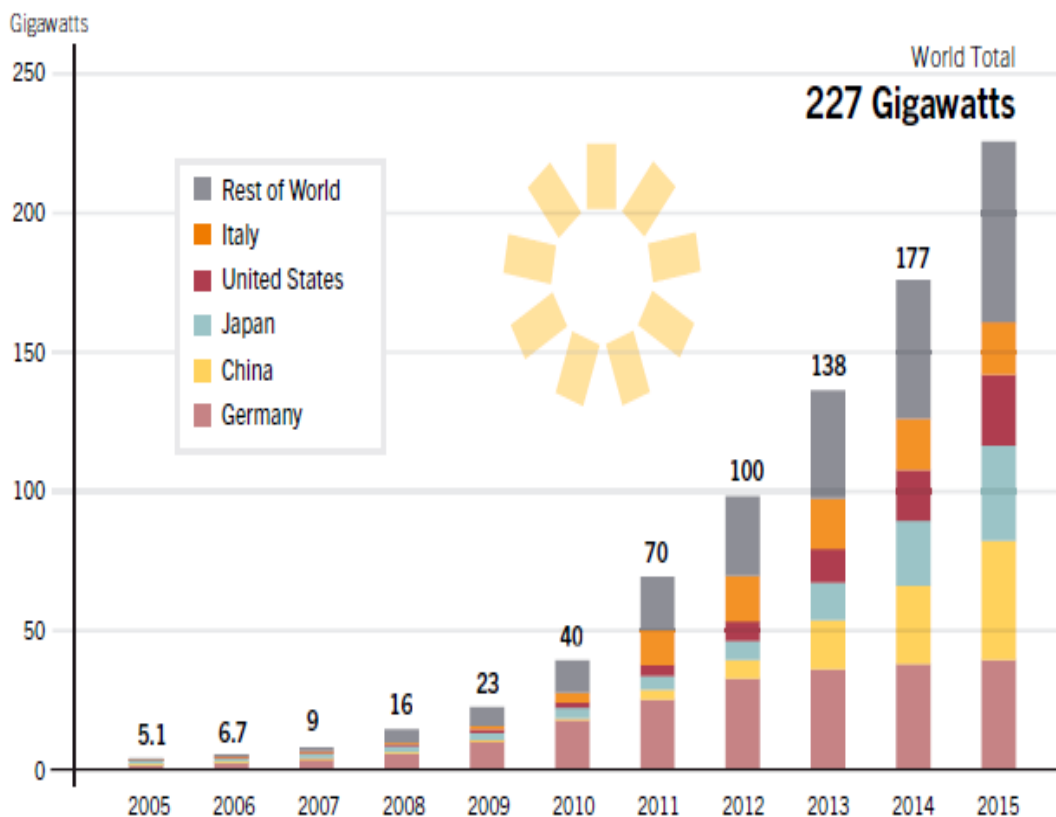


Figure 1.2: Photovoltaic Global capacity, by country 2005-2015 (Wetstone *et. al.*, 2016)

As observed from figure 1.2, the annual market was nearly 10 times the aggregate Global capacity just a decade earlier. In most parts of the world, market growth is a result of the rising effectiveness of solar PV, new government policies and programmes, growing demand for power and increasing consciousness of solar photovoltaic prospects as countries pursue mitigation of pollution and emission of CO₂. After hydro and wind power,

photovoltaic is ranked the third most vital renewable energy source considering worldwide installed capacity.

1.2.2 Solar cell technologies

Photovoltaic cell technologies are classified into first, second and third generations according to their theoretical maximum conversion efficiency and nature of the materials. The first generation comprises cells that are made of materials with high purity and structural defects in low concentrations. They are still at the moment the cells with the highest overall conversion efficiency. In this group we have crystalline silicon, single-junction GaAs and multijunction solar cells, with reported highest laboratory efficiencies of 25%, 29% and 46%, respectively (Green *et. al.*, 2016).

Mono and poly-crystalline bulk silicon presently control the photovoltaic market for terrestrial applications because of their finest concession between costs and performances. Silicon cell technique is *p-n* junction fabrication based where various parts of the semiconductor are doped with different impurities to produce the junction. Hence in between p-type and n-type materials, an interface is created which generates a built-in electric field due to various chemical potentials that electrons and holes possess across the interface. When a photon of energy larger than the band gap produces an electron-hole pair near the interface, the intrinsic electric field facilitates charge separation in the so-called depletion layer. Shockley and Queisser (1961) established a theoretical maximum conversion efficiency of 33.7% for a *p-n* junction (Hagfelt *et. al.*, 2010).

Though silicon is the most widely employed and researched material, it is not the perfect semiconductor for PV applications. It is an indirect semiconductor which has a low optical absorption efficiency therefore, Si wafers should be as thick as over hundred microns to absorb adequately the utmost incident light. This in addition to high cost of refinement and crystallization processes of silicon, renders production of silicon cells highly expensive. In view of this, Si-based first generation photovoltaic being a strong and established photovoltaic technology, its cost effective possibility still remains constrained. Moreover, efficiencies of silicon solar cells are not yet near the Shockley-Queisser theoretical limit

for a single-junction cell (Avrutin *et. al.*, 2011) even if there is a possibility of improvement.

To confront the challenges related to first generation PV, different approaches have been considered: (a) reduce the production cost and (b) improve the energy conversion efficiency beyond the Shockley-Queisser limit of 33.7% (Shockley and Queiser, 1961). The first approach resulted to the development of thin film solar cells called “second generation” photovoltaics. In another perspective, methods attentive to devices that could surpass the Shockley-Queisser limit have led to the origin of “third generation” photovoltaic technologies.

Second generation PV are called thin film solar cells, because the thickness of their constituent material is less than one micron which is 100-1000 times thinner compared to the first generation devices. The development of thin film solar cells is a motivation from their prospects for cost effectiveness. Whereas silicon solar panels are fabricated by the assemblage of single cells about one hundred square centimeter silicon wafers, thin film semiconductor materials are deposited on large planes, making them cost effective in terms of large scale assembly. Examples of thin film solar cells include Amorphous silicon (a-Si) and Copper indium gallium (di) selenide. Amorphous silicon (a-Si) is regularly employed in the double-junction or triple-junction devices which are produced overlaying different cells based on materials having varying band gaps, which absorb at different wavelength regions and CIGS has the highest efficiency among the thin film solar cells (Nazeeruddin *et. al.*, 2001).

Contrary to silicon wafers based photovoltaic devices (first generation), which are already near the theoretical conversion efficiency limit, thin film solar cells (second generation) are still far below their potential. Thin film technologies are in the initial production phase, and efficiencies of small area laboratory devices do not simply transform to efficiencies of large modules. The major challenges related to this technology are the use of harmful materials like cadmium and scarce elements such as telluride (Te) and indium (In). It is

somewhat controversial to use toxic materials to build a technique that is being promoted as environmental friendly.

Over two decades ago, a third generation of solar cells evolved. These devices, instead of a p-n junction as in the preceding generations was based on a multilayer structure in which charge carriers exchanged. The concept third generation refers to PV systems which either do not fall into the previous generations or try to exceed the Shockley-Queisser limit. Exploration on various methods to achieve conversion efficiency beyond 30% have been carried out. So far, tandems of cells deliver the greatest recognized illustration of how such high efficiency is likely reached. For instance, conversion efficiency is improved by stacking cells of varying band gaps to boost the spectral sensitivity (Green, 2006). On the whole, by assembling a sizable number of appropriately tailored and designed cells, efficiencies of concentrated and not concentrated solar illumination as high as 86% and 67% respectively are theoretically achievable (Avrutin *et. al.*, 2011).

In the 1990s, another concept of solar cells made from nanostructured and organic materials was conceived as a novel technique to fabricate cost effective PVs. The newly discovered organic and polymeric conjugated semiconducting materials seems very much promising for photovoltaics due to a number of reasons, namely: lightweightness, low consumption of materials, flexibility, low cost for large scale production. This type of solar cells show a promising prospect for progress since molecular and nanostructural engineering techniques can be exploited for further advancement. The most active research fields consist of organic heterojunctions (Benanti & Venkataraman, 2006), extremely thin absorber (ETA) cells (Belaidi *et. al.*, 2008), hybrid solar cells (Greene *et. al.*, 2007). In organic heterojunction the active layer comprises a heterogeneous mixture (*polymerblend*) of two immiscible polymers: a donor (n-type) and an acceptor (p-type). Polyphenylene vinylene derivatives and poly-alkylthiophenes are common donors; fullerene and its derivatives are common acceptors.

One of the solar cells made from nanostructured materials is a novel PV cell based on the principle of plant photosynthesis called dye sensitized solar cell was developed by

Grätzel's group (O'Regan and Grätzel, 1991). The device reported had sensitized nanoporous TiO₂ particles with a conversion efficiency of 7.1% (O'Regan and Grätzel, 1991). A typical dye-sensitized solar cell comprises a wide band gap semiconductor having a surface adsorbed dye sensitizer coated onto a transparent conducting oxide (TCO) coated on glass substrate. This forms an interface with a redox-coupled electrolyte that helps in ion diffusion and dye regeneration. Their finding opened a fresh area of scientific study and since then many researchers have been working on the enhancement of the efficiency and the stability of this type of solar cells. This area of research has attracted the attention of scientists from the start of the 21st century, publishing 2 or 3 research articles every day (Hagfeldt *et. al.*, 2010). This device has quite a lot of advantages over the previous generations technologies, one of which is, its performance is indifferent to temperature change; therefore the rise in operating temperature to 60 °C (the temperature attained at full one sun illumination) has no consequence on the conversion efficiency (Grätzel, 2000). It has also been reported elsewhere that DSSC's external quantum yield of photocurrent generation is close to unity if optical losses in the conducting substrate are accounted for (Grätzel, 2005).

The device's performance also imitates photosynthesis which is a process known to be highly efficient. Considering these qualities, DSSCs have the possibility to attain high efficiencies at a lower cost compared to the first and second generation technologies (Grätzel, 2003). Though DSSCs have shown very promising potentials, they are being faced by some challenges, key among them being the low overall conversion efficiencies. The current record efficiency reported for a dye sensitized solar cell is 13% (Mathew *et. al.*, 2014). However compared to the other technologies, the coming of DSSC (shown in figure 1.3), is relatively recent but the efficiencies are already near that of amorphous silicon.

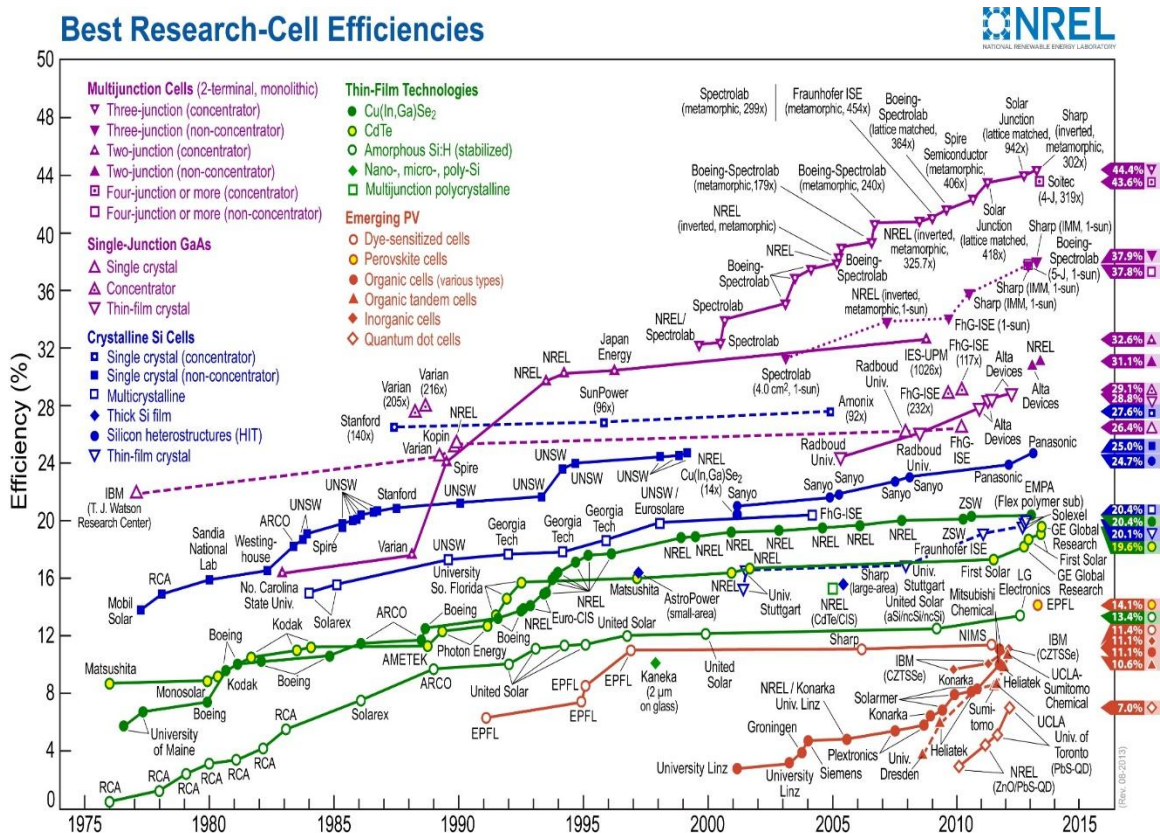


Figure 1.3: Solar cell efficiency timeline from 1975 to 2015 (National Renewable Energy Laboratory, 2014).

In summary, though dye sensitized solar cells have very promising potential for a cheap source of electrical power vis-à-vis silicon based solar cells, they still have low conversion efficiencies. One very critical part contributing to this low efficiency is the light harvesting ability of the dye semiconductor interface which is not yet fully explored, besides the need to develop cheap but stable sensitization. Previously, progresses were made in light harvesting efficiency of a dye-adsorbed TiO₂ electrode by way of light scattering (Hore *et al.*, 2006; Nelson and Deng, 2008; Yang *et al.*, 2008; Zhao *et al.*, 2011). The light-scattering consequence was attained by adding TiO₂ layers. Interestingly, adding scattering layers by means of the TiO₂ large particles warrants sufficient light trapping in the device (Chuangchote *et al.*, 2013; Hyung *et al.*, 2008), due to a rise in the absorption path length of photons and optical confinement. (Ferber and Luther, 1998) and (Rothenberger *et al.*, 1999) established the light-scattering effect via the transport theory and a many-flux model, respectively. Having known the scattering capacities of TiO₂ films, it is essential

that the TiO₂ electrode possesses a high surface area, which is accountable for optimal dye loading and effective photocurrent generation. In view of this, artificial pores were created in TiO₂ films by the use of acetylene black (Cho *et. al.*, 2013) and polystyrenes spheres (Pham *et. al.*, 2012) to enhance light harvest efficiency (LHE). However, in their studies, a number of important properties of the films were no characterized. In this study, film thickness and electrolyte concentration will be studied.

It is in this regard that this work sort to create artificial pores in TiO₂ thin films using carbon black so as to enhance light harvest efficiency, and in addition optimize film thickness of porous TiO₂ films and also find an optimum electrolyte concentration for a TiO₂ based dye sensitized solar cell.

1.3 Problem statement

Light harvesting efficiency has been enhanced by the employment of an additional layer of a semiconductor material which increases light scattering and trapping. For instance, light scattering in the mesoporous TiO₂ particles is currently enhanced by employing a separate TiO₂ scattering layer. The increased film thickness has limitations on effective charge transport especially in dense electrolyte media such as Cobalt (II/III) complex. These thicker films also reduce light intensity on some parts of adsorbed dye hence decreases photocurrent generation. In view of the above, there is still the challenge of optimization of light scattering versus charge transport and photocurrent generation which still limits the overall light harvesting efficiency. An optimum electrolyte concentration in DSSC of porous TiO₂ thin film has not been determined therefore compromising effective ion mobility. This work sought to fabricate and characterize dye sensitized solar cells based on highly porous TiO₂ thin films.

1.4 Objective of study

The aim of this study was to fabricate and characterize dye sensitized solar cells based on highly porous TiO₂ films. The specific objectives were:

- i. Study the effect of porosity and thickness on the optical properties of TiO₂ thin films

- ii. Examine the influence of porosity and thickness on electrical properties of TiO₂ thin films.
- iii. Analyze the TiO₂ microstructure employing X-Ray Diffraction (XRD), Scanning Electron Microscopy (SEM) and Atomic Force Microscopy (AFM) techniques
- iv. Fabricate and study the *I-V* characteristics of complete dye sensitized solar cells at varying porosity, film thickness and electrolyte concentrations.
- v. Determine the electrochemical impedance spectroscopy (*EIS*) of dye sensitized solar cell.

1.5 Justification and significance of the study

The study of the enhanced porosity in the working electrode of dye sensitized solar cell is expected to greatly contribute to the search for optimizing the important parameters for higher efficiency and low cost. In addition, the optimizations of film thickness and electrolyte concentration are also a necessary ingredient for improved efficiency of dye sensitized solar cell.

In this study, carbon black nanoparticles are employed to create pores in TiO₂ thin films that will serve the role of a light scattering layer hence increasing the light harvesting efficiency of dye sensitized solar cell without any negative effect on the charge transport as for the case of multiple layers. It also maintains the purity of TiO₂ since the pores are created by thermal decomposition of carbon black. Moreover, anatase nanocrystalline TiO₂ provides the maximum efficiency with optimization of surface area, porosity, pore diameter, transparency and film thickness. Though TiO₂ is available in abundance and relatively cheap, the creation of artificial pores is cheaper than employing an additional TiO₂ layer for light scattering. In addition, pore enhancement will allow for an optimal film thickness which maintains high light intensity on the dye adsorbed semiconductor hence generating high photocurrent.

Apart from the fact that screen printing is the best method for large scale production, it is a simple, easily reproducible and non-complicated method of thin film coating. The use of this method allows for the easy incorporation of carbon black into TiO₂ nanoparticles at various film thicknesses.

Conclusively, porosity enhancement, film thickness and electrolyte concentration optimizations will provide important information towards the improvement in the overall performance and low cost production of dye sensitized solar cells.

CHAPTER TWO

LITERATURE REVIEW

2.1 Introduction

In this chapter, the historical development of dye sensitized solar cells is discussed in details. All components of DSSC are also discussed briefly with the porosity of semiconductor being the main focus of this work reviewed extensively.

2.2 Historical development of dye-sensitized solar technology

The ongoing work on dye sensitized solar cells originated from photography about the time photovoltaic effect was discovered. Louis Daguerre developed the first photographic image onto a mirror-polished surface of silver bearing a coating of silver halide particles (Daguerre, 1839; Bird, 1839) about the same time which Edmond Becquerel discovered photovoltaic effect (ExxonMobil Energy outlook, 2012). The halides applied in this photography had the band gap ranging between 2.7 eV and 3.2 eV thereby making them not photoactive to light of energy less than 2.7 eV (corresponding wavelength > 450 nm). A German photochemist, Vogel made an improvement in three decades later through dye sensitization of silver halide emulsions. This led to photo response extending into the red and infra-red (Sandler, 2002). However, the operating mechanisms of electron injection from excited state of the dye molecules into the conduction band of n-type semiconductor substrates remained unclear to scientists until almost a century later (Williams, 1960; Bourdon, 1965; Nelson, 1965). These early photography devices were characterized by poor dye adsorption on the semiconductor surface and low conversion efficiencies restrained by the limited, weak light absorption of the dye monolayer on the surface.

On the other hand, thicker dye layers raised the electrical resistance of the system without improving current generation (Bourdon, 1965). Years later an improvement was achieved in chemisorption of sensitizers, electrochemistry and the choice of photoanode materials as a result of the investigation reported (Grätzel, 2000) on zinc oxide. However, at that time a large number of the semiconductors that were used had the challenge of corrosion. In that regard, TiO₂ was found to be a material of choice sequel to Fujishima and Honda's demonstration of direct photolysis of water with TiO₂ (Fujishima and Honda, 1971).

TiO₂ electrode was found not to decompose after irradiation, that is, neither were titanium ions found in the electrolyte solution nor the electrode surface was changed. Tributsch investigated further on this by demonstrating the reaction of excited chlorophyll molecules at electrodes and made a comparison with photosynthesis (Tributsch, 1971). The effort to find a solution to the challenge of dye-adsorption was first approached through the idea of discrete particles to make a sufficient interface (Duonghond *et. al.*, 1984), after which it was followed by the employment of photoelectrodes with high surface roughness. This was to enhance multiple light reflections at a rough surface, hence trapping most photons with a dye monolayer having a high molecular extinction.

Following all these researches in about one and half centuries, a major breakthrough was achieved with a nanocrystalline photovoltaic device that had a conversion efficiency of 7.1-7.9% under AM 1.5 solar illumination (O'Regan and Grätzel, 1991). The efficiency of this cell has greatly improved since its discovery. Employing a molecularly engineered porphyrin dye, coded SM315 with cobalt(II/III) redox shuttle, a current record efficiency of 13% has been achieved (Mathew *et. al.*, 2014). Recent achievements on long term stability with non-volatile electrolytes has increased the prospects of practical applications and put the dye sensitized solar cell on the right path for commercialization.

2.3 Components of dye sensitized solar cell

The sensitizers used in DSSC can be classified into two major groups namely; metalorganic and organic dyes. Metal-based sensitizers have costly synthesis process, comparatively low molar extinction coefficient in the visible region, inadequate accessibility of precursors and waste disposal issues. For these reasons, metal-free organic dyes could offer several advantages, being processed with simple, fast and cost effective synthesis approach and possess high molar extinction coefficients (Park *et. al.*, 2012; Park *et. al.*, 2013). Comparing with the Ruthenium based sensitizers, however, organic dyes exhibit lower conversion efficiencies, because of the deposition of dye particles on the semiconductor surface and narrow light absorption bands in the visible region.

The most commonly used of all metal and organic dyes, are ruthenium or osmium derivatives, which are known for lasting stability. Precisely, the polypyridyl ruthenium sensitizer family produces DSSCs with higher conversion efficiencies. The molecular structures of the commonly used ruthenium-based sensitizers are as displayed in figure 2.1.

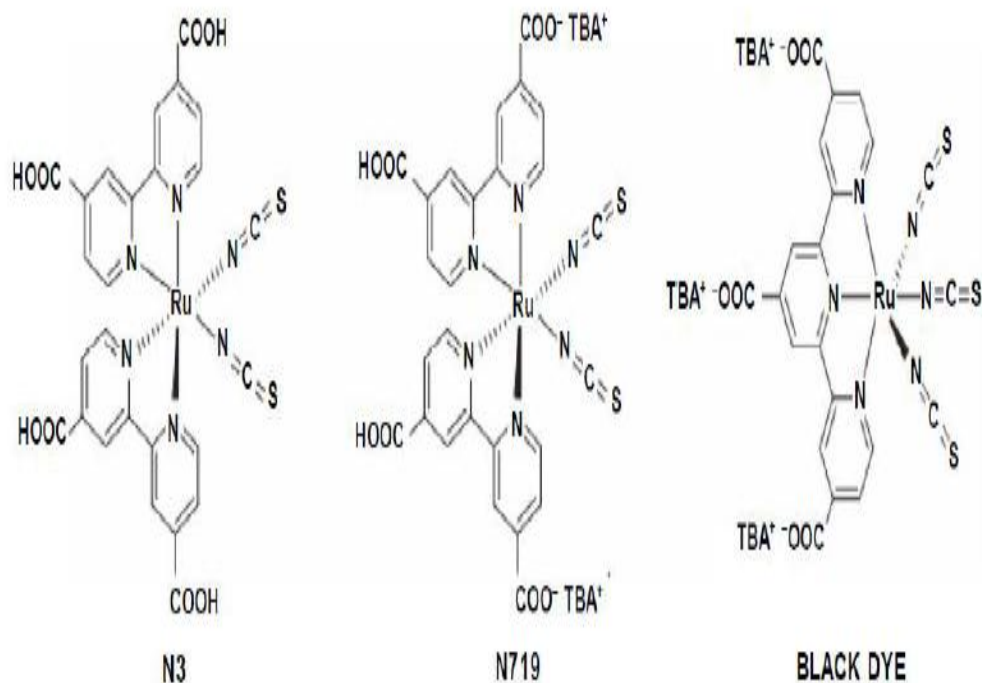


Figure. 2.1: Molecular structure of N3, N719 and N749 (“black dye”) sensitizers (Jena *et. al.*, 2012).

The first sensitizer to be developed in this group was the $RuL_2(NCS)_2$ ($L = 2,2'$ -bipyridyl-4,4'-dicarboxylic acid), N3 dye, which achieves a photoconversion efficiency as high as 10% (Nazeeruddin *et. al.*, 1993). Using this dye as control and replacing two protons with a tetra-*n*-butylammonium (TBA) cation group, the so-called N719 dye, $[RuL_2(NCS)_2] \cdot 2 TBA$ was produced. Introducing deprotonation alters the polarity at the boundary, thus shifting the semiconductor conduction band and increasing the V_{oc} of the cell. The Ru complexes are anchored to the TiO_2 surface by means of carboxylic groups. Anchoring ensures huge electronic interaction between the ligand and the conduction band of the semiconductor, thereby enhancing electron injection from the Ru complex into the oxide material.

The major limitation of these dyes is their reduced capacity to absorb light with wavelengths above 600 nm. N3 and N719 display a spectral absorption within the visible region, beginning from 400 nm. It is in this regard that several other dyes have been proposed. Investigations have revealed that when some molecules of the dye are substituted, the LUMO level of the sensitizer goes up and the HOMO level goes down, resulting to the absorption of higher wavelength of light. For instance, replacing a terpyridine group and a cyanide group with two bipyridine groups in the $[\text{RuL}'(\text{NCS})_3]: 3$ TBA ($\text{L}' = 2,2':6',2''$ -terpyridyl-4,4',4''-tricarboxylic acid) sensitizer (known as N749 or “black dye”), the absorption edge of the dye is moved by approximately 100 nm towards IR region. This is illustrated in Figure 2.2, where the Incident Photon-to-electron Conversion Efficiency (IPCE) spectrum of a DSSC made of a black dye is compared to an N3-based DSSC. The figure shows the absorption edge of the black dye goes to a maximum 900 nm, thus generating an overall photocurrent of up to 20.5 mA/cm^2 (Nazeeruddin *et. al.*, 1997).

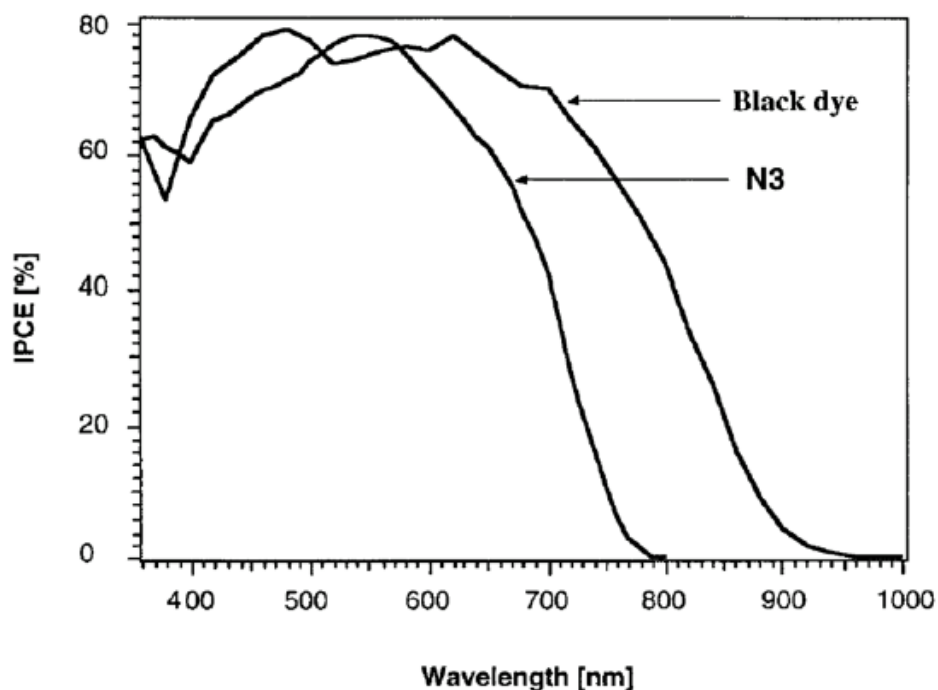


Figure 2.2: Incident Photon-to-electron Conversion Efficiency of DSSCs sensitized by N3 and N749 (“black dye”) dyes (Grätzel, 2000).

Several groups of organic sensitizers were projected in the past decade. The development of organic dyes based DSSCs has been very fast in recent years and the conversion efficiencies of these cells have been comparable to those based on polypyridyl ruthenium dyes. Some of the frequently employed organic dyes such as coumarin, indoline, cyanine and squaraine dyes are shown in figure 2.3. Hara *et al.*, (2001) proposed a sequence of coumarin derivatives with which an efficiency of 7.7% equivalent to N719 was obtained. Indoline dyes characterized by their reduced photodegradation that allows for a high long-term stability of the cell were synthesized for the first time and a 9.5% photoconversion efficiency was achieved with the so-called D205 dye (Horiuchi *et al.*, 2003). High molar extinction coefficient values and the absorption capacity of near-IR radiation have been reported to be typical features of Cyanine dyes (Ma *et al.*, 2008). However the photovoltaic properties of DSSCs depending on these dyes are relatively low. For instance, the use of Cy3 dye yields an efficiency of 4.8% at 75 mW/cm² illumination (Wu *et al.*, 2008). SQ1 and SQ2 dyes which belong to the Squaraine family, proposed by Grätzel and his colleagues (Yum *et al.*, 2007; Geiger *et al.*, 2009) have been reported to have efficiencies of 4.5% and 5.4% respectively. These dyes too exhibit high molar extinction coefficient values and strong electronic coupling with the TiO₂ surface.

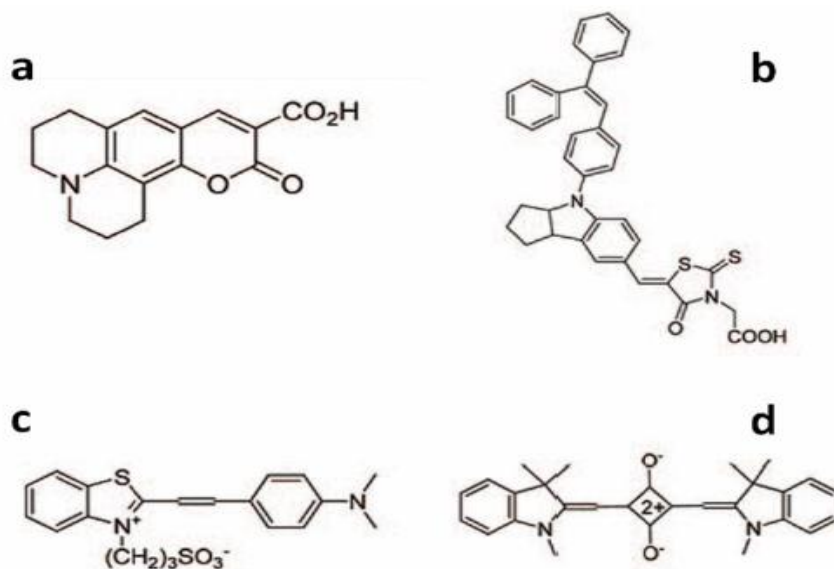


Figure 2.3: Molecular structures of dyes of varying species of organic sensitizers: a) coumarin, b) indoline, c) cyanine and d) squaraine (Hagfelt *et al.*, 2010).

The use of a single dye for sensitization is often poorly performing. This is so because absorption spectrum is not easily harmonized with the solar emission spectrum. To overcome this limitation, co-sensitization with many dyes which have varying spectral responses is employed to increase the DSSC photovoltaic performance. Zhao *et. al.*, (1999) combined a sequence of squaraine dyes as co-sensitizer of ruthenium polypyridyl complexes which produced better performed Dye-sensitized solar cells in comparison to those sensitized with normal ruthenium polypyridyl complexes.

Semiconductor quantum dots have also been employed as alternative to the use of molecules chemisorbed on the surface of the oxide. These are particles made up of small number of atoms in groups II-VI or III-V with very small dimensions. Their absorption spectrum is very wide and it can be altered by the change of dimension of the particles. Easy corrosion when in contact with a liquid electrolyte is their major drawback.

Having discussed the sensitizer, there is the need to quickly look at the progress in electrolyte whose choice largely depends the sensitizer as discussed above. The electrolyte plays a very vital function in the process of light-to-electricity conversion, being an electron transfer mediator with the role of regenerating the dye sensitizer from its oxidized state. Electrolytes for DSSCs are grouped into liquid, quasi-solid, or solid, depending on the viscosity. The liquid organic solvent-based electrolyte is the commonly used electrolyte in DSSCs. It consists of a redox couple dissolved in a high dielectric constant organic solvent with some additives to boost the device performance (Hagfeldt *et. al.*, 2010).

Iodide/triiodide (I^-/I_3^-) redox couple is the most employed redox couple due to its sluggish recombination process. Electrolytes made from this couple are normally prepared by dissolving iodide salts and cations such as Li^+ , Na^+ and Mg^+ in a liquid solvent. The corrosive properties of iodine however led to the search for alternative redox couples such as Br^-/Br_3^- (Ferrere *et. al.*, 1997), $SCN^-/(SCN)_3^-$ (Oskam *et. al.*, 2001) and $SeCN^-/(SeCN)_3^-$ (Wang *et. al.*, 2004). Despite these redox couples having favorable electrochemical and non-corrosive properties, they still have poor chemical stability (Hagfeldt *et. al.*, 2010). In addition, some coordination compounds which include copper and cobalt complexes have

also been employed as redox mediators (Sapp *et. al.*, 2002; Hattori *et. al.*, 2005). Presently, Co complexes are the utmost promising redox couples. They are noncorrosive, nonvolatile, and comparatively transparent to the visible light. In addition, it was reported lately that Co(II/III)tris(bipyridyl)-based redox electrolyte can give a power efficiency of up to 13% (Mathew *et. al.*, 2014).

In the application of DSSC, some important properties of solvents are usually taken into consideration. The solvent should possess low volatility within the operating DSSC temperature range to permit a speedy flow of charges, and a high dielectric constant to allow for an easier redox couple dissolution (Hagfelt *et. al.*, 2010). Among all the solvents used in DSSC research field, acetonitrile (ACN) is the most performing, for the reason of its outstanding stability, low viscosity and capacity to dissolve a lot of salts and organic molecules. However, ACN boiling point is low (78 °C). Therefore, for long-term stability of the DSSCs, 3-methoxypropionitrile (MPN) is preferable because it is characterized by 164 °C boiling point and low toxicity. An efficiency of 7.6% at 1000 h of continuous irradiance was achieved with MPN as solvent (Andrade *et. al.*, 2009). It is view of the above that solvents such as, water, ethanol, ethylene carbonate and propylene carbonate are not usually employed (Yu *et. al.*, 2011).

In regard to the additives, so many cations and compounds have been employed in liquid electrolytes to improve the cell photovoltaic performance. 4-tert-butylpyridine (TBP) is one of the commonly used whose effect suppresses the dark current and increase Fill Factor and efficiency values through prompting the coordination between N atoms and Ti ions at the TiO₂ surface, thus restraining recombination (Hao *et. al.*, 2004). Addition of guanidinium thiocyanate (GuSCN) to liquid electrolyte raises both current and voltage due to positive shift of TiO₂ conduction band reduction of charge recombination (Zhang *et. al.*, 2009). So also, Li cations are commonly applied as additives. The cations are then adsorbed on the TiO₂ nanoparticles surface, which result to an important rise in photocurrent density values. The increase in photocurrent is because of the capability of Li ions to reduce the acceptor states of TiO₂, which changes the flat band on the photoanode surface and making the electron injection more energetically favorable (Kelly *et. al.*, 1999).

The major limitations in exploiting liquid solvent-based electrolytes include their stability, sealing and leakage, which affect the overall efficiency with time. In view of this, several proposals are being considered to provide solutions, amongst them are, solvent-free liquid electrolytes (quasi-solid and solid electrolytes). Quasi-solid are based on the so-called room temperature ionic liquids (RTIL) and they exhibit reduced volatility, good chemical and thermal stability and high ionic conductivity. Mostly employed RTILs for DSSCs include alkyl imidazolium, trialkyl methylsulfonium, and alkylpyridinium salts. The only limitation of RTILs is their high viscosity that brings about slow charge carriers diffusion (Santiago *et. al.*, 2007).

Quasi-solid electrolyte is usually developed from organic solvent or ionic liquid based electrolytes which are gelled, polymerized, dispersed in polymeric matrix, or in which nanoparticles are dispersed (Hagfelt *et. al.*, 2010). These electrolytes consist of conductive polymers, hole-conducting molecular solids or organic p-type conductors, such as polypyrrole (Murakoshi *et. al.*, 1997), poly(3,4-ethylenedioxythiophene) (PEDOT) (Saito *et. al.*, 2002), poly(3-hexylthiophene) (P3HT) (Ravirajan *et. al.*, 2006), polyaniline (PANI) (Somani & Radhakrishnan, 2003) and 2,2',7,7'-tetraakis-(N,N-di-p-methoxyphenyl-amine) 9,9-spirobifluorene (spiro-OMeTAD) (Cai *et. al.*, 2011). Up to this moment, the photovoltaic performance of DSSCs based on quasi-solid electrolytes are still low compared to liquid based electrolytes.

Just before the photoanode is discussed, there is the need to briefly look at the counter electrode without which the current generated cannot be collected. Similar to the photoanode, the counter electrode is fabricated using a glass substrate coated with a film of transparent conductive oxide (TCO). For the purpose of ensuring a sufficient and fast reduction reaction kinetics at the TCO-coated cathode, a catalyst coating is required (Hagfelt *et. al.*, 2010).

Platinum (Pt) and carbon-based materials are the commonly employed catalysts in DSSCs. The application of Pt yields high current and voltage, *IV* and also exhibits low counter electrode resistance (Hauch & Georg, 2001). Platinum catalyst coating is applied easily by

methods such as electrochemical (Hagfeldt & Grätzel, 1995; Smestad *et. al.*, 1994), sputtering (Nazeeruddin *et. al.*, 1993), pyrolytic or spin coating (Lee *et. al.*, 2001). However, Pt deposited by electrochemical and vapor methods has been found unstable in presence of the iodide-based electrolyte (Olsen *et. al.*, 2000). In view of the above, alternative Pt catalyst coating method known as "platinum thermal cluster catalyst" was developed. This catalyst gave a better kinetic performance compared to normal platinum coating methods, chemical and electrochemical stability in DSSCs and low platinum loading of 5-10 mg/cm², hence resulting in costs reduction, mechanical stability and optical transparency of the counter electrode.

Even though platinum shows outstanding catalytic accomplishment, it is very costly. In order to find a cost effective solution for counter electrode fabrication, graphite is employed (Kay & Grätzel, 1996; Acharya *et. al.*, 2010). Other carbon materials such as hard carbon spherule (HCS) have been explored as counter electrodes for dye-sensitized solar cells (Huang *et. al.*, 2007). Though investigation revealed that photovoltaic properties were powerfully influenced by the specific surface areas of the carbon materials, their conversion efficiencies were very much close to those of Pt. based DSSCs. The major challenges confronting this material are the low homogeneity and bond to the substrate which results to poor performance of the cells compared to the Pt-based cells. A very interesting alternative material in this regard is graphene, which in principle could both serve the role of a transparent conductive film and catalyst, hence reduces the cost of fabrication of the counter electrode (Wang & Hu, 2012). In addition, another promising project uses a porous carbon counter electrode as a catalyst layer. This carbon electrode comprises a mixture of carbon black, graphite powder and nanocrystalline TiO₂ particles. This combination results in high conductivity (sheet resistance of 5 Ω/sq for a 50 μm-thick layer) for the reason of carbon black particles joining individual graphite flakes, while the TiO₂ particles serve as binders to the entire structure.

Finally and most importantly, the photoanode which is the component of DSSC that on which this study is focused, is hereby discussed at length with emphasis on TiO₂ material.

Considering the several wide bandgap oxide semiconductors studied as prospective electron acceptors for DSSC, TiO₂ remains the most versatile. It provides the maximum efficiencies, is chemically stable, non-toxic, and accessible in huge magnitudes (Malliga *et. al.*, 2014). Its anatase nanocrystalline form offers the maximum efficiency with optimization of surface area, porosity, pore diameter, transparency and film thickness. TiO₂ is the best semiconductor for the reason its wide bandgap, nanoporous structure with large surface area and, suitable HOMO and LUMO alignment with the electrolyte and dye respectively. In the dark, this wide bandgap semiconductor oxide film is insulating. Due to the nanometer size of the particles (~20nm), a single electron injection produces an electron concentration of 10¹⁷cm⁻³ resulting in a conductance in the order of 10⁻⁴scm⁻¹ for the electron diffusion coefficient of 10⁻⁴cm²s⁻¹ (Grätzel, 2005). Other structures of TiO₂ such as organized mesoporous film (Zukalová *et. al.*, 2005) or TiO₂ nanotubes (Kang *et. al.*, 2009) have also produced comparable efficiency. Both ZnO nanoparticles (Rensmo *et. al.*, 1997) and nanotubes (Martinson *et. al.*, 2007) have been employed in DSSC. ZnO does not require high-temperature annealing process like TiO₂, which enables DSSC fabrication on flexible polymer substrates. Other, alternative wide-gap oxides such as Y₂O₃ (Kay and Grätzel, 2002), In₂O₃ (Sharma *et. al.*, 2009), SnO₃, (Snaith & Ducati, 2010) and Nb₂O₂ (Viet *et. al.*, 2010) have been under study, and have potential for DSSC applications. Although individually these semiconductors do not perform efficiently, the combination of same have demonstrated promising outcome.

The size, shape, and crystal structure of the TiO₂ nanoparticles depend on the method of preparation of the film (Wang, 2002). The porosity is also a function of the annealing temperature profile. The average porosity increases from 15nm to 20nm with an increasing temperature from 400°C. However, with annealing temperatures above 500°C this trend becomes stable with no change in the pore-size distribution (Barbe *et. al.*, 1997). An annealing temperature study from 150°C to 450°C shows an increasing J_{sc} for films annealed at higher temperature, due to higher porosity. This is attributed to the increase of diffusion coefficient and carrier lifetime with increasing temperature (Nakade *et. al.*, 2003).

Nanoparticle size is another key parameter for DSSC. With increasing particle size electron diffusion coefficient rises with decline in surface area and the structure of grain boundaries. On the other hand, electron recombination lifetime decreases with particle size increase. Thus, a small particle size would be favorable for DSSC applications. However, charge injection efficiency is lowered with the decrease of the particle size due to reduced diffusion length. Hence, an optimization in the particle size is the requirement (Nakade *et al.*, 2003). It is important to mention that though DSSCs have been fabricated with TiO₂ film thickness of 0.5-2.0 μm (Kao *et al.*, 2009), the typical film thickness for DSSC is 5–20 μm (Simiyu, 2010; Hamadani *et al.*, 2011; Escalante-Quijano *et al.*, 2013; Wu *et al.*, 2013; Zhang *et al.*, 2014; Sedghi and Miankushki, 2015; Kumari *et al.*, 2016) with the TiO₂ mass of about 1–4 mg/cm². An optimum surface area of the sintered TiO₂ colloid is 75 m²/g and a porosity of 50–65% (Nazeeruddin *et al.*, 2001). Considering a Titania film of thickness ranging from 10 to 15 μm, the effective surface area is increased over a thousand times, which is the beauty of the mesoscopic structure, allowing for a dense monolayer of adsorbed sensitizer.

In a DSSC, TiO₂ layers thickness influences the photon absorption in direct proportion. For single-layer electrodes (20 nm particles) a small but linear fall in the open-circuit voltage (V_{oc}) is detected with a rise thickness. However, thickness response of the short-circuit current density (J_{sc}) is reliant on the viscosity of the electrolyte. A low viscosity electrolyte can support higher photocurrent resulting from thick nanocrystalline-TiO₂ layer, therefore the current displays a linear increase. However, for high viscosity electrolyte a peak in the current is seen and falls afterwards (Hara *et al.*, 2001). The thickness of a film being coated also depends on particle size and surface structure. For example, optimal thickness for 20 nm particles is half of that obtained for the 42 nm particles (Ito *et al.*, 2009).

Light scattering technique was employed since two centuries in photography and was found to improve the light harvesting efficiency. Titanium dioxide nanoparticle photoanode received a major improvement by the incorporation of a scattering layer made of large titania particles to boost light harvesting (Bird, 1839). The light scattering and optical management effects play very crucial roles in the development of dye-sensitized

solar cell photoanodes and their overall photovoltaic performance (Usami, 1997; Rothenberger *et al.*, 1999). Large TiO₂ particles in the range of 100 and 400nm are generally applied as light scattering media, either embedded in a matrix of smaller nanoparticles or more often screen-printed on top of a transparent mesoporous film (Wang *et al.*, 2004; Arakawa *et al.*, 2006). The two layer structure has become commonly applicable in majority studies on dye-sensitized solar cells (Grätzel, 2009), including the best cell of that period recording 12.3% power conversion efficiency (Yella *et al.*, 2011). In addition to the two layer structure, multilayer structures of different particle sizes have also been studied (Wang *et al.*, 2004; Arakawa *et al.*, 2008). In the recent past, Chen's group (Chen *et al.*, 2009) successfully synthesized 500 nm titania beads with a mesoporous surface, not only light scattering was achieved but also a large surface area was provided as anchoring sites for dye molecules.

Some improvements have been recorded in light harvesting efficiency of a dye-adsorbed TiO₂ electrode via light scattering (Zhao *et al.*, 2011). Given the scattering abilities of TiO₂ films, it is also important that the TiO₂ electrode possess a high surface area, which is accountable for optimal dye loading and effective photocurrent generation. With all the aforementioned approaches, it has been found that scattered photons are contained within the film by multiple reflections and their optical path length has been increased significantly beyond the film thickness. In as much as the light scattering effect from large particles has been comprehensively studied and simulated, achieving similar results with enhanced pores has not been adequately explored (Hore *et al.*, 2005). The addition of another layer increases the overall film thickness which decreases the V_{oc} of the DSSC due to the long diffusion length the photoelectron to transport to the electrode hence improving the probability of recombination (Tsai *et al.*, 2013; Escalante-Quijano *et al.*, 2013). The further increase in photoanode thickness contributed by the additional layer also reduces the J_{sc} of DSSC due to decrease in transmittance with increase in film thickness (Kao *et al.*, 2009).

Though TiO_2 is relatively cheap and readily available, the addition of TiO_2 layers may result to increase in the overall cost of DSSC and compromise the lightweight advantage of the device. In view of the discussed challenges facing the use of additional TiO_2 layers for light scattering, Trang-Pham *et. al.*, (2012) presented a simple design that realizes improved light harvesting with a reduced amount of dye quantity while concurrently enhancing the power conversion efficiency of (PCE) of dye-sensitized solar cells. Polystyrene (PS) spheres of sub-micrometer size were integrated with TiO_2 paste resulting in photo-anode with bimodal pore size distribution. The conversion efficiency of the cell rose from 6.3% to 6.9% for the reason of the artificial pores created without any additional TiO_2 layers. However, the polystyrene spheres are extremely expensive which could still result to high cost of device production. There is yet the need to create these pore without incurring too much expenses.

Another attempt was made to create artificial pores by the incorporation of acetylene black in TiO_2 thin films (Cho *et. al.*, 2013). In their work, DSSCs based on porous TiO_2 photo-electrode without a light scattering layer to improve the light harvesting efficiency were fabricated and studied. The structural and the photovoltaic performance of the DSSCs were compared with TiO_2 photo-electrode films with and without artificial pores. The conversion efficiency improved compared to cell made from bare TiO_2 films. The acetylene-black was incorporated for light-scattering and morphology change of the electrode and for a reduction of residual carbons in the TiO_2 photo-electrode films. This approach is no doubt very favorable for use in dye sensitized solar cells. However, the electrical properties of the photoelectrode films were not studied which may compromise the electrical conductivity of the films as pore sizes are being enlarged. Optical properties were not also explored even though their effect on the overall photovoltaic performance of DSSC is very crucial. Film thickness also needs to be varied as it is logical that its variation could affect porosity in terms of depth. As such, porosity of photoelectrode could have an effect on electrolyte concentration hence the need to study. It is in this regard that this research took a comprehensive study on pore enhanced TiO_2 films for applications in dye-sensitized solar cells.

CHAPTER THREE

THEORETICAL BACKGROUND

3.1 Introduction

This chapter deals with the fundamental theory of the working and characterization of dye-sensitized solar cell. Firstly, a complete DSSC is presented and its working principle is discussed. Subsequently, the semiconductor and electrolyte interface is discussed, explaining the way the structure of the interface influences the correlation between charge and potential. The procedure of charge transfer at the interface is also described. The second part of the theory describes the different characterization techniques namely; optical characterization, scanning electron microscopy, X-Ray Diffraction (XRD), *I-V* characterization, photocurrent and photovoltage spectroscopy is also presented.

3.2 Structure and basic components of a dye sensitized solar cell

A dye sensitized solar cell is the only solar cell device that separates the roles of light harvesting and charge transport in the process of photocurrent generation. The conventional p-n junction based process usually combines the two functions simultaneously. Splitting the functions offers huge possibilities for enhancing the individual components and roles of the cell. Since O'Regan and Grätzel (1991) developed the first dye sensitized solar in a span of over twenty five years today, there has been an exponential rising interest in this kind of technology.

The standard structure of a DSSC, which comprises a semiconductor photoanode, a counter electrode, a dye sensitizer and a redox coupled electrolyte (Weerasinghe *et. al.*, 2013), is shown in Figure 3.1. The photoanode is made up of a porous TiO₂ semiconductor coated on a conducting substrate. The conducting substrate comprises a thin layer of transparent conducting oxide (TCO) layer coated on a glass substrate. The TCO-layer is usually fluorine-doped tin oxide (F:SnO₂) or indium tin oxide (ITO).

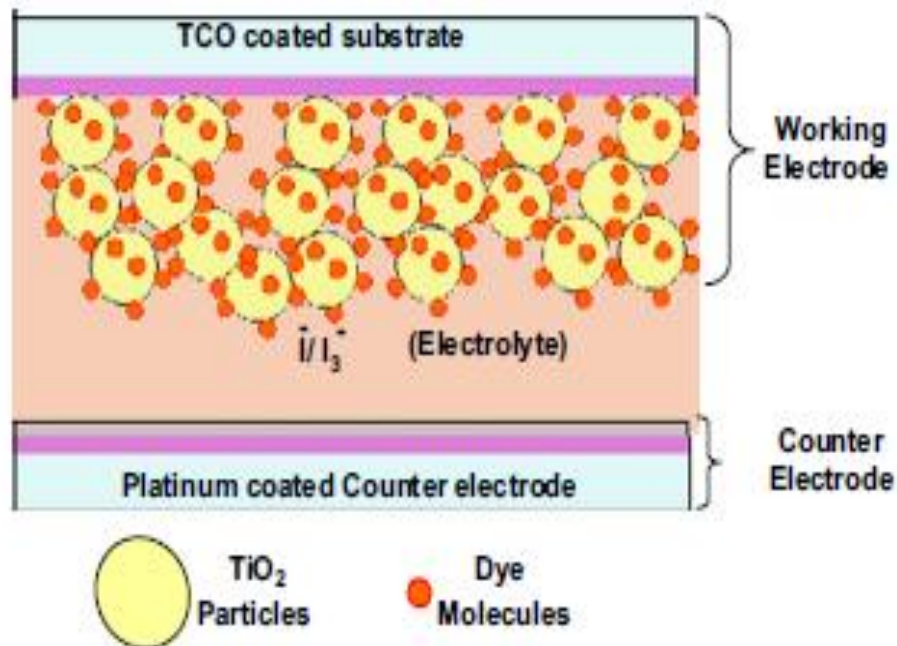


Figure 3.1: Structure of dye TiO₂ dye sensitized solar cell (Weerasinghe *et. al.*, 2013)

The working electrode is sensitized with a monolayer of dye molecules, which absorbs light and generates photoelectrons. Usually, a high specific surface area nanostructured layer is employed as a working electrode material in place of a flat semiconductor (Grätzel, 2005). This enables enhanced dye adsorption, thus resulting in a relatively high light absorption and consequently a higher overall photoconversion efficiency in the device. The counter electrode comprises a glass plate with a TCO-layer that is again coated on it a thin layer of platinum (Pt) catalyst.

A redox coupled electrolyte, usually a compound of iodine and iodide in organic solvent is used to fill the gap between the electrodes. The mesoporous film is prepared by methods such as sputtering or pressing semiconductor nanoparticles onto the conducting substrate. The film thickness varies from a few hundreds of nanometers to 30 μm , depending on the method of deposition and objective. The porous film has a characteristic internal area of 10²-10⁴ times larger than the projected cell area (Grätzel, 2003). The porosity of the mesoporous film, which is the percentage volume of voids or spaces not occupied by the semiconductor, is between 50-70 %. To seal the structure and avoid the leakage of redox couple electrolyte, a thermoplastic material, surlyn is sandwiched between the electrodes

whose thickness also determines the volume of electrolyte. The thermoplastic material has a typical thickness ranging from 25 to 60 μm .

Oxide semiconductor materials such as, ZnO, SnO₂ and TiO₂ have been employed in dye sensitized solar cells with TiO₂ being the most studied and used material. This is due to its outstanding performance for the reason of their physical and chemical stability, availability and non-toxicity, high refractive index, efficient photo catalytic activity, low cost among other advantages (Malliga *et. al.*, 2014). Investigations of TiO₂ have revealed that it is a material that is chemically resistant, highly transparent (60 - 95 %) in the visible, and also has a high refractive index (Pulker, 1984; Tang *et. al.*, 1994).

The studies on the structure of TiO₂ have shown that it exists in anatase or rutile when it is in crystalline form and in brookite when it is in amorphous form. The energy band gaps of anatase and rutile have been reported as 3.2 eV and 3.0 eV, respectively (Kim, 1996). Considering the aforementioned qualities, TiO₂ is a material of choice for the semiconductor in DSSCs combined with ruthenium complex dyes.

3.3 Operational principles of dye-sensitized solar cell

There are basically three stages in which a photovoltaic cell can operate; that is, light absorption, charge separation and charge collection. Unlike a conventional solar cell which is based on a *p-n* junction, the working principle of dye sensitized solar cell is based on the photogeneration of an electron by a dye, as similar to photosynthesis. Very important in a DSSC is a mesoporous layer consisting of nanometer-sized particles of a wide-band semiconductor oxide, such as TiO₂, ZnO or SnO₂, which are compacted to provide an electronic conduction. A complete operation scheme is presented in figure 3.2.

The oxidized dye is generated by the injection of an electron into the conduction band of the oxide as a result of photoexcitation of the sensitizer dye. After the electron is injected, the ground state of the dye is consequently reinstated by donation of an electron from the electrolyte reductant, which subsequently is regenerated by the reduction of the electrolyte oxidant at the counter-electrode (Grätzel, 2009; Listorti *et. al.*, 2011).

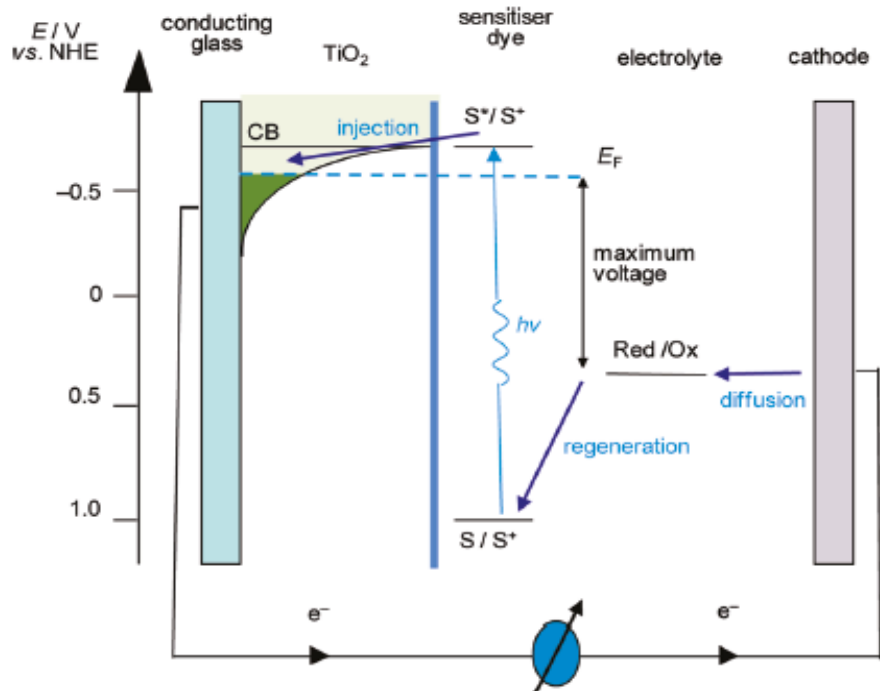


Figure 3.2: The operation principle of the dye-sensitized nanostructured solar cell (Listorti *et. al.*, 2011)

The difference between the Fermi level of the oxide and the redox potential of the electrolyte gives the voltage produced by the radiated cell (Liu *et. al.*, 2010). The process repeats itself, becoming self-sustaining with illumination (Smestad, 1998). Each of the components incorporated in a DSSC contributes well to the overall performance of the device. DSSCs can be fabricated at a sensible low cost and still giving out comparatively good efficiencies.

The sensitizer plays an essential role in dye sensitized solar cells. It absorbs photons and generate electrons that will eventually be injected into the conduction band of the semiconductor on which it is chemisorbed. The dye properties greatly influence the light harvesting efficiency (LHE) and the total photoelectric conversion efficiency of the solar cell. The energy diagram of a semiconductor/chromophore interface is shown in figure 3.3.

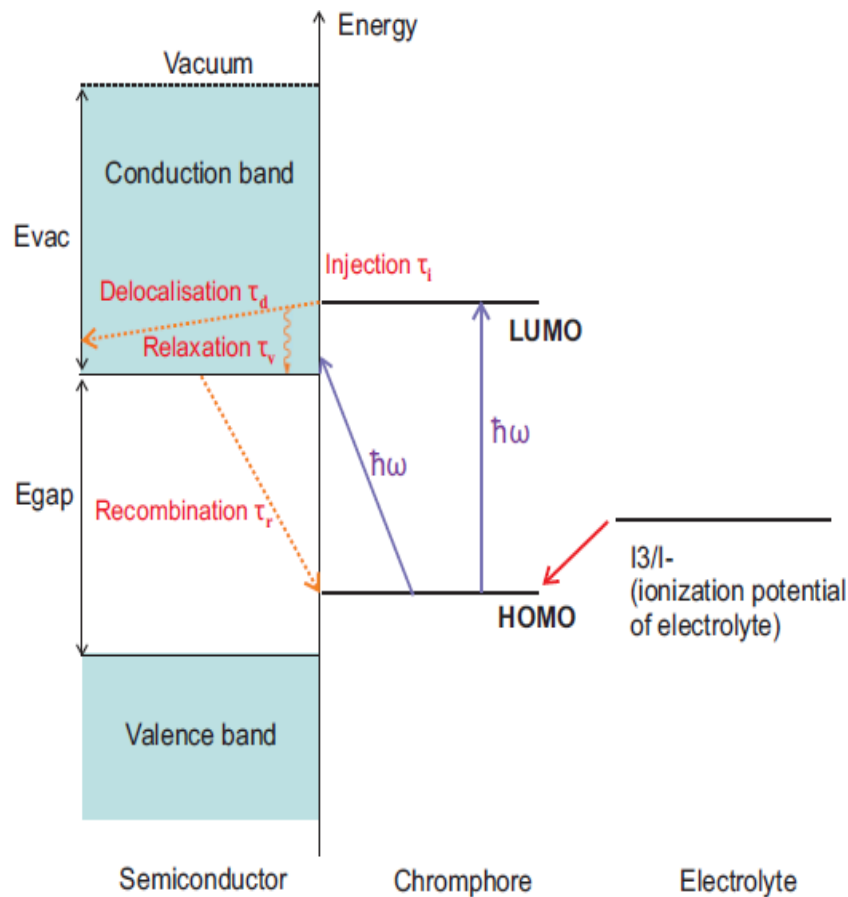


Figure 3.3: Schematic energy diagram of a semiconductor/chromophore interface (Smestad, 1998)

An electron in ground state is energized to excited state by the absorption of photon energy. Provided that the dye is energized levels of the Lowest Unoccupied Molecular Orbital (LUMO) and the semiconductor conduction band (CB) are in satisfactory positions, the electron in highest energetic orbital can proceed to the oxide material. For this reason, the dye in its excited state must have energy slightly above the semiconductor conduction band of the oxide, for the injection of the excited electrons to occur (Calzolari *et. al.*, 2011). In the same manner, the Highest Occupied Molecular Orbital (HOMO) level of the dye must be below the energy level of the redox potential of the electrolyte to allow for the dye regeneration (Calzolari *et. al.*, 2011). In this regard, a suitable choice of the dye/semiconductor and dye/electrolyte pairs is crucial for efficient DSSC. Also very important is the absorption of the sensitizer must range from Ultra Violet (UV) region to

Infra-Red (IR) region with an absorption peak in the visible region. In addition, the dye must be properly anchored to the semiconductor oxide surface in order to ensure a low charge transfer resistance and a stable chemical bond (Kong *et. al.*, 2007). To reduce the tendency of dye aggregation, some co-adsorbent additives such as chenodeoxycholic acid (CDCA) are usually employed together with the sensitizer (Mishra *et. al.*, 2009).

3.4 Electrochemistry of Semiconductor in photovoltaic

3.4.1 Semiconductor-electrolyte Interface (SEI)

A semiconductor material comprises a valence band and a conduction band separated by an energy band gap. The semiconductor band gap is relatively small which allows for electrons from the valence band to reach conduction band upon excitation. In the conduction band, the electrons become free and conducting. In the case of an insulator, the band gap is too wide for electron jump to the conduction band from the valence band under illumination. Metals have both valence and conduction bands overlapping, hence always conducting. The differences highlighted above are further illustrated in figure 3.4. The density of the conduction band electrons n_c , and the effective density of conduction band states N_c , defines the Fermi-level for electrons in a semiconductor. The distribution of states in the conduction band is given by equation 3.1 below (Sze, 1981);

$$N_c(E) = \frac{\sqrt{2}(m_{dos}^*)^{3/2} (E - E_c)^{1/2}}{\pi^2 \hbar^3} \quad (3.1)$$

where E is the energy of the state, E_c is the conduction band energy level and m_{dos}^* is the effective mass of the electron.

The Fermi-Dirac distribution function (Shockley & Read, 1952; Sze, 1981) in equation 3.2 gives the probability of an electron to occupy an energy level E , $f(E)$:

$$f(E) = \frac{1}{1 + e^{(E - E_f)/k_B T}} \quad (3.2)$$

where E_f is the energy of the Fermi level, K_B is Boltzmann constant and E is energy of the state.

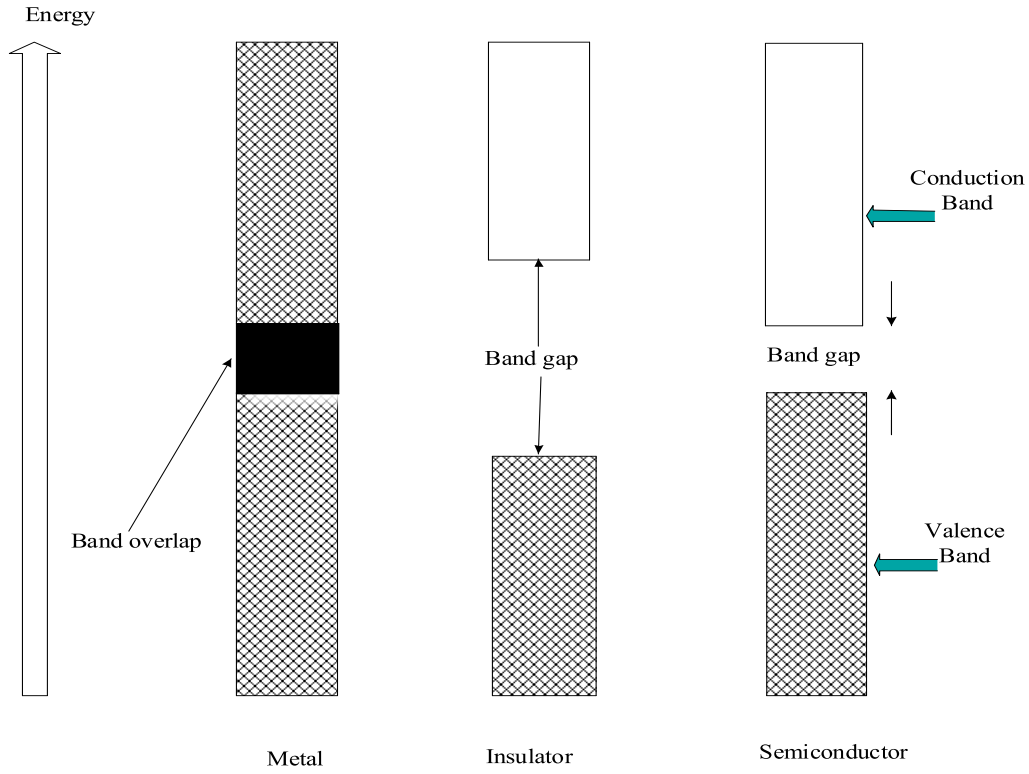


Figure 3.4: Schematic energy levels diagram for a metal, an insulator and a semiconductor

Taking the integral of the product of equations (3.1) and (3.2) results to the density of the conduction band electrons in the semiconductor, i.e. (Shockley and Read, 1952),

$$n_c = \int_{E_c}^{\infty} N_e(E) f(E) dE = \frac{\sqrt{2}(m_{dos}^*)^{3/2}}{\pi^2 \hbar^3} \int_{E_c}^{\infty} \frac{(E - E_c)^{1/2}}{1 + e^{\frac{E - E_f}{k_B T}}} dE \quad (3.3)$$

For low values of densities, the Fermi function is insignificant thereby not considered, then the equation becomes

$$n_c = N_c \frac{E - E_c}{e^{k_B T}} \quad (3.4)$$

where N_c is the effective density of the states. From equation (3.4), the relation for energy of the Fermi level in the bulk semiconductor can thereby be determined and is obtained as:

$$E_f = E_c + k_B T \ln\left(\frac{n_c}{N_c}\right) \quad (3.5)$$

It is also important to discuss the Fermi level in the redox electrolyte because the dye sensitized solar cell possesses an electrolyte-semiconductor interface. However, this is defined for ideal solutions, from the relation between the concentration of oxidized (Ox) and reduced species (Red) that is



If the redox level, E_{redox} , of the electrolyte solution is lower compared to Fermi energy E_F in the semiconductor, for example the electrolyte consists of strong oxidants, clearly the electrons will transmit through the *SEI* from the semiconductor into solution until the equilibrium will be attained (that is, $E_F = E_{redox}$). The electron transfer from the semiconductor into solution will make the valence and conduction bands to shift comparatively to the Fermi level, which is to curve upwards (Bard & Faulkner, 2000). This condition is displayed in Figure 3.5. Such reactions are governed by the Nernst equation, which relates the Fermi level of the redox electrolyte, $E_{f, redox}$ with its reduced, C_{red} , and oxidized, C_{ox} , species in solution, given a standard electrode potential, E° (Bard & Faulkner, 2000), that is

$$E_{f, redox} = E^\circ + k_B T \ln \left(\frac{C_{ox}}{C_{red}} \right) \quad (3.7)$$

The standard reference electrode commonly employed in electrochemical investigation is the saturated calomel electrode (SCE) made up of Hg/Hg₂Cl₂/KCl saturated in water. Also commonly used as reference electrode is normal hydrogen electrode, commonly referred to as NHE. Taking the difference between (3.7) and (3.5) results in the difference in Fermi level between the semiconductor and the redox electrolyte which defines the potential gradient referred to as the potential, V as reported in (Memming, 1980; Grätzel, 2005),

$$V = \frac{E_f - E_{f, redox}}{e} \quad (3.8)$$

where E_f and $E_{f, redox}$ are the Fermi energies of the semiconductor and electrolyte respectively, and e is the electron charge.

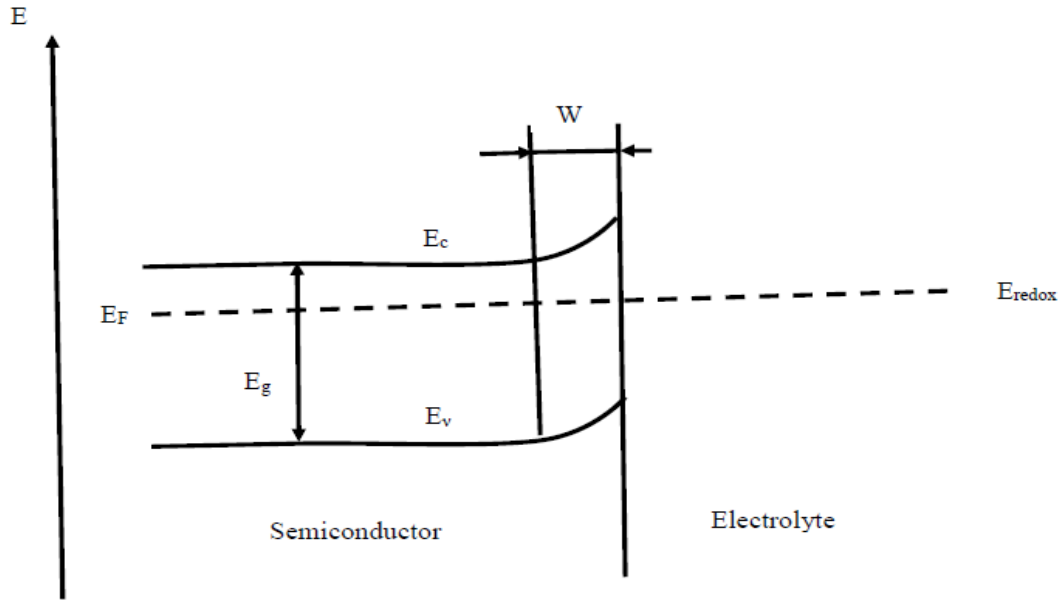


Figure 3.5: Schematic energy diagram of semiconductor-electrolyte interface (Memming, 1980)

This represents the thermodynamic driving force for electrons to have a net flux at the interface between the materials. The potential is also the V_{oc} of the cell and the maximum V_{oc} a cell can attain is defined by the difference between the quasi Fermi level of the semiconductor and the redox potential of the electrolyte.

At the semiconductor/electrolyte interface and in the bulk of the electrolyte, the following processes mainly take place:

1. mass movement of electrons under the effect of potential gradient,
2. movement of redox species under the impact of concentration gradient and
3. movement of fluids due to convections caused by density gradients.

All these processes can be given by the transport equation (Bard & Faulkner, 2000)

$$J_i(x) = -D_i \frac{\partial C_i(x)}{\partial x} - \frac{Z_i F}{RT} D_i C_i \frac{\partial \phi(x)}{\partial x} + C_i v(x) \quad (3.9)$$

where $J_i(x)$ is the flux of species i (mol sec⁻¹ cm⁻²) at a distance x from the surface, D_i is the diffusion coefficient (cm²sec⁻¹), $\partial C_i(x)/\partial x$ is the concentration gradient at a distance x , $\partial(\phi)(x)/\partial x$ is the potential gradient, z_i , and C_i , are the charge and concentration of

species i , respectively, and $v(x)$ is the velocity (cm sec^{-1}) with which a volume element in solution moves along the axis. The three terms on the right hand side of equation (3.9) stand for the contributions of diffusion, migration and convection, respectively, to the flux.

The technique commonly employed in the investigation of electrochemical processes is cyclic voltametry (CV) which comprises a potentiostat and a cell that holds the analyte to be investigated. The cell is made up of three electrodes; working (WE), reference electrode (RE) and counter electrode (CE). The set-up of this study is as shown figure 3.6.

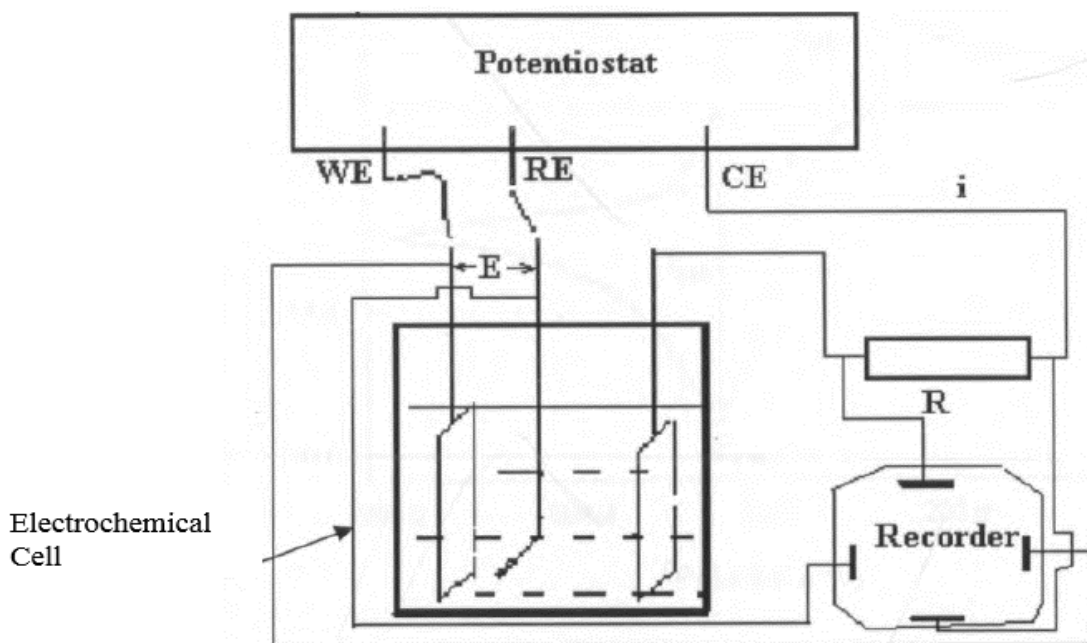


Figure 3.6: Electrochemical measurement system showing the working electrode (WE), reference electrode (RE) and counter electrode (CE) (Simiyu, 2010).

Current is usually measured between WE and CE as the potential is applied between WE and RE. The working electrode is responsible for the provision of a surface for electron transfer for the system under study. The potential of the electrode (versus NHE via RE) is cyclically scanned typically at a rate of 1 - 100 mV/s between two end points, and the consequential current is examined. In this manner, it makes it possible to tell at which potential an electrochemical reaction occurs by the observation of peak current. A typical CV profile for a system whose concentration of species is described by the Nernst equation is illustrated in figure 3.7.

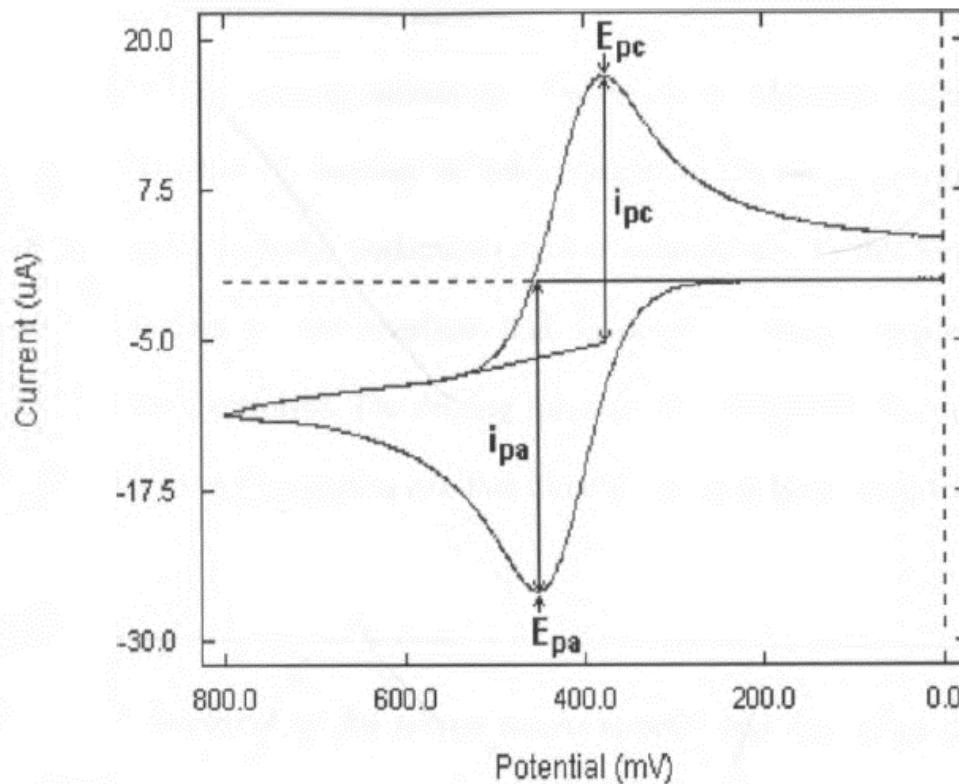


Figure 3.7: An ideal cyclic voltammogram for a reversible single electrode transfer reaction showing important peak parameters. E_{pc} and E_{pa} are cathodic and anodic peak potentials, respectively while i_{pc} and i_{pa} are cathodic and anodic peak currents respectively (Simiyu, 2010)

To derive the redox potential E° of the solution, there has to be an interpolation between the cathodic peak potential (E_{pc}) and the anodic peak potential (E_{pa}) which are oxidation and reduction peaks, respectively. More information that is derivable from a cyclic voltammogram is the reversibility and kinetics of the system. Many effects in electrochemical reactions can alter a typical voltammogram making it differ from the one shown in figure 3.7. These include:

1. when the redox reaction is irreversible,
2. slow reaction as a result of slow diffusion and
3. many reactions occurring at the same time

3.4.2 Processes of charge transfer at the semiconductor electrolyte interface (SEI)

The processes of charge transfer across the SEI are mainly oxidation or reduction reaction of redox species in the electrolyte resulting in anodic and cathodic current respectively. In such a process, a chemical reaction takes place at the interface that involves a charge transfer between the semiconductor and the electrolyte. The driving force for the charge net flow at the *SEI* is the bias potential which drives the reaction in either direction leading to a charge transfer process (Memming, 1980)

3.4.3 Band bending

The Fermi-level of electrons in the n-type semiconductor and the redox potential in the electrolyte are same between the semiconductor and the electrolyte at equilibrium (figure 3.8). Provided that the system is in equilibrium, electrons can move from the semiconductor to the electrolyte by the process of diffusion. This possibly leads to the formation of a depletion layer due to build-up in electric field at SEI which prevents further movement of electrons to the electrolyte. In this regard, the energy of the electrons near the semiconductor-electrolyte contact is affected by the electrical field in the depletion layer, with those near the interface with stronger effect, a situation that results to band bending (figure 3.8), (Memming, 1980; Södergren *et. al.*, 1994).

At the Fermi level, E_f , the depletion layer vanishes giving way for flat-band potential. For nanometer-sized particles, the distances are too short within the particle for the depletion to build up therefore a constant potential within the particle is assumed. The potential distribution for a spherical particle which projected the aggregate band bending for small particles of radius r , was first solved by Albery and Bartlett, (1984),

$$\Delta\phi_{sc} = \frac{k_B T}{6e} \left(\frac{r}{L_D} \right)^{1/2} \quad (3.10)$$

where e is electron charge. L_D is the Debye length given by

$$L_D = \sqrt{\frac{\epsilon \epsilon_o k_B T}{2e^2 N_D}} \quad (3.11)$$

where ϵ_0 is permittivity of free space and ϵ is dielectric property and N_D is donor density.

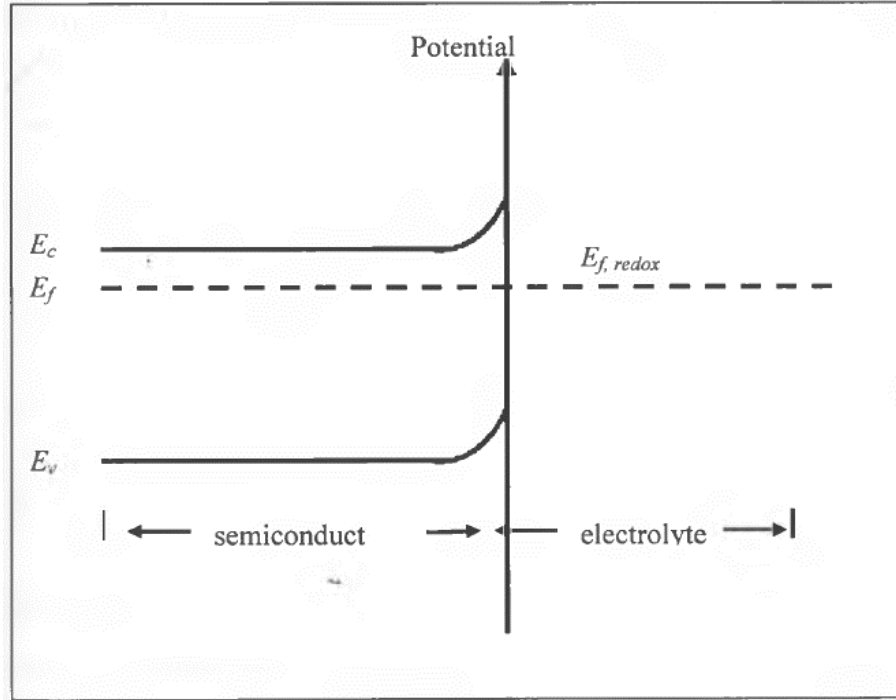


Figure 3.8: Band bending at the semiconductor-electrolyte interface for n-type semiconductor (Memming, 1980).

3.5 Dye sensitization

In a non-sensitized photoelectrochemical solar cell, electrons get excited and are transferred from the valence band to the conduction band as light is absorbed in the semiconductor producing electron-hole pairs. This absorbed photon energy is transformed to electrical energy as the produced charges are separated at the semiconductor-electrolyte interface (Listorti *et. al.*, 2011). However, in the situation of the dye sensitized solar cell, charge carriers are generated by electron (or hole) injection from the excited dye instead of band gap excitation. Figure 3.9 illustrates its energy scheme and principle of operation. Upon the illumination of an n-type semiconductor such as TiO_2 , the dye gets excited from its ground state S to S^* as shown in figure 3.9 (part a) and equation 3.12 (a). When in the excited state S^* , the dye molecule injects an electron into the conduction band of TiO_2 (figure 3.9 (part b) and equation 3.12(b)) and also gets oxidized (S^+) in the process. The oxidized dye molecule is reduced to ground state (figure 3.9 (part c) and equation 3.12(c)) by the redox couple available in the electrolyte accepting electron from the counter electrode.

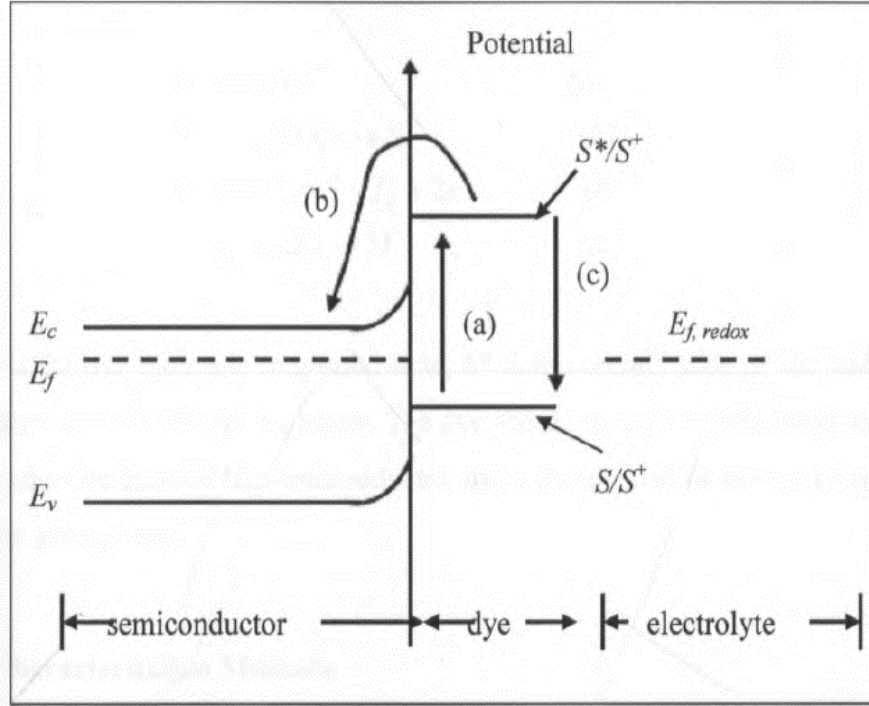


Figure 3.9: Dye sensitized semiconductor-electrolyte interface electrode illumination (Simiyu, 2010)

The reaction in (part b) occurs when the dye is in close contact with the semiconductor surface at the excited state lifetime and more to that, the energy level of the dye is above the conduction band of the semiconductor. All the chemical reaction processes described above are summarized in equation (3.12):



where S is the ground state of the dye molecule, S^* is the dye molecule in excited state and S^+ is the dye molecule in oxidized state.

3.6 Electrical characterization

The electrical resistivity of a material quantifies the magnitude of opposition that material offers to the flow of electricity. If electricity can flow with ease via a material, that material has low resistivity. If electricity finds it excessive difficult to flow via a material, that material possesses high resistivity (Valdes and Member, 1954). Electrical resistivity is a vital physical property of all materials. It is always essential to precisely measure the resistivity of any given material. The electrical resistivity of varying materials at room temperature can differ by over 20 orders of magnitude. Electrical conductivity is defined as the reciprocal of the resistivity. That is to say, high resistivity means low conductivity, and a low resistivity means high conductivity for that material. Figure 3.10 shows a simple model of electricity flowing through a material under applied voltage. The white circle represents an electron which moves from left to right through the material. The black solid circles are the stationary atoms of the material. Electrical resistivity is caused by the constant collisions between the two.

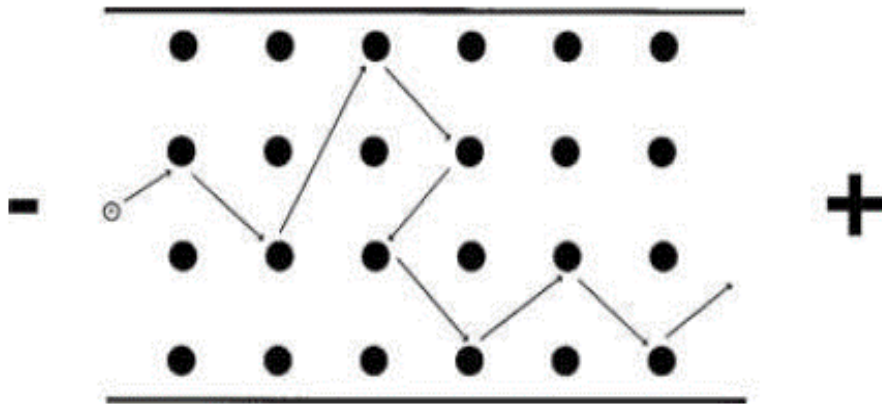


Figure 3.10: Simple model of electricity flowing through a material under an applied voltage (Valdes and Member 1954).

At microscopic level, electricity is the movement of electrons through a material. There are actually many of them going round simultaneously but one is used for ease of explanation. The electron moves from the left side of the material to the right side due to an external force which is normally an applied voltage (denoted by the plus and minus signs). The electron collides with the “stationary” atoms as it continues moving through the material.

These several collisions tend to slow down the electron. The number of collisions between electron and atoms vary with materials. A material that produces more collisions is highly resistive and that which produces less collisions is a low-resistivity material. Temperature greatly influences the resistivity of a material.

The sheet resistance of thin films are computed by several models and equations. The model shown in figure 3.11 is employed in computing the resistivity of a semi-infinite sample of a semiconductor material.

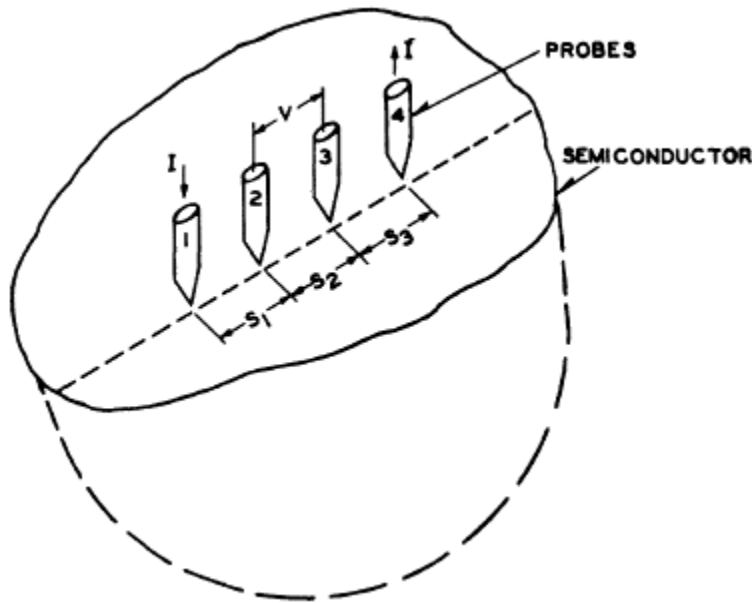


Figure 3.11: Model for the four point probe resistivity measurement (Valdes and Member, 1954)

The resistivity is computed as (Valdes and Member, 1954)

$$\rho = \frac{V}{I} \frac{2\pi}{\frac{1}{S_1} + \frac{1}{S_2} - \frac{1}{S_1 + S_2} - \frac{1}{S_2 + S_3}} \quad (3.13)$$

where, V is the floating potential between the inner probes in volts, I is current through the outer pair of probes in amps, S_1, S_2, S_3 are the point spacing in cm and ρ is resistivity in ohm-cm.

when $S_1 = S_2 = S_3 = S$ equation (3.13) becomes

$$\rho = \frac{V}{I} 2\pi s \quad (3.14)$$

Since conductivity is the inverse of resistivity,

$$\sigma = \frac{1}{\rho} \quad (3.15)$$

where, σ is conductivity of the material measured in Siemens or $\Omega^{-1}\text{cm}^{-1}$

Equation (3.14) represents the resistivity of a sheet of material. In case of a thick film, resistivity is given thus:

$$\rho = R_s \times t \quad (3.16)$$

where, R_s is sheet resistance and t is the film thickness.

$$R_s = \frac{\pi}{\ln 2} \frac{V}{I} \equiv 4.53 \frac{V}{I} \quad (3.17)$$

Combining (3.16) and (3.17),

$$\rho = 4.53 \frac{V}{I} \times t \quad (3.18)$$

3.7 Optical characterization

In this section, we discuss optical properties of semiconductor thin films. These properties include absorption, reflectivity, transmittance, band gap, extinction coefficient and refractive index. Information about these properties are critical in the choice of materials for solar cells.

3.7.1 Transmittance and reflectance

The optical behavior of a material is used to obtain its optical constants such as refractive index n and extinction coefficient, k . Reflection is the process whereby electromagnetic radiation is reverted at the boundary between two media known as surface reflection or at the inner part of a medium known as volume reflection, whereas transmission is the passage of electromagnetic radiation via a medium. The two processes can be accompanied by scattering, which is the process of rebounding a unidirectional beam into diverse directions. In this situation, scattering is either referred to as diffuse reflection or as diffuse transmission. When no diffusion occurs, reflection or transmission of a unidirectional beam results in a unidirectional beam according to the laws of geometrical optics (Figure 3.12).

In this situation, they are either regular reflection or transmission. The frequency of radiation remains the same whether it is reflection, transmission or scattering that occurs.

Reflectance and transmittance can be employed to define the optical properties of materials. The quantities are applicable to either complex radiation or to monochromatic radiation. The optical properties of materials are not a constant for the reason that they depend on many parameters which include: thickness of sample, surface conditions, angle of incidence, temperature, polarization effects and spectral composition of the radiation.

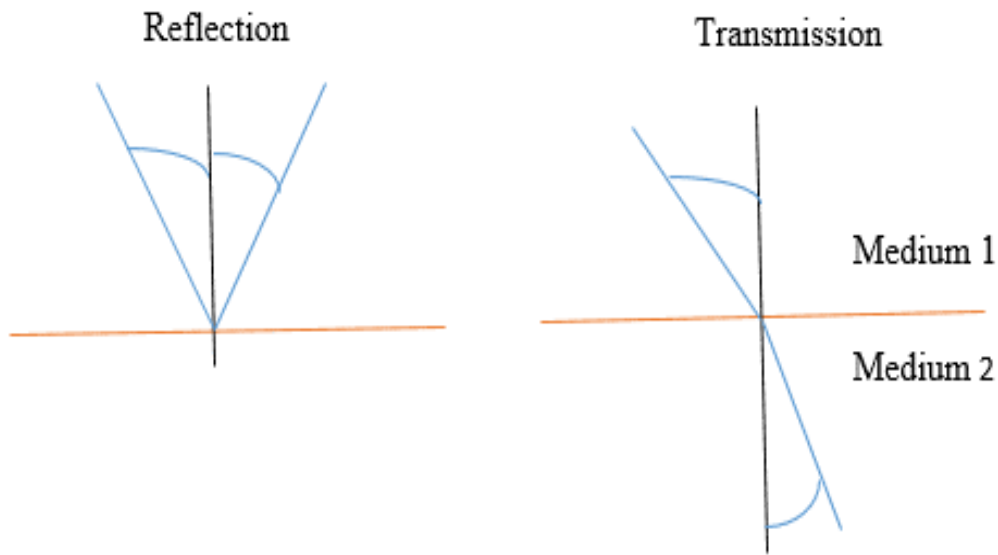


Figure 3.12: A typical transmission and reflection of a unidirectional beam (Weisstein, 2017)

The transmittance and reflectance spectra of thin films can be measured by UV-Vis spectrophotometer to the variation of these spectra with wavelengths. Transmittance provides information on how much light intensity gets to the semiconductor and dye. Reflectance on the other shows how much light intensity is reverted back from the thin films. The transmittance of a thin film is given (Yakuphanoglu *et. al.*, 2004)

$$R = (1 - T)^2 e^{-\alpha d} \quad (3.19)$$

where, T is transmittance, R is reflectance, d is the film thickness and α is absorption coefficient.

However, at shorter wavelengths near the optical band gap, the scattering losses are dominated by the fundamental absorption and the following relation is often used (Mardare *et. al.*, 2000)

$$\alpha = \frac{1}{d} \ln\left(\frac{1}{T}\right) \quad (3.20)$$

The reflectance R , the refractive index n , and the extinction coefficient k of crystalline solids are related through the relations (Aksay and Altiookka, 2007):

$$R = \frac{(n-1)^2 + k^2}{(n+1)^2 + k^2} \quad (3.21)$$

Solving for n in (3.21),

$$n = \frac{1+R}{1-R} + \sqrt{\frac{4R}{(1-R)^2} - k^2} \quad (3.22)$$

$$k = \frac{\alpha\lambda}{4R} \quad (3.23)$$

3.7.2 Absorption

The best direct and probably the simplest technique for probing the band structure of semiconductors is to measure the absorption spectrum. In the process of absorption, a photon of a known energy excites an electron from a lower to a higher energy state. Therefore, by introducing a piece of semiconductor at the output of a monochromator and investigating the variations in the transmitted radiation, the possible transitions of an electron and its distribution of states can be understood. Absorption is expressed in terms of a coefficient $\alpha(h\nu)$ which is defined as the relative rate of decrease in light intensity $L(h\nu)$ along its propagation path (Pankove, 1990):

$$\alpha = \frac{1}{L(h\nu)} \frac{d[L(h\nu)]}{dx} \quad (3.24)$$

where h is Planck's constant, ν is frequency and x is the propagation path length.

3.7.3 Allowed and forbidden transitions

Take the case of absorption transitions between two direct valleys where all the momentum conserving transitions are allowed (figure. 3.13), which means the probability of transition;

P_i does not depend on the photon energy. In such a situation, each initial state at E_i is associated with final state at E_f , thus (Pankove, 1990):

$$E_f = hv - |E_i| \quad (3.25)$$

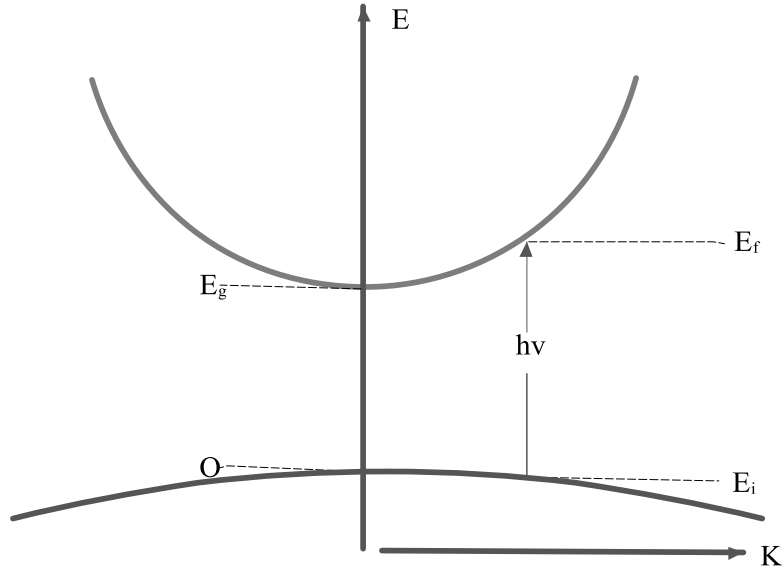


Figure 3.13: Absorption transitions between two direct valleys that are allowed (Pankove, 1990)

Substituting for band gap, E_g and solving equation 3.25

$$E_f - E_g = \frac{\hbar^2 k^2}{2m_e^*} \quad (3.26)$$

$$E_i = \frac{\hbar^2 k^2}{2m} \quad (3.27)$$

Adding the two preceding equations and substituting hv for $E_f - E_i$,

$$hv - E_g = \frac{\hbar^2 k^2}{2} \left(\frac{1}{m_e^*} + \frac{1}{m_h^*} \right) \quad (3.28)$$

The density of directly associated states can thus be estimated:

$$N(hv)d(hv) = \frac{8\pi k^2 dk}{(2\pi)^3}$$

$$= \frac{(2m_r)^{3/2}}{2\pi^2\hbar^3} (hv - E_g)^{1/2} d(hv) \quad (3.29)$$

where, m_r is known as the reduced mass expressed as

$$\frac{1}{m_r} = \frac{1}{m_e^*} + \frac{1}{m_h^*} \quad (3.30)$$

Hence the absorption coefficient is

$$\alpha(hv) = A^* (hv - E_g)^{1/2} \quad (3.31)$$

where A^* is given by:

$$A^* \approx \frac{q^2 \left(2 \frac{m_e^* m_h^*}{m_e^* + m_h^*}\right)^{3/2}}{nch^2 m_e^*} \quad (3.32)$$

Figure 3.14 shows the direct band gap of TiO₂ thin film obtained by the application of equation 3.26 known as Tauc's equation and figure 3.15 is the case of an indirect band gap also obtained from same equation.

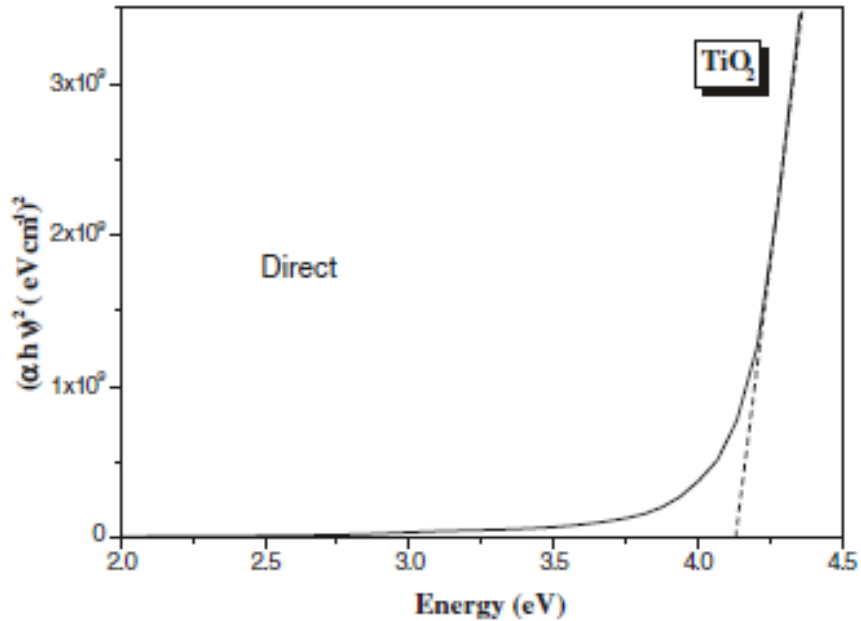


Figure 3.14: Plot of $(\alpha h\nu)^2$ against $(h\nu)$ for the estimation of the direct gap energy value (Ghraiiri and Bouaicha, 2012).

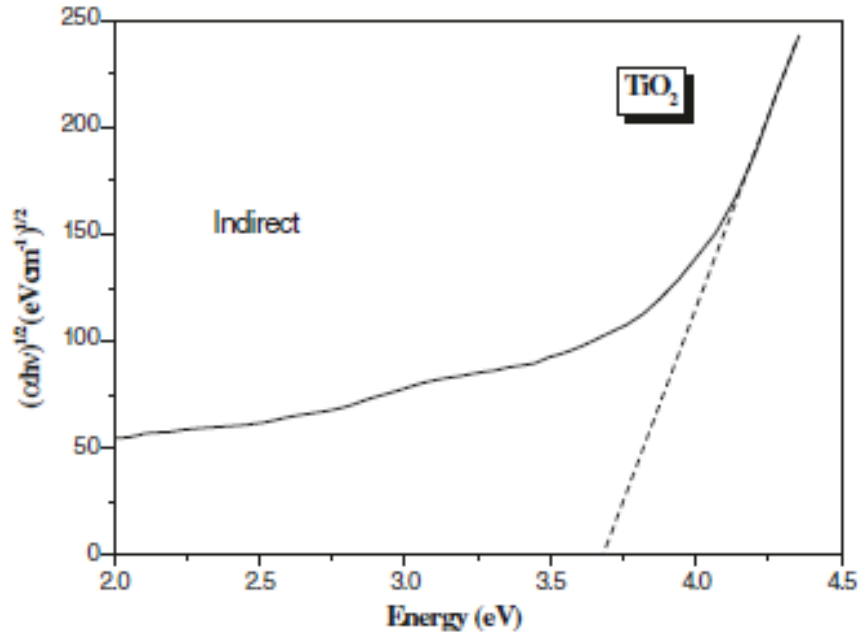


Figure 3.15: Plot of $(\alpha hv)^{1/2}$ against (hv) for the estimation of the indirect gap energy value (Ghrairi and Bouaicha, 2012).

However, in some materials, quantum selection rules forbid direct transitions at $k=0$ but allow them at $k \neq 0$ the probability of transition increases with k . In the model shown in Figure 3.14 it shows that the probability of transition increases directly to $(hv-E_g)^{1/2}$. For the reason that the density of states linked in direct transitions is related to $(hv-E_g)$, the absorption coefficient has the following spectral dependence (Pankove, 1990):

$$\alpha(hv) = A'(hv - E_g)^{3/2} \quad (3.33)$$

where,

$$A' = \frac{4}{3} \frac{q^2 \left(\frac{m_e^* m_h^*}{m_e^* + m_h^*} \right)^{5/2}}{nch^2 m_e^* m_h^* hv} \quad (3.34)$$

3.8 Characterization methods

3.8.1 X-ray diffraction (XRD)

X-rays are electromagnetic radiation of high energy, ranging from about 200 eV to 1 MeV. The production of X-rays takes place in an x-ray tube comprising two electrodes in a

vacuum chamber. An incident electron with a sufficient energy ejects an inner-shell electron, the atom is left in an excited state but with a hole instead in the electron shell. In an event that the hole is filled from an outer shell, an x-ray photon whose energy is equivalent to the difference in the electron energy levels is produced. This energy is characteristic of the target material and is exhibited in form of high intensity peaks which are used for diffraction analysis. These x-rays when focused on a material, get scattered by the atoms in specific directions according to Bragg's law given by (Suryanarayana and Norton, 1998),

$$\lambda = 2nd_{hkl} \sin \theta \quad (3.35)$$

where λ is the wavelength of the x-rays, d_{hkl} is the inter-planar spacing of the crystal and θ is the angle of incidence.

Equation (3.30) is employed in the analysis of the diffraction patterns of samples and therefore applied for the identification of elements and crystal orientation. The diffraction pattern of the sample is obtained by the plot of peak intensities against measured diffraction angle (2θ) on y and x axes respectively. The diffraction pattern has a series of peaks that correspond to x-rays diffracted from a specific set of planes in the specimen. The pattern is usually determined by the powder diffraction file (PDF) standard from the reference library for Barium Titanate (Remmel *et. al.*, 1999). The peaks positions are influenced by the crystal structure (shape and size of the unit cell) of the sample material that facilitates the determination of structure and lattice parameter of the material. In real sense, the actual patterns differ slightly from the standard due to the peak broadening as a result of the size of the crystal and the overlapping of peaks.

In addition to identifying peaks, XRD provides information about the crystal sizes of the samples. Scherrer's formula given by Suryanarayana and Norton, (1998) is used to calculate crystal sizes of the samples.

$$Size = \frac{180}{\pi} \frac{k\lambda}{\cos \sqrt{(FWHM)^2 - S_i^2}} \quad (3.36)$$

where k is the Scherrer's constant (0.89) which is the ratio of the full width at half maximum (FWHM) and integral breadth, S_i is the instrument broadening (assumed to be 0), λ represents the wavelength of the incident radiation (1.54Å for the instrument used).

3.8.2 Current-voltage characterization

Solar energy is made of an electromagnetic spectrum of wavelengths stretching ultraviolet (UV), visible and infrared regions. From the theory of blackbody radiation, the energy density per wavelength, $\frac{de_r}{d\lambda}$ can be written as a function of wavelength (λ) as (Wüfel, 2005)

$$\frac{de_r(\lambda)}{d\lambda} = \frac{2hc_o d\Omega}{d\lambda} \frac{1}{e^{hc/\lambda k_B T} - 1} \quad (3.37)$$

where $d\Omega$ is a solid angle element, c is velocity of light within the medium, k_B is Boltzmann's constant and h is Plank's constant. Maximum density per wavelength is obtained from taking the square and equating to zero, $de_r/d\lambda$. Thus,

$$\lambda_{\max} = \frac{hc}{4965k_B T} = \frac{0.2497}{k_B T} \mu\text{meV} \quad (3.38)$$

The power density at the sun's surface is 62 MWm^{-2} but reaches just outside the earth's atmosphere as 1353 Wm^{-2} . As it passes through the atmosphere, the spectrum is somewhat absorbed by atmospheric components (that is, oxygen, Ozone, water vapor, carbon dioxide and methane). This attenuation is described by the 'Air Mass' (AM) factor since the absorption is directly proportional to the mass of air through which radiation passes. AM is given as l/l_o where l_o represents thickness of the atmosphere, l is the path length through which the radiation passes at an incident angle α with respect to the earth's surface normal. Thus l is expressed as,

$$l = l_o \cos \alpha \quad (3.39)$$

AM0 is the spectrum outside the atmosphere and AM1 is that on the earth's surface for perpendicular incidence. The standard spectrum for moderate weather is AM 1.5, which matches a solar incident angle of 48° with respect to the surface normal, thereby resulting to an average irradiance of 1000Wm^{-2} .

Current-voltage (I - V) measurement defines the I - V response of the solar cell device, i.e., I - V characteristics of the device ranging from the dark to under diverse light intensities. In the dark, the solar cell device exhibits the properties of an ideal diode in which the applied voltage (known as bias voltage) on the device produces current in the opposite direction with respect to light generated current. This kind of current is known as dark current and is expressed by (Sze, 1981),

$$I_{dark} = I_s (e^{eV/kT} - 1) \quad (3.40)$$

where I_s is the saturation current, V is the applied voltage and e is the elementary charge. Under irradiation, the I - V characteristics are of the form:

$$\begin{aligned} I &= I_{ph} - I_s (e^{eV/kT} - 1) \\ &= I_{ph} - I_s (e^{V/V_T} - 1) \end{aligned} \quad (3.41)$$

where I_{ph} is the photo-generated current and V_T is the thermal voltage ($k_B T/e$).

In the case of real devices, the ideality factor m is employed to define the reliance of dark current on voltage, hence the equation (Nelson, 2003),

$$I = I_{ph} - I_s (e^{V/mV_T} - 1) \quad (3.42)$$

Equation 3.42 can be achieved experimentally by the plot of photocurrent against applied bias to give a typical curve referred to as the current- voltage (I - V) characteristics curve (Figure 3.16). Essential parameters of a cell namely open circuit voltage (V_{oc}), short circuit

current (I_{sc}), fill factor (FF) and the total power conversion efficiency can be deduced from the I - V curve.

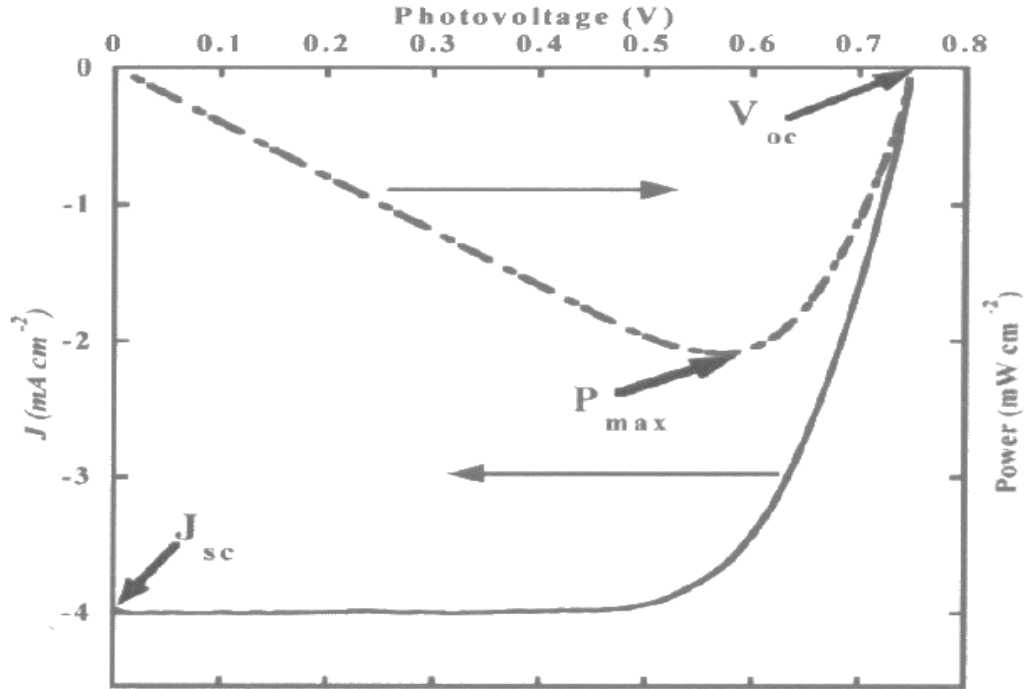


Figure 3.16: A typical I - V curve showing variation of current with voltage and corresponding power curve (Nelson, 2010).

3.8.2.1 Open-circuit voltage (V_{oc})

Measurement of V_{oc} is carried out under an open circuit condition (infinite external load and zero power). External current does not flow between the two terminals in this circumstance, i.e. $I=0$ and $V=V_{oc}$. Hence, V_{oc} is derived from equation (3.41) by (Nelson, 2003),

$$I_{ph} - I_s \left(e^{\frac{V_{oc}}{mV_T}} - 1 \right) = 0 \quad (3.43a)$$

$$V_{oc} = mV_T \ln \left(\frac{I_{ph}}{I_s} + 1 \right) \equiv mV_T \ln \left(\frac{I_{ph}}{I_s} \right) \quad (3.43b)$$

Equation (3.43b) shows that the value of V_{oc} increases logarithmically with photogenerated current and light intensity.

3.8.2.2 Short-circuit current (I_{sc})

Short-circuit current (I_{sc}) is obtained when the applied voltage is zero, that is., the circuit is shorted, and the external load and power are equal to zero. In this case, equation (3.43a) becomes

$$I_{sc} \equiv I_{ph} \quad (3.44)$$

This shows, I_{sc} increases linearly with light intensity.

3.8.2.3 Fill factor (FF)

The product of photocurrent and the applied voltage gives the output power of the solar cell device. Output power is zero when $I=I_{sc}$ and $V=V_{oc}$, which is the situation whereby no external work can be done. In between short circuit and open circuit, at some potential, a maximum output power (P_{max}), shows up as seen in figure (3.16). This is the point at which the device delivers the maximum power output with the voltage, V_{mp} and the current I_{mp} .

$$V_{mp} = V_{oc} - mV_T \ln\left(\frac{V_{mp}}{V_T} + 1\right) \quad (3.45)$$

FF is defined as follows:

$$FF = \frac{V_{mp} I_{mp}}{V_{oc} I_{sc}} \quad (3.46)$$

which expresses the way the maximum power rectangle fits under the I - V curve. Combining (3.40) and (3.41) produces an approximation for FF as in equation (3.37)

$$FF = \frac{\frac{V_{oc}}{mV_T} - \ln\left(1 + \frac{V_{oc}}{mV_T}\right)}{1 + \frac{V_{oc}}{mV_T}} \quad (3.47)$$

Fill factor values for DSSC are commonly within the range of 0.5 to 0.8 depending on the device. The series resistance (R_s) arising from the internal resistance and resistive contacts of the cell plays a vital role on FF and so also, shunt resistance (R_{sh}) due to the leakage of current. An equivalent circuit for a solar cell illustrating R_s and R_{sh} is displayed in figure 3.17.

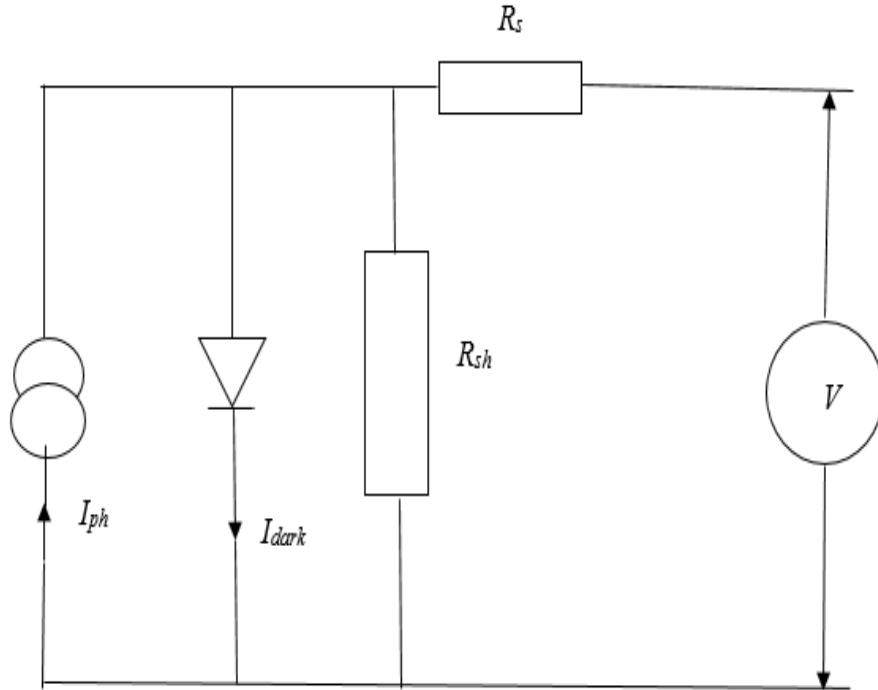


Figure 3.17: An equivalent circuit for a solar cell showing the series (R_s) and shunt (R_{sh}) resistances (Sze, 1981)

3.8.2.4 Solar-to-electric power conversion efficiency (η)

The conversion efficiency (η) describes the overall performance of the device and is defined as the ratio of the maximum power (P_{max}) to the power of incident radiation (P_{in}). Mathematically, power conversion efficiency is given by

$$\eta = \frac{V_m I_m}{P_{in}} = \frac{V_{oc} I_{sc} FF}{P_{in}} \times 100\% \quad (3.48)$$

The standard test conditions at which P_{in} is usually include *AM* 1.5 spectrum illumination, incident power density of 100 mWcm^{-2} and at 298K .

3.9 Electrochemical impedance spectroscopy

It is known that the concept of electrical resistance is the ability of a circuit element to resist the flow of electrical current. Ohm's law in equation 3.49 defines resistance in terms of the ratio between voltage, E , and current, I .

$$R = \frac{E}{I} \quad (3.49)$$

Though is a known established relationship, its application its application is limited to only one circuit element which is the ideal resistor. An ideal resistor has several simplifying properties:

1. It follows Ohm's Law at all current and voltage levels.
2. Its resistance value is independent of frequency.
3. AC current and voltage signals though a resistor are in phase with each other.

However, the real world contains circuit elements that exhibit much more complex behavior. These elements force us to abandon the simple concept of resistance, and in its place we use impedance, a more general circuit parameter. Like resistance, impedance is a measure of the ability of a circuit to resist the flow of electrical current, but unlike resistance, it is not limited by the simplifying properties listed above.

Electrochemical impedance is usually measured by applying an AC potential to an electrochemical cell and then measuring the current through the cell. Assume that we apply a sinusoidal potential excitation. The response to this potential is an AC current signal. This current signal can be analyzed as a sum of sinusoidal functions (a Fourier series).

The excitation signal, expressed as a function of time, has the form

$$E_t = E_o \sin(\omega t) \quad (3.50)$$

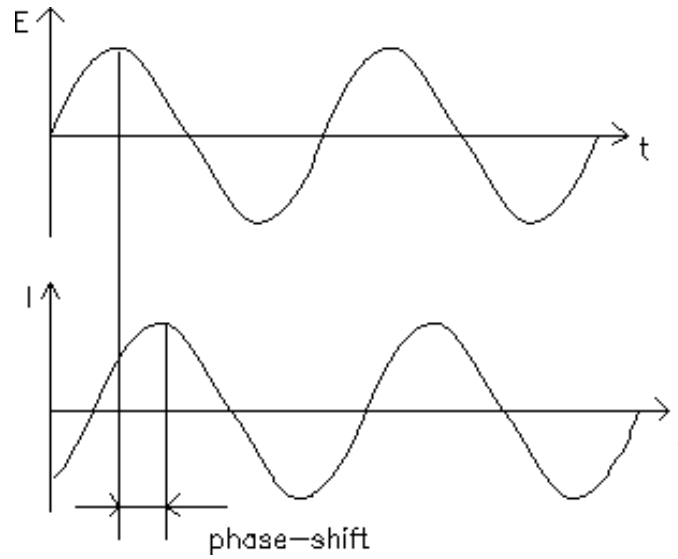


Figure 3.18. Sinusoidal current response in a linear system (<https://www.gamry.com>)

where E_t is the potential at time t , E_0 is the amplitude of the signal, and ω is the radial frequency. The relationship between radial frequency ω (expressed in radians/second) and frequency f (expressed in hertz) is:

$$\omega = 2\pi f \quad (3.51)$$

In a linear system, the response signal, I_t , is shifted in phase (Φ) and has a different amplitude than I_0 .

$$I_t = I_0 \sin(\omega t + \Phi) \quad (3.52)$$

An expression analogous to Ohm's Law allows us to calculate the impedance of the system as:

$$Z = \frac{E_0}{I_t} = \frac{E_0 \sin(\omega t)}{I_0 \sin(\omega t + \Phi)} \quad (3.53)$$

CHAPTER FOUR

EXPERIMENTAL METHODS

4.1 Introduction

In this chapter, appropriate experimental details of preparation of the device, characterization and analysis employed in this work are adequately described. Most of research work was conducted in the laboratories at the Department of Physics, University of Nairobi, Kenya except for the following: Scanning electron microscopy (SEM) of the films which was carried out at Helmholtz-Zentrum, Institute of Silicon Photovoltaic Berlin, Germany. Atomic Force Microscopy (AFM) and four point probe measurements were done at the Material Science and Engineering, Texas A & M University, College Station, USA and Solid state laboratory, Makerere University, Kampala, Uganda respectively; X-ray diffraction measurements were taken at the University of Botswana, Botswana.

The first section of this chapter, provides details of glass substrates, TiO_2 and TiO_2 + carbon black pastes, dyes, electrolytes and counter electrodes. The glass substrates acquired for Solaronix SA, Switzerland employed for the building of both photo and counter electrodes were 2.2 mm thick and had a $15 \Omega/\text{sq}$ fluorine doped tin oxide coated on one side. In addition, the procedure for the assemblage of the complete DSSC device is also explained. The second section deals with setups of spectroscopic methods such as XRD and SEM, AFM, UV-Vis spectroscopy, electrical measurements of films and cells' current-voltage characterizations. Reagents and solvents used in this research were mainly of analytical grade and supplied by Sigma Aldrich unless stated otherwise. Ruthenium complex dyes, glass substrates, electrolytes, TiO_2 pastes, sealants and gaskets were purchased from Solaronix SA, Switzerland. Carbon black was acquired from Alpha Aesar, Germany. The dye sensitized solar cells assembled to study current-voltage characteristics for porosity, electrolyte redox concentrations, double reflection and dyes had $13.5 \mu\text{m}$ film thickness and cell active area of 0.48 cm^2 while those assembled to study film thickness with respect to photovoltaic performance had $3.21 \mu\text{m}$, $8.23 \mu\text{m}$, $13.52 \mu\text{m}$ and $18.93 \mu\text{m}$ average film thicknesses and cell active area of 0.48 cm^2 .

4.2 Samples preparation

4.2.1 Preparation of mixed TiO₂ and carbon black paste

The materials for the preparation of this paste included TiO₂ paste (Ti-Nanoxide T/SP) comprising anatase particles (15-20 nm), concentration (18 wt %), terpineol and organic binders from Solaronix SA, Switzerland. So also carbon black (100% compressed, acetylene) was acquired from Alfa Aesar, Germany.

A 1.99 g of Ti-Nanoxide T/SP employed as control paste was diluted in 50 ml of absolute ethanol (analytical grade, 98% alcohol) and mixed with a magnetic stirrer bar for 30 minutes. Subsequently, 0.01g of carbon black which represents 0.5 wt% of the desired past was added to the suspension and dispersed with the sonication horn of a digital sonifier (Branson Ultrasonics, China) to break any aggregates in the nanoparticles. It was sonicated in pulses (2s ON, 2s OFF) to avoid temperature elevation for 30 minutes at intervals of 6 minutes and stirred for 5 minutes at each interval. The mixture was then transferred to a rotary evaporator at 80 °C, 100 mbar. The paste was again homogenized by a grinder after the ethanol was evaporated. This procedure was repeated for 1.0, 1.5, 2.0 and 3.0 wt % of carbon black making five mixed pastes of varying carbon black concentrations which were collected in preservation bottles and labelled appropriately.

4.2.2 Thin film preparation

TiO₂ pastes (0, 0.5 1.0, 1.5, 2.0 and 3 wt% of carbon black) were employed to coat films on F:SnO₂ conducting glass substrate by the method of screen printing. The screen printing mesh (63T, Silk screening print services Ltd, USA) had 20 mesh openings of size 6x8 mm that produced a total of 20 similar films at one coating. To coat subsequent layers, the coated film was dried in air for 10 minutes, transferred to a hot plate at 120 °C for five minutes and allowed to cool to room temperature then another coat applied until the desired number of coatings was attained. These films were then annealed in a tube furnace step wise at 500 °C for 30 minutes in air and let to cool to room temperature. The film thicknesses of study was performed by Alpha Step IQ surface profilometer (Tencor Instruments Inc, USA). The prepared films were either used for film thickness measurement, electrical characterisation, XRD, SEM, AFM and UV-Vis analysis or used

for the preparation of photoanode for the assemblage of a complete solar cell for *I-V* characterizations.

4.2.3 Dye preparation

A 0.5 mM ruthenium complex dye solution of prepared by dissolving 0.0297g of cis-diisothiocynato-bis (2,2'-bipyridyl-4,4'-dicarboxylato) ruthenium(II) bis (tetrabutylammonium) (known in literature as N719) complex in 50 ml of 99.9 % ethanol. The dye solution was stirred for 2 hours with a magnetic bar stirrer and dispersed with sonification horn in pulses (2 s ON 2 s OFF) for 2 hours. The above procedure was repeated with 0.0341g of triisothiocynato-(2, 2':6', 6''-terpyridyl-4, 4', 4''-tricarboxylato) ruthenium (II) tris(tetra-butylammonium) complex (known in literature as N749) to produce 0.5 mM solution of dye. The resulting dye solutions were drained into preservation bottles and kept in a cool dark place awaiting electrode dye sensitization.

4.2.4 Dye characterization

In this procedure, the absorption capacity of the dye solution used in this work were determined. These dyes used were N719 and N749 (black dyes). Absorption characteristics were studied using UV-Vis spectrophotometer at wavelengths 300 nm to 950 nm. The absorption characteristics were recorded for 0.5 mM solution of both N719 and N749, and also for photoelectrodes sensitized with each of the dyes. An empty cuvette was used as a reference for investigation on dyes in solution whereas unsensitized TiO₂ thin film was employed as reference for the dye sensitized film. In both situations the respective spectra recorded were the results of the differences between the spectra of the reference and the measured samples.

4.2.5 Preparation of counter-electrode

In the preparation of cathode electrodes, pre-drilled fluorine doped tin oxide conducting glass substrates were cut into the size of 2 cm x 2 cm and cleaned in the ultrasonic bath using ethanol, acetone and water for 20 minutes each in that order. After cleaning, the glass substrates were dried in dry and clean air for 1 hour at room temperature. Platinum (Platisol T/SP acquired from Solaronix SA, Switzerland) was coated on the conducting side of the

glass substrate and heated in a tube furnace for 30 minutes at a temperature of 450 °C. The counter electrodes were then cooled in dry and clean air before use.

4.2.6 Complete solar cell assembly

Figure 4.1 illustrates the assembling of a dye sensitized solar cell. In the first part of this exercise, the photoanode was prepared as follows: TiO₂ coated films sintered in tube furnace were let to cool to 80 °C then dipped in ruthenium dye complexes (N719 or N749) that was at room temperature, for 24 hours. The dye sensitized films were subsequently rinsed in ethanol to eliminate any excess dye and dried on a hot plate for 5 minutes at 70 °C.

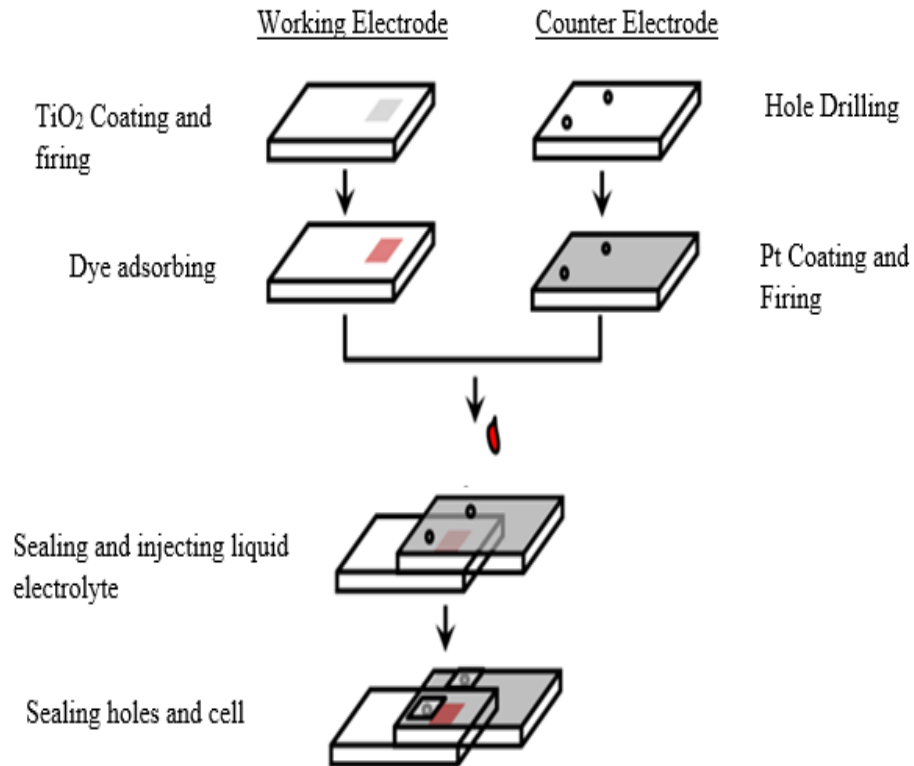


Figure 4.1: Fabrication process of complete DSSC unit cell (Cho *et. al.*, 2013)

It was followed by fusing the photoelectrode together with the counter electrode in sandwich manner using 60 μm thick thermoplastic sealing film made of surlyn (Solaronix, Switzerland) by heating on a hot plate while applying mechanical pressure at a temperature of 100 $^{\circ}\text{C}$. The iodide/tri-iodide electrolyte, that is, iodolyte HI-30 (0.03 mol dm^{-3}), iodolyte Z-100 (0.10 mol dm^{-3}) or iodolyte Z-150 (0.15 mol dm^{-3}) was dropped onto the hole in the counter electrodes and injected into the cells by vacuum backfilling with the aid of a vac'n'fill syringe. The cell was thoroughly wiped to remove excess electrolyte and finally, the holes in the counter electrodes were sealed using Surlyn and a microscope cover glass.

4.3 Thin film characterization

4.3.1 UV-vis spectroscopy

The ultraviolet-visible (UV-Vis) transmittance, reflectance and absorbance spectra of the TiO_2 (with or without carbon black) thin films were studied using Shimadzu UV-Vis-NIR double beam Spectrophotometer (SolidSpec-3700/3700DUV, Japan, Inc.). All the measurements were recorded at the wavelengths range of 300 nm and 900 nm.

In the first instance, transmittance, reflectance and absorbance of samples were determined at varying film thicknesses (3.21, 8.23, 13.52 and 18.93 μm). Subsequently, the film thickness was kept constant at 3.2 μm and these measurements were repeated for samples with 0, 0.5, 1.0, 1.5, 2.0 and 3.0 wt% of carbon black. In each case the empty FTO/glass was used as reference which means that the spectra recorded were the resultant difference between the spectra of the samples and that of the empty FTO/glass.

4.3.2 Scanning Electron Microscopy (SEM)

The morphological characteristics of the films were studied by the HITACHI S-4100 Scanning Electron Microscope (SEM) with cold field emission gun which allows the investigation of structure and morphology of conductor, semiconductor and insulator materials without application of a conducting surface coatings. It was achieved with Gemini column at 5kV electron source. The SEM micrographs were taken using a CCD (charged coupled device) camera interfaced to a computer. Varying micrographs of

samples with different carbon black concentrations (0, 0.5, 1.0, 1.5, 2.0 and 3.0 wt%) were taken at a magnification of X 30000 for top view images.

4.3.3 Atomic force microscopy (AFM)

The surface microstructural features of the films were characterized using Multimode 8-HR Atomic Force Microscopy/Scanning Tunneling Microscopy (AFM/STM) in tapping mode. Films of varying carbon black concentrations (0, 0.5, 1.0, 1.5, 2.0, 3.0 wt%) were subjected to this measurements.

4.3.4 X-ray diffraction (XRD)

X-ray diffraction was obtained by means of Siemens D5000 Diffractometer (Bruker AXS GmbH, Germany) with 0-20 parallel beam geometry. The theta, 2θ range was from 10° to 80° with detector type of scan at a scan speed of $0.6^\circ/\text{min}$ and step size of 0.01° . The stage was set to rotate at 15 rotations per minute. XRD peak references were obtained from International Centre for Diffraction Data, USA.

4.3.5 Electrical measurements of films for studying resistivity and conductivity

The current-voltage characteristics of the films were determined using Jandel RM3-AR 4-Point Probe. The RM3-AR is a combined constant current source and digital voltmeter. It measures resistivity in combination with four point probe equipment. The unit supplies a constant current and displays either the resultant voltage or the sheet resistance of the sample in ohms/square, depending which function has been chosen. In this measurement, we selected the 'High' button which put the unit in high resolution mode. This was the most desirable settings for high accuracy as it enabled voltages between 0 mV to 150 mV to be measured. A keypad was selected to input a desired constant current in 1 mA to the probe and the resultant sheet resistance in ohms/squares of sample was being displayed. The sheet resistance was displayed because ohms/square button was preferably selected. The procedure was repeated for samples with different film thicknesses (3.21, 8.23, 13.52 and 18.93 μm) and so also samples with different carbon black concentrations (0, 0.5, 1.0, 1.5, 2.0 and 3.0 wt%).

4.4 Solar cell characterization

4.4.1 Current-voltage characterization of complete solar cell

Current-voltage (I - V) characteristics were obtained using a set-up which consists of a 500 W xenon lamp, a solar simulator model SS (Science tech, Canada) equipped with a 1.5 AM G filter interphased with a Kethley, 2400 (Keithly Inc, USA) source meter controlled by a computer interface. The measurements were carried out under the intensity of 100 mW cm^{-2} (equivalent to one sun at AM 1.5) at the surface of the solar cell. All the solar cells characterized in this work had an active area of 0.48 cm^2 . A mask was placed on the solar cell sample to ensure that only the solar cell's active area was exposed to illumination. The current-voltage characteristics under these conditions were obtained by applying an external potential bias to the cell and measuring the generated current with a Keithley 2400 digital source meter (Keithley, USA).

The solar cell's working electrode (cathode) and counter electrode (anode) were connected to the negative and positive terminals of the source meter respectively, then to the computer via GPIB interface. The bias was from short circuit to open circuit and was obtained automatically using a LabVIEW software. From the data, an I - V curve was plotted in real time and the parameters V_{oc} , I_{sc} , FF and P_{max} were computed, displayed and saved automatically as a notepad file. I - V characteristics for dye sensitized solar cells at film thicknesses of 3.21, 8.23, 13.52 and 18.93 μm were recorded. I - V characteristics for solar cells sensitized with N719 and N749 were compared using films of thickness 13.5 μm . For porosity dependent I - V characteristics, I - V was recorded for solar cells with films of 0, 0.5, 1.0, 1.5, 2.0 and 3.0 wt% carbon black concentrations. In the case of redox concentration dependent I - V , solar cells with electrolyte concentrations of 0.03, 0.1 and 0.15 mol dm^{-3} were measured. The effect of double illumination on the cell's active was also studied by employing a 6 cm x 6 cm mirror at the back of a Pt counter electrode of the cell.

4.4.2 Electrochemical Impedance Spectroscopy (EIS)

The electrochemical impedance spectroscopy measurement set up is illustrated in figure 4.2. Impedances of DSSC at varying film thickness (3.21, 8.23, 15.52 and 18.93 μm) were determined using AUTOLAB Potentionstat, PGSTAT204 (Metrohm, SA). The

AUTOLAB coupled with an LED was connected to a computer interface with the aid of a GIPB interface. Impedance and frequency were obtained automatically using a software NOVA 1.10.

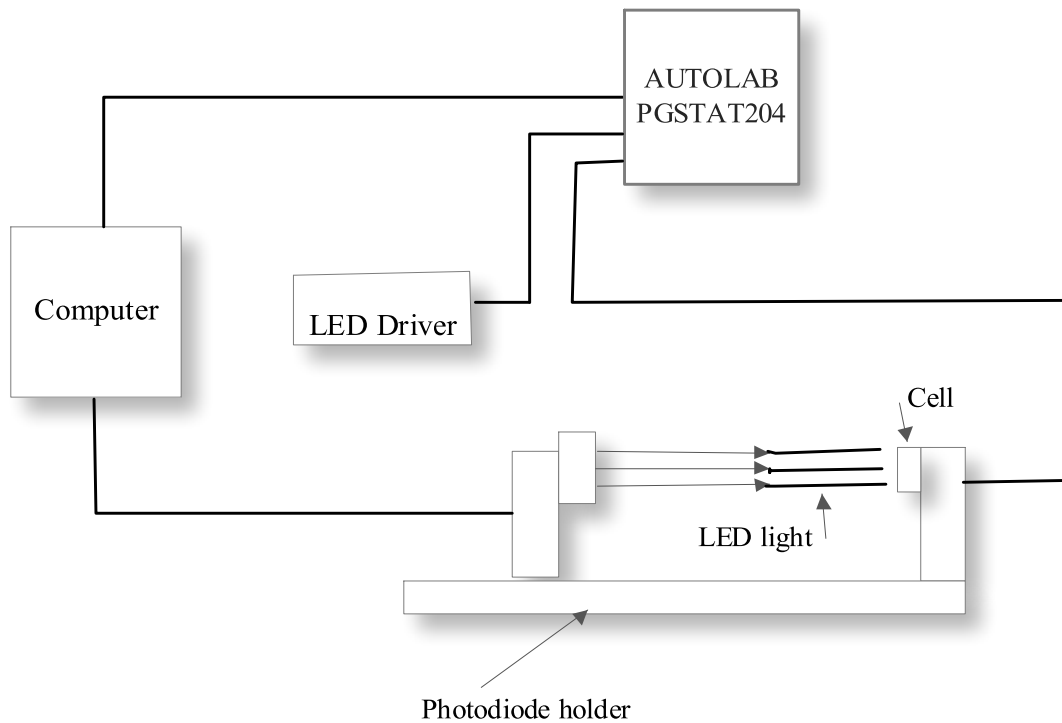


Figure 4.2: Schematic Diagram of Electrochemical Impedance Spectroscopy Set Up

CHAPTER FIVE

RESULTS AND DISCUSSIONS

5.1 Introduction

This chapter deals with the analysis and discussions of the optical (UV-Vis) characteristics of TiO₂ photoelectrodes coated by screen printing method. The electrical characteristics of the films at varying film thickness and pores size were also critically analyzed and discussed. The other part of this chapter is where the XRD characteristics of the thin films are analyzed and discussed. This is followed by analyzing the results from the morphological (SEM and AFM) characteristics of the TiO₂ thin films (with and without carbon black). The last and concluding part of this chapter analyzed and discussed the *I-V* characteristics of the solar cells. Dye sensitized solar cells with varying carbon black concentrations, film thicknesses, electrolyte redox concentrations and ruthenium dyes are analyzed and compared.

5.2 Optical Characterization

5.2.1 Effect of film thickness on the transmittance of TiO₂ films

The transmittance spectra of screen printed TiO₂ thin films at varying film thicknesses is presented in figure 5.1. Samples generally showed high transparency in the visible region, slight decrease in the IR and sharp fall in the UV. Transmittance dropped with increase in film thickness. At 600 nm, the transmission spectra had maximum average values 80%, 74%, 70% and 62% for the films of thicknesses of 3.21, 8.23, 13.52 and 18.93 μm respectively. It could be for the reason that optical film density increases with increase in film thickness. Since there was the densification of films due to rise in thickness, passage of light was compromised thereby resulting to low transparency. In other words, the decrease in transmittance is due to enhanced absorption as result of increase in film thickness and the scattering effect originating from increased crystallite size (Malliga *et. al.*, 2014). The transmittance of TiO₂ thin films coated by spin coating within film thickness of 0.5 and 2.0 μm were also found to depend inversely on film thickness (Kao *et. al.*, 2009). The results also show that the average increase in film thickness of 5.2 μm resulted to a corresponding average decrease of 5.3 % in transmittance. That is to say, on the average, every 5.2 μm rise in thickness blocked 5.3 % transmission of light. The maximum

transmittance values of these samples were obtained at the wavelength of about 400nm and absorption edge was found to be 300 nm.

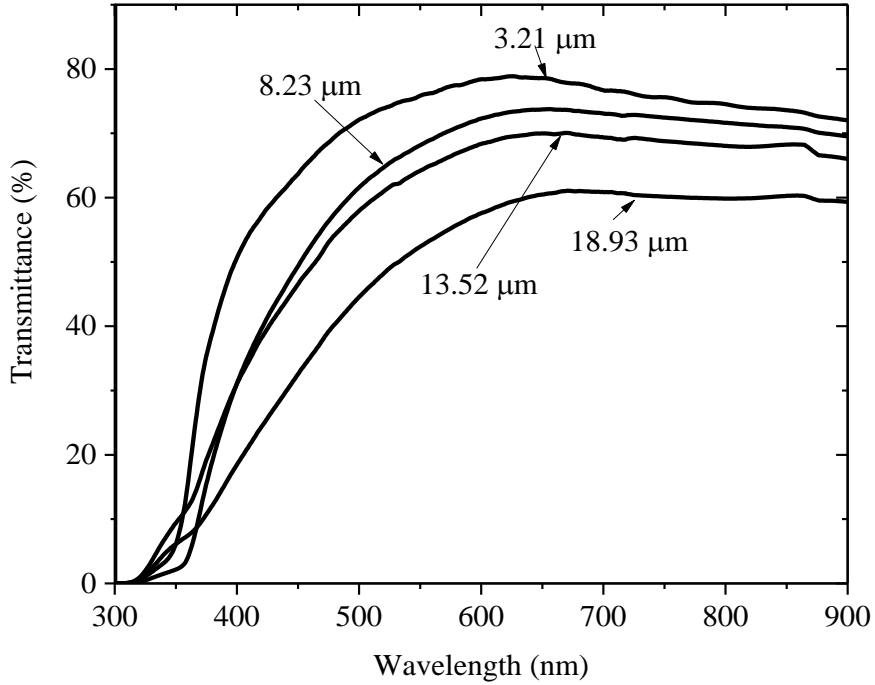


Figure 5.1: UV-Vis transmittance versus wavelength spectra for screen printed TiO₂ thin films at film thicknesses of 3.21, 8.23, 13.52 and 18.93 μm from 300-900 nm.

Figure 5.2 shows how transmittance varied with film thickness varied at specific wavelengths of 600 and 850 nm. The selected wavelengths, 600 nm and 850 nm are in the visible and infrared respectively. It was observed that there was a drastic drop in transmittance at 600 nm as film thickness increased. This was however different in the near infra-red region of 850 nm as the drop was gentle and slow. More importantly, the transmittance values at 850 nm are lower compared to values at 600 nm. This may be attributed to the reason that the energy of photons at 850 nm were lower therefore penetration through the films become low. The films showed higher transparency in the visible compared to IR and UV. As observed in the figure 5.2, the transmittance for 3.21, 8.23, 13.52 and 18.93 μm at 600 nm were found to be 78, 73, 68 and 57 % respectively. On the other hand, 3.21, 8.23, 15.52 and 18.93 had values of 73, 71, 68, and 60 % respectively at 850 nm. It can therefore be stated that in all the thicknesses apart from 18.93

μm , there was reduction in transmittance as wavelength increased from 600 nm to 850 nm. However, there was a 3 % rise in transmittance for the 18.93 μm film as wavelength increased from 600 nm to 850 nm. This can be considered to be within the allowed marginal error implying that there was no rise in transmittance. This is no doubt a characteristic property of films for application in DSSC.

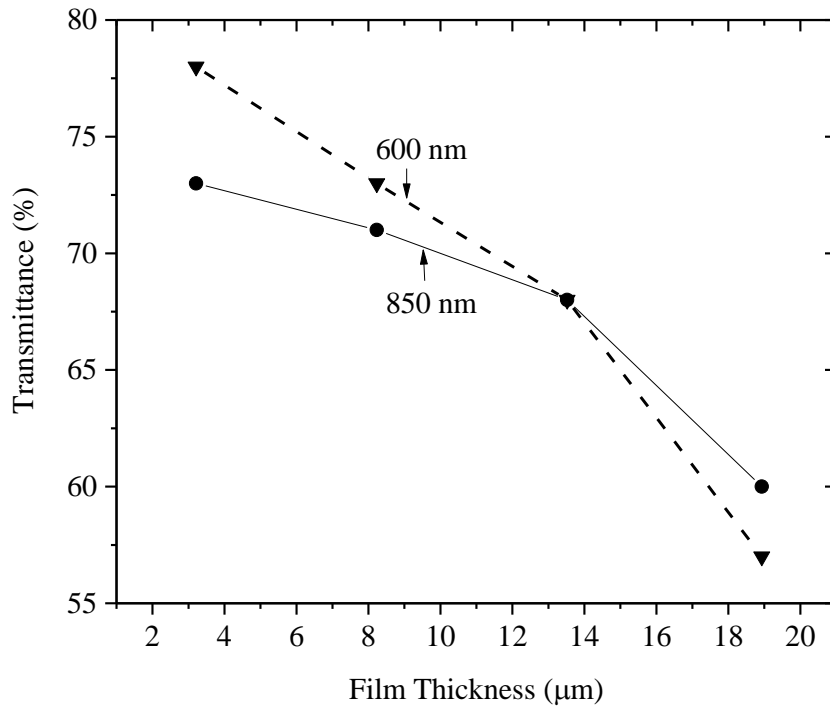


Figure 5.2: Variation of transmittance spectra with film thickness at wavelengths of 600 and 850 nm

5.2.2 Effect of porosity on the transmittance of TiO_2 thin films

The transmittance spectra of screen printed TiO_2 thin films at varying carbon black concentrations are shown in figure 5.3. For this particular study, film thickness of 3.2 μm was used to eliminate the effect of film thickness on the observations. UV-Vis transmittance of the films were determined at the wavelengths range of 300 and 900 nm. From the results, samples 0, 0.5 and 1.5 wt % showed high transparency in the visible region and decreased sharply at the UV region but dropped slowly towards the IR. The spectra have an average maximum value of 79% (0 wt %) in the visible. It was observed that as the weight percentage of carbon black increased, the light transmission decreased.

The film with the maximum weight percentage of carbon black (3 wt %) was the least transparent (39%). Carbon black increased the porosity of the films which in turn increased reflectance and absorbance of the films therefore, transmittance is reduced with increase porosity.

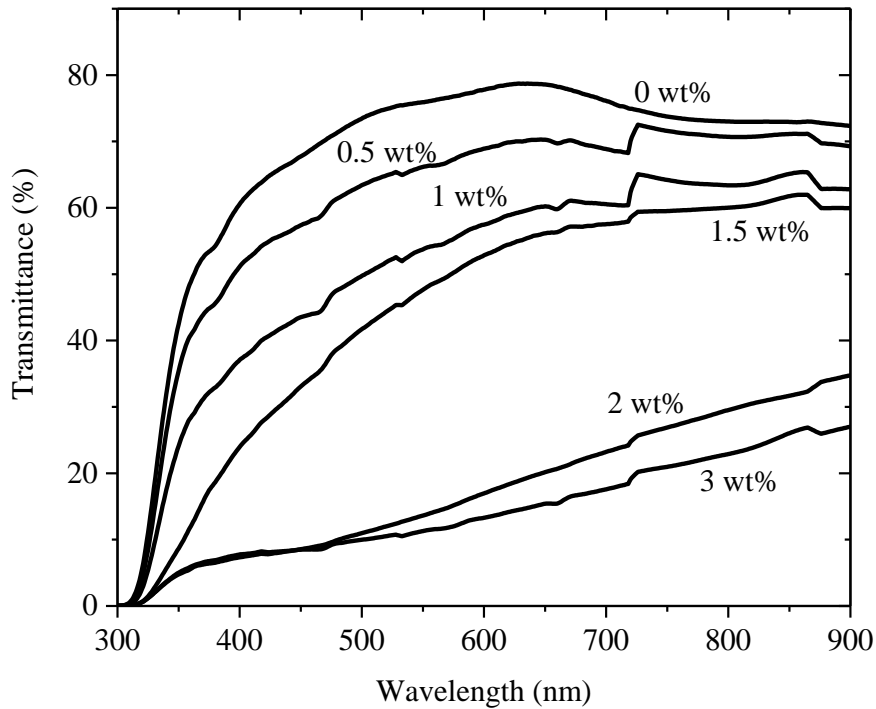


Figure 5.3: UV-Vis transmittance versus wavelength spectra of screen printed TiO₂ thin films (3.21 μm) at varying carbon black concentrations (i.e. 0, 0.5, 1.0, 1.5, 2.0 and 3.0 wt %) from 300-900 nm.

Figure 5.4 shows the variation of transmittance spectra with carbon black concentrations at the wavelengths of 600 and 850 nm. The decline in transmittance with porosity at 600 nm was found to be sharp but slow at 850 nm. However at higher porosity, the decline in transmittance of the films were slow and steady at both 600 and 850 nm. It could be because the porosity of films was very high that could allow for easy passage of photons regardless of the energy they possessed. Transmittance values of films as measured at 600 nm were found to be 78, 69, 57, 52, 16 and 13 % for 0, 0.5, 1.0, 1.5, 2.0 and 3.0 wt% respectively. At 850 nm in the IR, transmittance values for 0, 0.5, 1.0, 1.5, 2.0 and 3.0 wt% were recorded

as 73, 71, 64, 61, 31 and 26 % respectively. This shows higher transmittance in the visible especially for films of lower porosity.

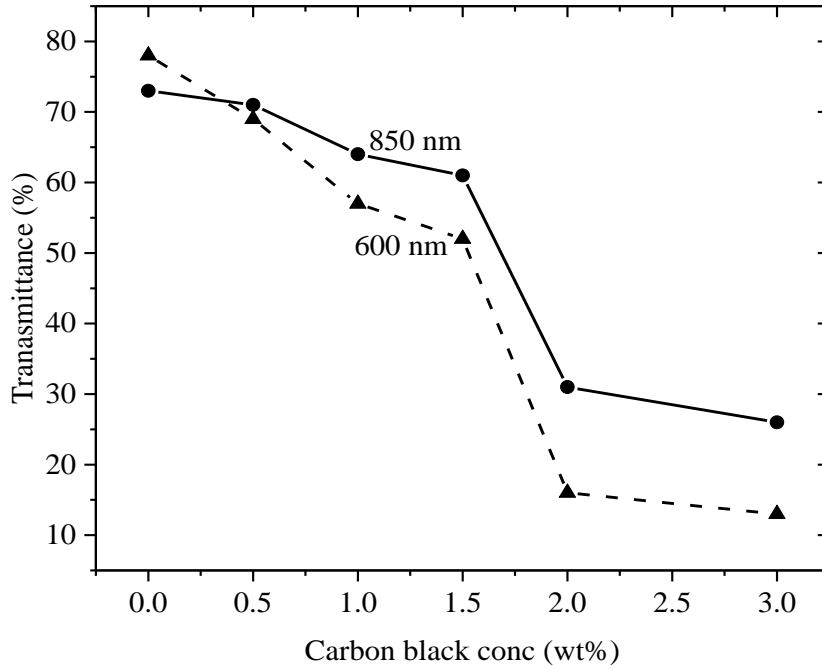


Figure 5.4: Variation of transmittance with carbon black concentrations at wavelengths of 600 and 850 nm for TiO₂ thin films (3.21 μ m)

Furthermore, transmittance spectra of samples 2 wt % and 3wt % were relatively lower. Though the rise in porosity of films also contributed to the drop in their transmittances, the drastic drop could be due to residue of carbon black left behind because at those concentrations, 500 °C temperatures is not sufficient to completely burn out carbon black hence the light blockage. The obvious dark pigment seen in SEM micrographs (figures 5.21 (e) and (f) on page 89, confirms this observation.

5.2.3 Effect of film thickness on the reflectance of TiO₂ thin films

The dependence of UV-Vis reflectance spectra on the thickness of TiO₂ thin films is presented in figure 5.5.

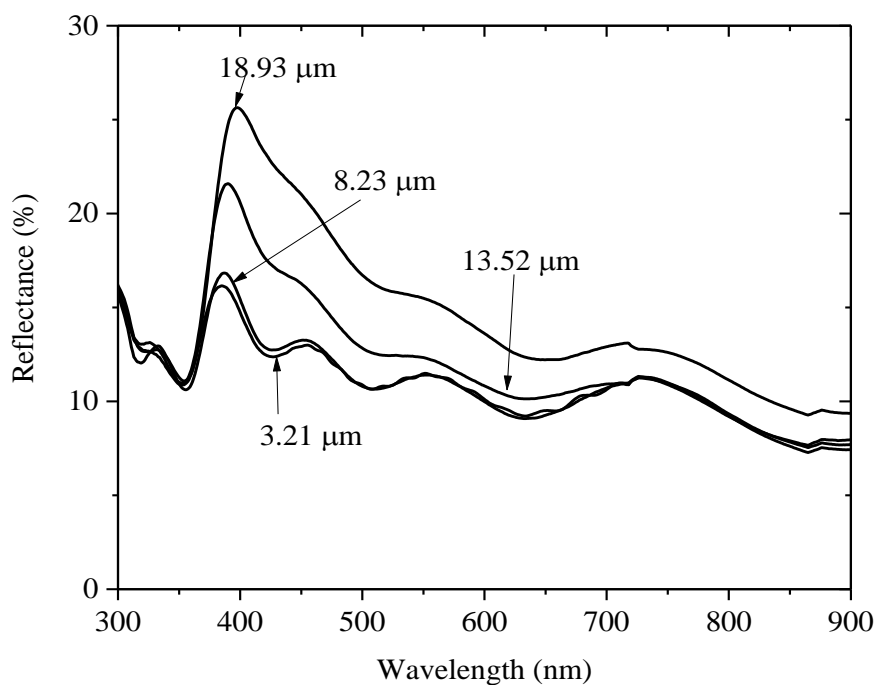


Figure 5.5: UV-Vis reflectance versus wavelength spectra of bare TiO₂ thin films for various thicknesses

The films were observed to be relatively reflective. However, the reflectance was observed to rise with increase in film thickness in the visible though it remained invariant in the UV and IR. It is expected that reflectance is not affected by film thickness. However, in this case, reflectance was observed to increase with film thickness. The explanation is that unlike in plane reflection where it is a surface activity, in this case reflectance takes place across the entire cross-sectional area of the film, otherwise known as volume reflection. The increase in reflectance with film thickness could be attributed to increase in roughness. As previously reported (Kangarlou & Rafizadeh, 2012), surface roughness increases with the rise in film thickness. In their investigation where TiO₂ films were deposited at varying thickness between 50 and 100 nm, it was found that surface roughness significantly increased with thickness due to bulk diffusion and coalescence. Generally, light is reflected back into TiO₂ thin films as it irradiates into the photoelectrode. If the photoelectrode has a strong scattering ability, much more light is reflected back. The increased surface

roughness in this case could be responsible for the enhanced scattering ability and hence higher reflection.

The variation of reflectance with film thickness at wavelengths of 400 and 800 nm is presented in figure 5.6.

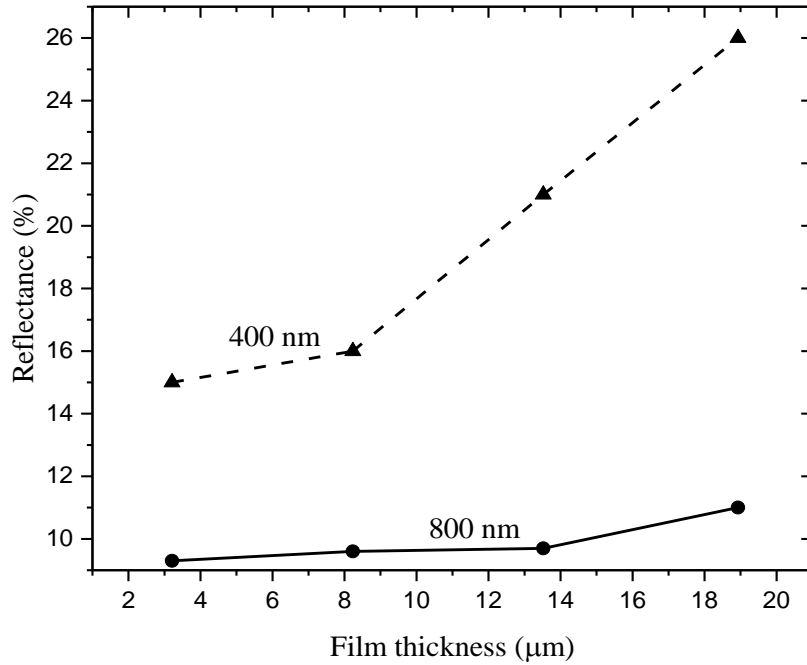


Figure 5.6: Variation of reflectance with film thickness at the wavelengths of 400 and 800 nm.

It was observed that the reflectance spectra rose to their maximum values at 400 nm and dropped rapidly at 800 nm. The films of thicknesses 3.21 μm 8.23 μm, 13.52 μm and 18.93 μm had reflectance values of 15 %, 16 %, 21 % and 26 %, respectively at 400 nm and 9, 9, 9 and 11% at 800 nm, respectively. Reflectance was higher in the visible than in the IR. The explanation is that photons are reflected into the films thereby raising the absorption of more photons.

5.2.4 Effect of porosity on UV-vis reflectance of TiO₂ thin films

The reflectance spectra of TiO₂ films at different carbon black concentrations is presented in figure 5.7.

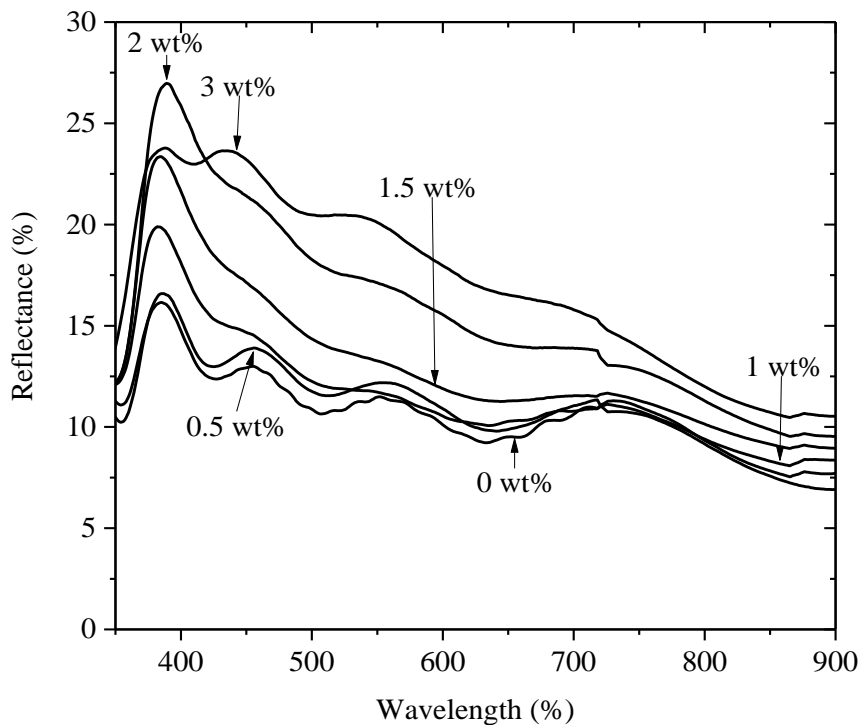


Figure 5.7: Variations of reflectance with wavelength spectra for TiO₂ thin films (3.21 μm) with varying wt % carbon black concentrations (0, 0.5, 1.0, 1.5, 2.0 and 3.0 wt %).

The carbon weighted films possessed relatively high reflectance spectra compared to bare TiO₂ thin film (0 wt %). There was an observed overall rise in reflectance with increase in carbon black concentration. However, the rise was more pronounced at lower wavelengths than in the IR. The rise in reflectance is a result of multiple lights scattering by the artificial pores created. The results show that the bare films exhibited a comparatively smaller porosity than that of carbon black TiO₂ films and that carbon black TiO₂ films enhanced the light reflection capacity of the photoelectrode TiO₂ thin films. The increased reflectance due to higher porosity has also been reported in TiO₂ films with acetylene black (Cho *et. al.*, 2013). The variation of reflectance with carbon black concentrations at the wavelengths of 400 and 800 nm is displayed in figure 5.8.

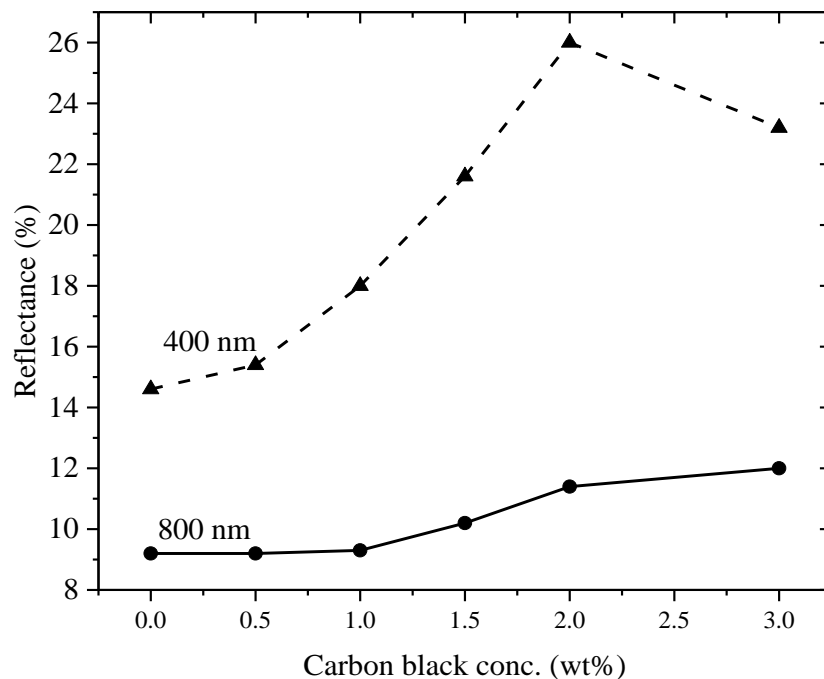


Figure 5.8: Variation of the reflectance with wt % of carbon black concentrations for TiO₂ thin films (3.21 μm) with carbon black concentrations at wavelengths of 400 and 800 nm.

The results show a sharp contrast of reflectance values at 400 and 800 nm. There is higher reflectance at 400 nm than at 800 nm. Films with carbon concentrations of 0, 0.5, 1.0, 1.5, 2.0 and 3.0 wt% had values of approximately 15, 16, 18, 22, 26 and 23 % respectively at 400 nm and 9, 9, 9, 10, 11 and 12 % respectively at 800 nm. There was an abnormal drop in reflectance for 3 wt% in the visible which could be due to impurity in the paste in the course of coating. This explains the peak at 2 % for reflectance at 400 nm (figure 5.8)

5.2.5 Effect of film thickness on the UV-vis absorbance of TiO₂ thin films

Figure 5.9 shows the absorbance spectra versus wavelength of bare TiO₂ thin films at varying film thickness.

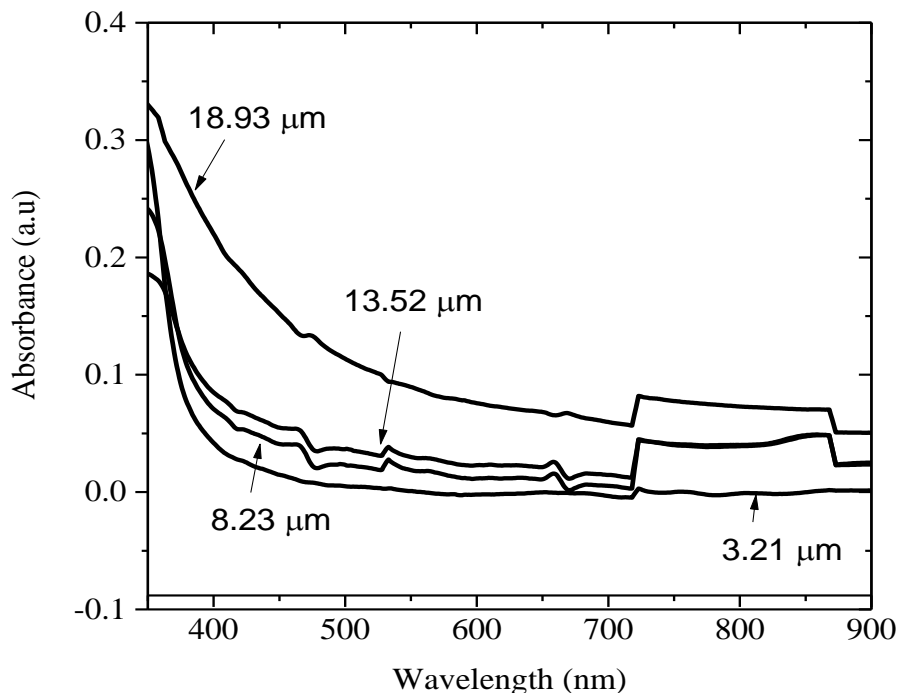


Figure 5.9: Absorbance versus wavelength spectra of bare TiO₂ thin films at different film thicknesses.

The spectra show an increasing absorbance with increasing film thickness in the visible. This trend is due to change in film density and light trapping. The thickest of the films (18.93 μm) was found to have the most absorbance. Other studies have established that the TiO₂ film thickness should be about 10 μm for the optimal light-absorbing ability (Zhang *et. al.*, 2014; Huang *et. al.*, 2006). The enhancement of visible light absorption means the increase in the light- harvesting capability of the electrodes. This finding is in agreement with the that earlier reported by Zhang’s group that absorbance directly depends on film thickness (Zhang *et. al.*, 2014).

In figure 5.10, the absorbance versus wavelength spectra of N719 dye sensitized TiO₂ thin films at varying film thicknesses from 350 to 900 nm is presented. It was observed that all firms had relatively high absorbance compared to bare TiO₂ films. In addition, the absorbance of the films became higher as the films got thicker. It is for this reason that thicker TiO₂ films enhance higher adsorption of N719 through the TiO₂/N719 layers (Kao

et. al., 2009). The surface area of films increases with rise in film thickness, and the larger the surface area, the more the anchoring sites for the N719 dye molecules. Therefore, the more the N719 molecules are adsorbed, the more photons of light are absorbed.

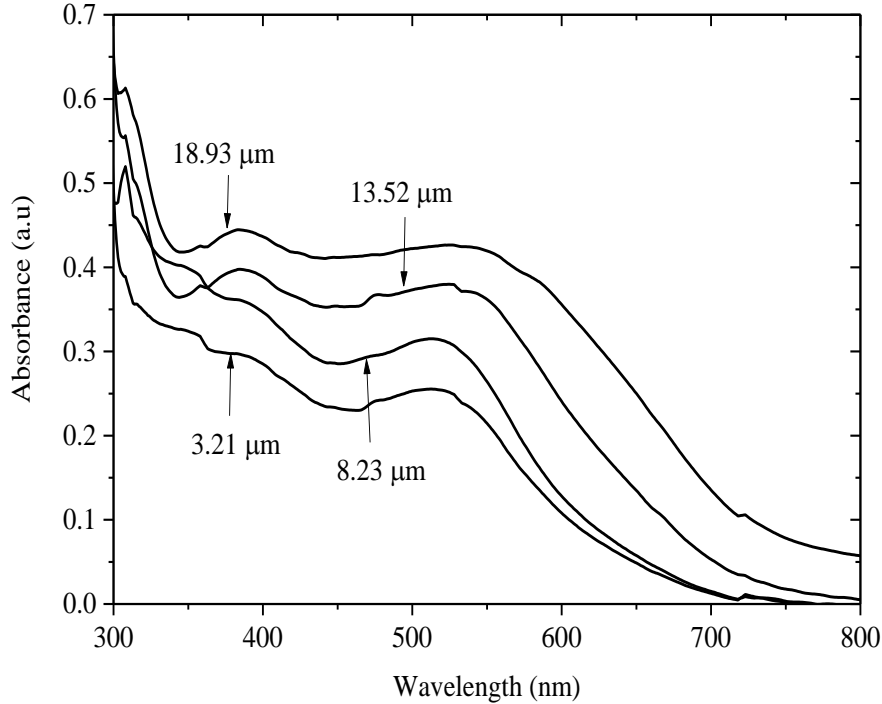


Figure 5.10: Absorbance versus wavelength spectra for N719 dye sensitized TiO₂ thin films at varying film thickness.

The variation of absorbance with wavelength for dye sensitized TiO₂ thin films at thicknesses of 400 and 800 nm is presented in figure 5.11. The results show higher absorbance in the visible (400 nm) than in the IR (800 nm). Films of thicknesses 3.21, 8.23, 13.52 and 18.93 μm had absorbance values of 0.28, 0.36, 0.39 and 0.44, respectively at 400 nm while the same films had 0, 0, 0.01 and 0.06, respectively at 800 nm. It was observed that there was almost no absorbance at 800 nm whereas significant absorbance was observed in the visible.

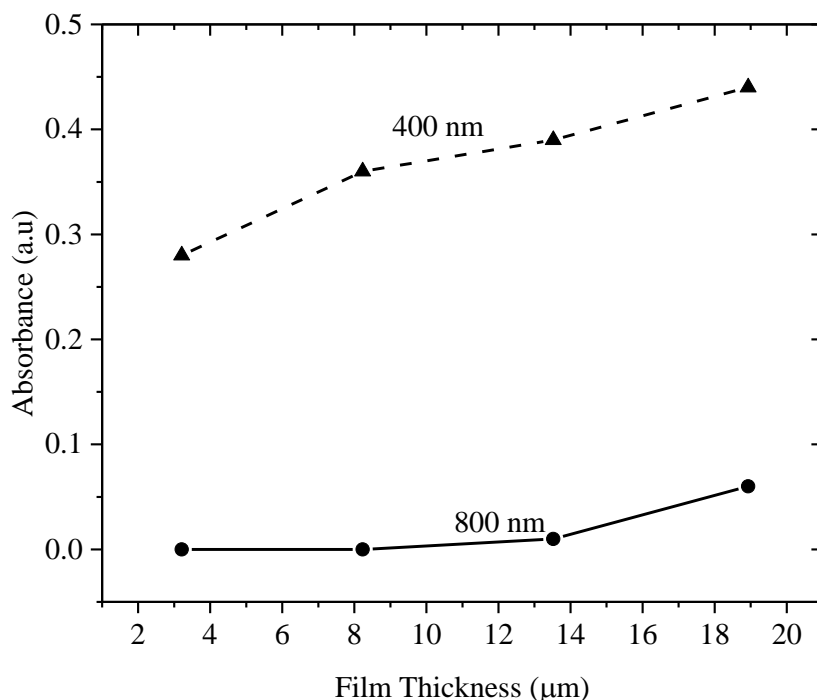


Figure 5.11: Variation of absorbance with film thickness for N719 dye sensitized TiO₂ films at 400 and 800 nm

5.2.6 Effect of porosity on the UV-vis absorbance of TiO₂ thin films

The absorption spectra of TiO₂ thin films at varying carbon black concentrations is presented in figure 5.12. At both 400 and 800 nm, absorption increased with film thickness and the films absorbed more at 400 nm. The step wise drops observed at 720 nm is a result of the change in detectors of the spectrophotometer. Though the absorbance spectra were generally low, it can be observed that bare TiO₂ thin film had the least absorbance. The absorbance of the films increased with increase in wt % carbon black (that is porosity). As the pores increased, absorbance increased due to increase in optical path length, optical light confinement, or light trapping (Cho *et. al.*, 2013). On a general note, light is reflected through TiO₂ films when it irradiates into the photo-electrode. If the photo-electrode possesses strong scattering capacity, a lot more of light intensity is reflected back to the inner TiO₂ photo-electrode, which improves the quantity of light absorbed by the films. These observations are in agreement with previous investigations (Cho *et. al.*, 2013; Pham *et. al.*, 2012) where pores were created for enhancing light absorbance in TiO₂ thin films.

It was found that the absorbance 0 wt% film rose abnormally above all other spectra in the UV. This was not expected from bare TiO₂ films therefore it could be the presence of some impurities in the course of processing the films.

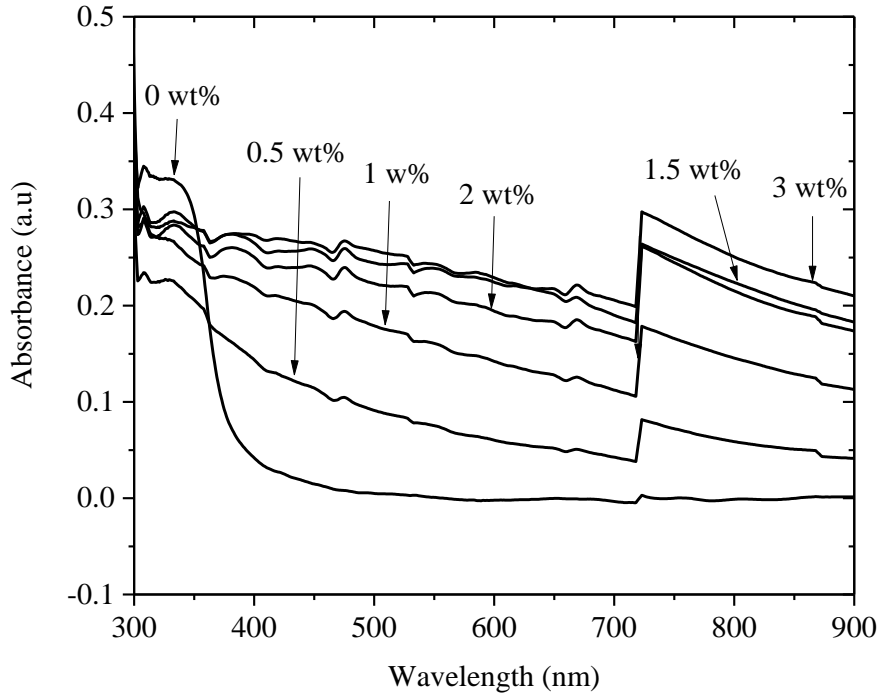


Figure 5.12: Absorbance versus wavelength spectra for TiO₂ thin films (3.21 μm) at varying carbon black concentrations.

5.2.7 Effect of dye-sensitization on the UV-vis absorbance of TiO₂ thin films

The absorbance of bare TiO₂, N719 sensitized and N749 sensitized 13.5 μm TiO₂ thin films is presented in figure 5.13. An absorption edge of 300 nm was recorded showing the highest absorbance values in all the films. It was found that TiO₂ had a relatively low absorbance. N719 dye showed high absorbance between 300 and 700 nm but dropped beyond this range to the same value exhibited by TiO₂. In the case of N749, the high absorbance value extended up to 850 nm showing N749 absorbs photons within the UV, visible and IR whereas N719 absorbs photons only within UV and the visible. This is to say the black dye absorbs photons within a wider range of wavelengths compared to N719. However, N719 has a higher absorbance value between 300 and 600 nm then dropped below N749 between 600 and 850 nm. The behavior reveals that N719 is a better absorber in the visible which

is ideal for PV applications. Though N749 is wider range absorber, its absorbing ability in the visible is not as good as N719 therefore making it inferior to N719 in the area of DSSC. It was also observed that between 850 and 900 nm, all the films had the same absorbance.

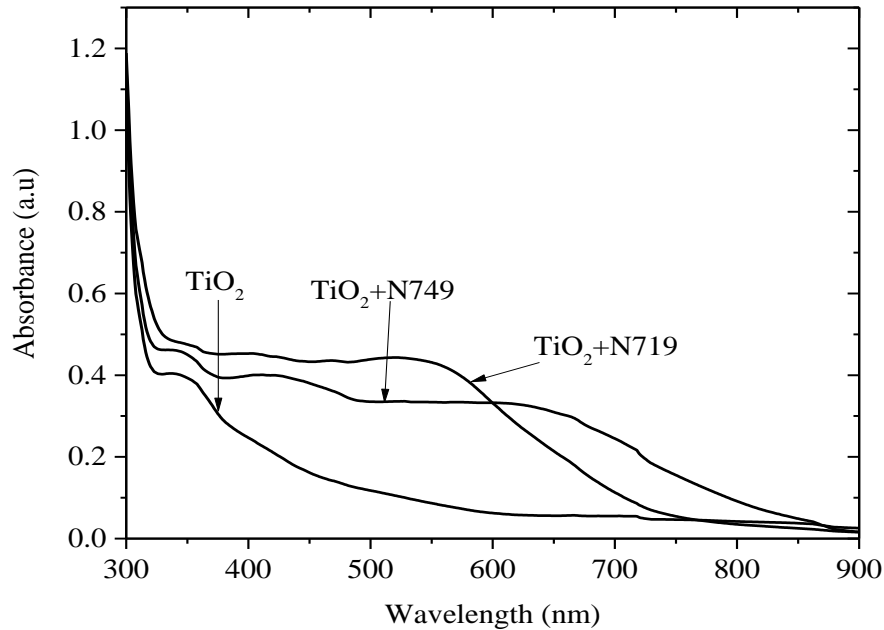


Figure 5.13: Absorbance versus wavelength spectra of bare TiO_2 , N719 sensitized and N749 sensitized TiO_2 thin films ($13.5 \mu\text{m}$)

5.2.8 Effect of film thickness on the refractive index of TiO_2 thin films

The refractive index of TiO_2 thin films at different film thickness is presented in figure 5.14. In this study, optimum film of thickness, $13.5 \mu\text{m}$ was maintained. The results show films of generally high refractive index within the visible. The values of refractive index decreased with the rise in wavelengths. These values show that the thin films are absorbing in the studied region. This trend is similar to observations already reported in the literatures (Yakuphanoglu *et. al.*, 2004; Aksay & Altiocka, 2007). From the figure, refractive index increased with increase in film thickness. Films with thickness 3.21 , 8.23 , 13.52 and $18.93 \mu\text{m}$ had refractive indices of 1.38 , 1.41 , 1.55 and 1.69 respectively at the wavelength of 380 nm .

The increase in the refractive indices is partially attributed to the structural inhomogeneity of TiO_2 film. The deposited TiO_2 thin film can be seen as a composite layer consisting of

air and TiO₂ granule and the volume ratio of air in the composite layer decreases with increase in film thickness (Xu *et. al.*, 2013). Therefore the thicker layer, the more compact and dense, resulting in the increase in refractive index of the thin film. From Snell's law, refractive index is the ratio of the sine of the angle incidence to the sine of the angle of refraction and denser materials have higher refractive for their smaller angle of refraction.

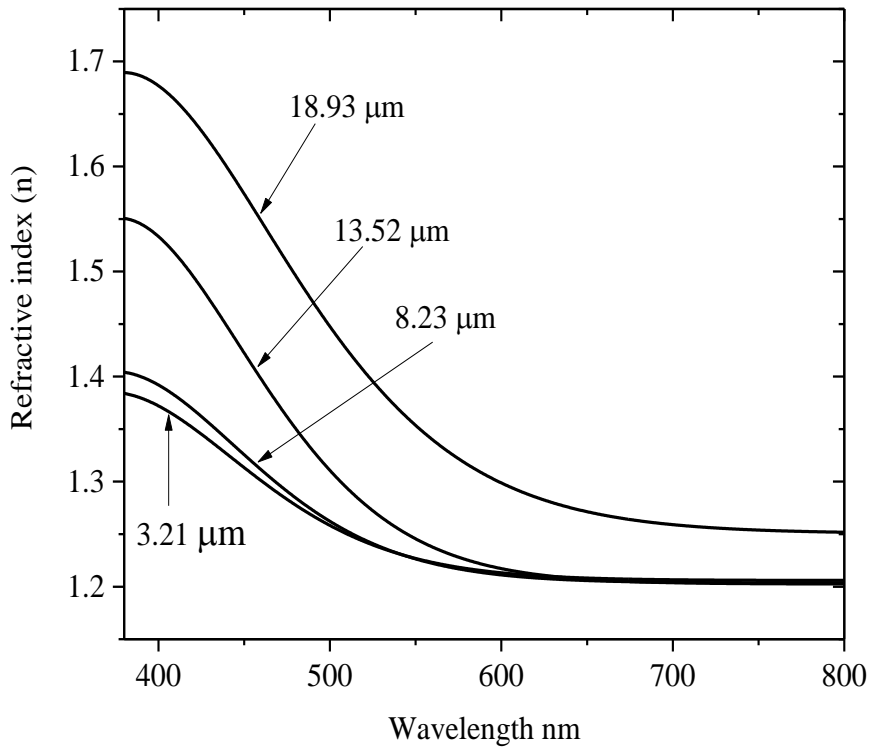


Figure 5.14: Refractive index versus wavelength for TiO₂ thin films at different thicknesses obtained from MATLAB model.

The dependence of refractive index with film thickness at wavelengths of 400, 500, 600, 700 and 800 nm is shown in table 5.1. The results show that at 400 and 500 nm, the refractive index were generally high and increased as the films got thicker. However, at 600, 700 and 800 nm, there was a drastic drop in their values and they remained unchanged even as films became thicker except for 18.93 μm. This could be attributable to the lower energy at longer wavelengths. Since the radiation at this wavelength has got very low energy the deviation of the rays became small despite the increased film thickness. The high refractive index of the films in the visible (400 and 500 nm) shows that they are good for DSSC applications.

Table 5.1: Dependence of refractive index on film thickness at wavelengths of 400, 500, 600, 700 and 800 nm

Film thickness (μm)	Refractive index, (n)				
	400 nm	500 nm	600 nm	700 nm	800 nm
3.21	1.37	1.25	1.21	1.20	1.20
8.23	1.39	1.26	1.21	1.20	1.20
13.52	1.53	1.31	1.22	1.20	1.20
18.93	1.68	1.45	1.30	1.26	1.25

5.2.9 Effect of porosity on the refractive index of TiO₂ thin films

The refractive index of TiO₂ thin films at varying wt % carbon black at the wavelength of 350 and 800 is presented in figure 5.15. It can be seen that the films exhibited high refractive index especially at lower wavelengths and decreased with increasing wavelength. This trend has been reported in previous work (Yakuphanoglu *et. al.*, 2004; Aksay & Altiokka, 2007) thereby validating these observations. The results show that refractive index increased with increase in porosity. That is, 0, 0.5, 1.0, 1.5, 2.0 and 3.0 wt % TiO₂ films had 1.38, 1.50, 1.58, 1.60, 1.70 and 1.62, respectively at the wavelength of 380 nm. Since the films thickness was kept constant at 3.21 μm , the only variable in this case which was the porosity was responsible for the variation observed in the refractive index of the films. This is because the increase in porosity increases light scattering, delay in light path and light trapping (Cho *et. al.*, 2013). This has an overall increase in the light absorption of the films.

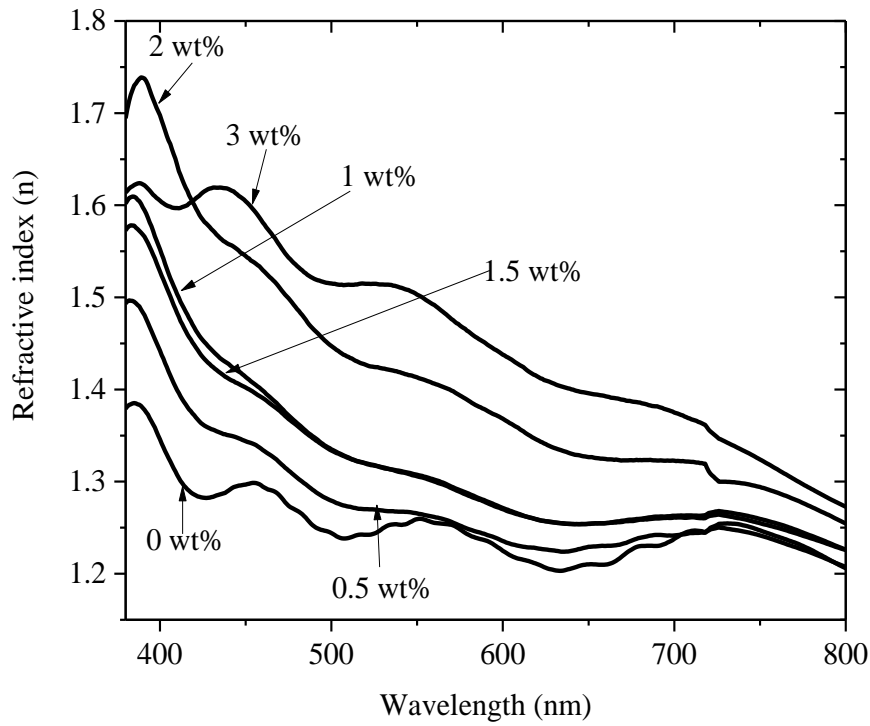


Figure 5.15: Refractive index versus wavelength for TiO₂ thin films at varying carbon black concentrations obtained from a MATLAB model.

The refractive index of TiO₂ thin films of different carbon black concentrations at specified wavelengths is presented in table 5.2.

Table 5.2: Refractive index versus wavelength for TiO₂ thin films (3.21 μm) of different carbon black concentrations at 400, 500, 600, 700 and 800 nm.

Carbon black (wt %)	Refractive index, (n)				
	400 nm	500 nm	600 nm	700 nm	800 nm
0.0	1.35	1.24	1.22	1.24	1.21
0.5	1.44	1.28	1.24	1.24	1.21
1.0	1.53	1.33	1.27	1.26	1.23
1.5	1.55	1.33	1.27	1.26	1.23
2.0	1.70	1.44	1.37	1.32	1.25
3.0	1.60	1.52	1.44	1.38	1.27

The results show higher refractive index in UV and visible than in the IR. In visible and UV, refractive index increased sharply and steadily with the rise in carbon black concentrations. However, refractive index remained invariable with increase in carbon black concentrations in the IR. Higher refractive index results to higher absorbance as a consequence reduced light transmission. In view of this, the higher refractive index observed in the visible due to rise in porosity is an indication of improved films for DSSC applications.

5.2.10 Effect of film thickness on the estimated optical band gap of TiO₂ thin films

The dependence of optical band gap on the thickness of TiO₂ thin films is presented in figure 5.16.

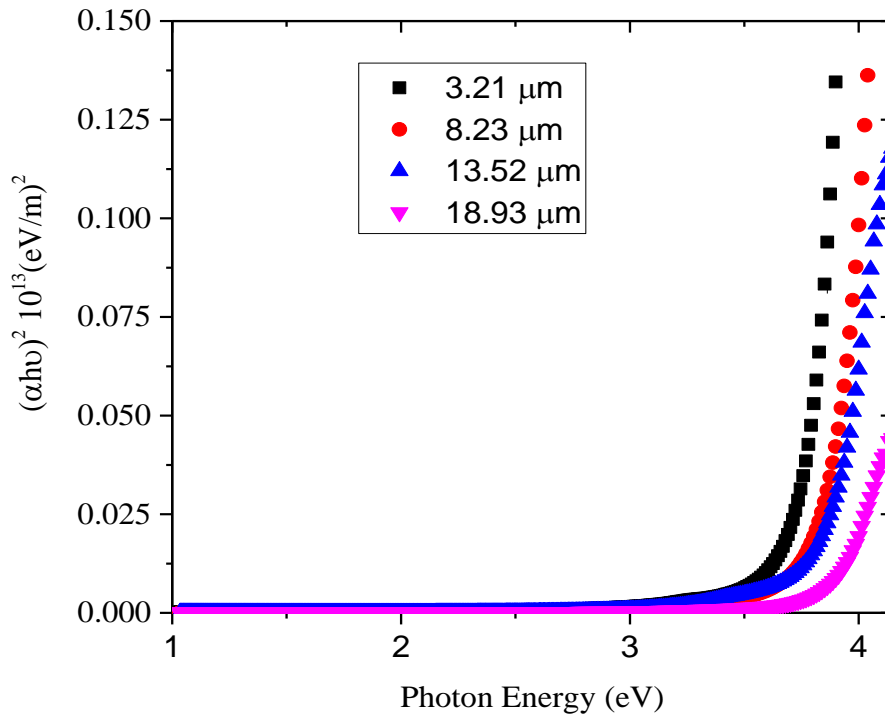


Figure 5.16: Variation of Estimated optical band gap with TiO₂ film thickness

The results show that the estimated optical band gap of films rose as the films became thicker. The increase of TiO₂ optical band gap which might be the result of the change in film density and increasing crystal size could be attributed to the quantum confinement

limit of nanoparticles. It is observed that films of thicknesses 3.21, 8.23, 13.52 and 18.93 μm had estimated optical band gaps of 3.49, 3.59, 3.70 and 3.81 eV respectively as presented in table 5.3.

Table 5.3: Variation of estimated optical band gap of TiO₂ with film thickness

Film Thickness (μm)	Estimated Optical Band Gap (eV)
3.21	3.49
8.23	3.59
13.52	3.70
18.93	3.81

Though band gap is an intrinsic property of a material which ordinarily should not be affected by film thickness, the estimated optical band gap has been reported by several research groups to depend on film thickness. In the estimation of the optical band gap of films, absorption coefficient and film thickness are mutually dependent (Kittel, 1996). In the light of the foregoing, the estimated band gap of a thin film cannot remain unchanged with variation in any of them. The behavior observed in this study is similar to observations by Granqvist and group on TiO₂ films studied by combined reflectance, transmittance spectra, and Forouhi-Bloomer (FB) method (Rodriguez *et. al.*, 2000). A similar trend was observed with optical band gap of ZnO thin films (Miao *et. al.*, 2007). More to that, investigations on annealing temperature dependence of TiO₂ thin films on band gap also revealed that optical band gap increases as the films become thicker (Aksay & Altıokka, 2007). In their study, film thickness was found to increase as the annealing temperature decreases. Contrary to this finding, another group had earlier reported the optical gap of TiO₂ films to decrease as the films become thicker (Malliga *et. al.*, 2014). However the thickness of their samples was less than 2 microns whereas in the present studies, thickness ranges between 3.21 and 18.93 μm . This difference might likely be responsible for these opposite observations. In table 5.4, the estimated optical band gaps of TiO₂ was found to range from 3.49 to 3.81 eV. The values are high in comparison to the known theoretical band gap of 3.2 eV due to high film thickness. However, Malliga and group have also

reported the estimated band gap of TiO_2 to be between 3.50 and 3.92. On a positive note, films with higher band gaps for DSSC applications reduce recombination.

5.2.11 Effect of porosity on the optical band gap of TiO_2 thin films

Figure 5.17 shows the optical band gaps of TiO_2 thin films with different porosity.

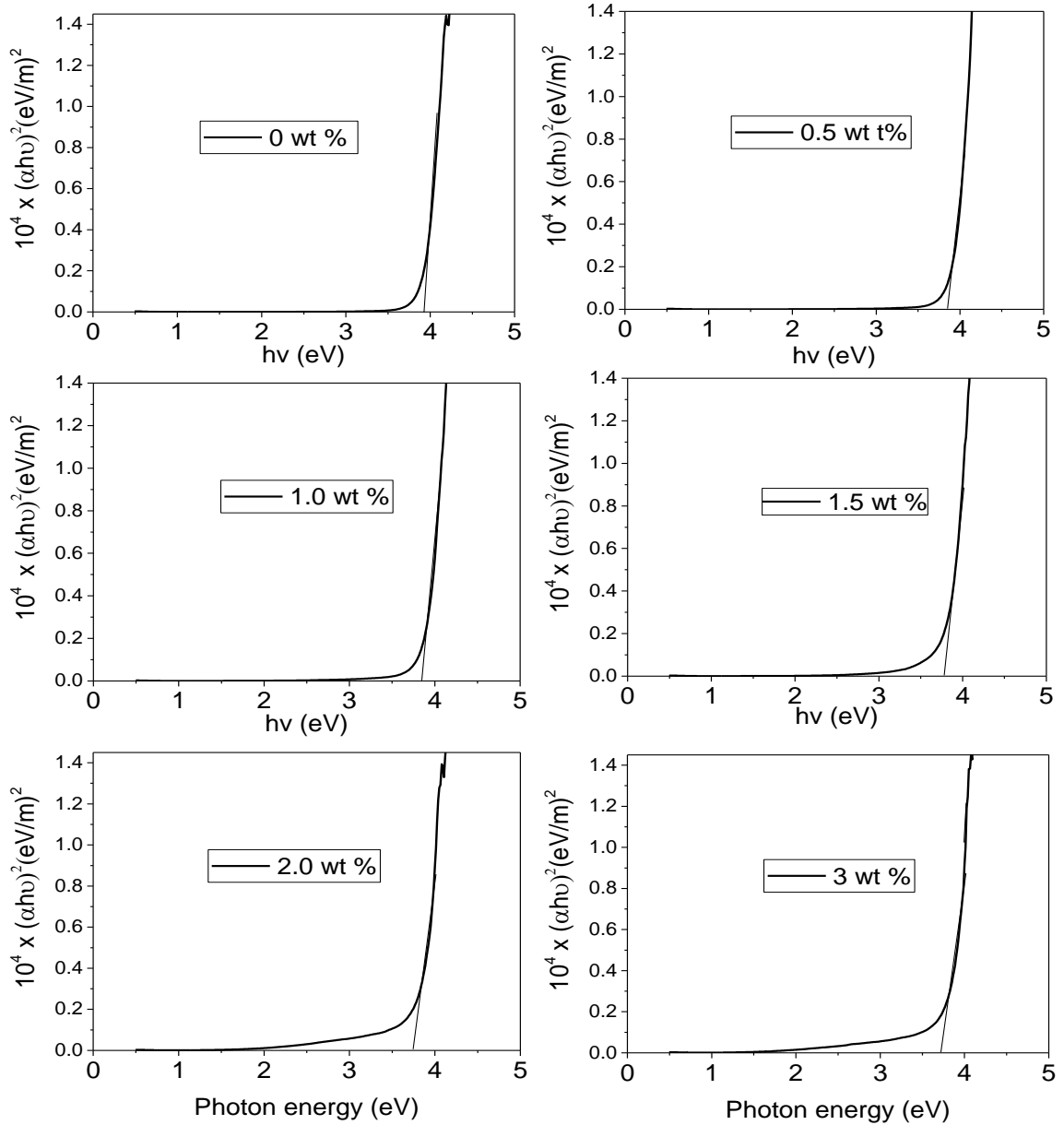


Figure 5.17: Estimated optical band gaps of TiO_2 thin films at varying wt % carbon black

The optical band gaps were obtained using the same procedure as discussed in sub-section 5.2.10. As seen in figure 5.17, there was no significant change in the band gaps of samples as the porosity increased. It was found that porosity had no effect on band gaps as all the films despite their variations in porosity had a band gap of approximately 3.8 eV.

5.3 Electrical Characterization

5.3.1 Effect of thickness on resistivity and conductivity of TiO₂ thin film

The resistivity and conductivity of TiO₂ thin films at different film thicknesses are presented in table 5.4.

Table 5.4: Resistivity and conductivity dependence on film thickness of TiO₂ thin films

Film Thickness (μm)	Resistivity ($10^{-2} \Omega\text{cm}$)	Conductivity (Siemen's cm^{-1})
3.21	3.39	29.4
8.23	6.18	16.1
13.52	13.53	7.3
18.93	22.63	4.4

The results in table 5.4 show that resistivity increased as the film thickness increased. This could be due to increase in collisions among electrons as they become more in number. The amount of electrons in a thin film is sometime influenced by the potential applied across the film or the quantity of the material deposited in a particular area. However, in this experiment, the potential was kept constant therefore, increase in thickness could be responsible for the rise in the number of electrons. The thicker the films, the more the electrons and hence the more the collisions which could result to increased resistivity. In addition, thicker films are likely to create longer transmission paths for electrons which could also result to more collisions.

The relationship between resistivity and conductivity is given by equation (5.6)

$$\sigma = \frac{1}{\rho} \tag{5.1}$$

The values for conductivity are equally recorded in table 5.4. It can be seen that conductivity of TiO₂ thin films is the reciprocal of resistivity. Therefore, conductivity decreased as the film thickness rose. The values obtained for both conductivity and resistivity are plotted in figure 5.18 to give a better understanding and graphical demonstration of the dependence of the two variables on film thickness.

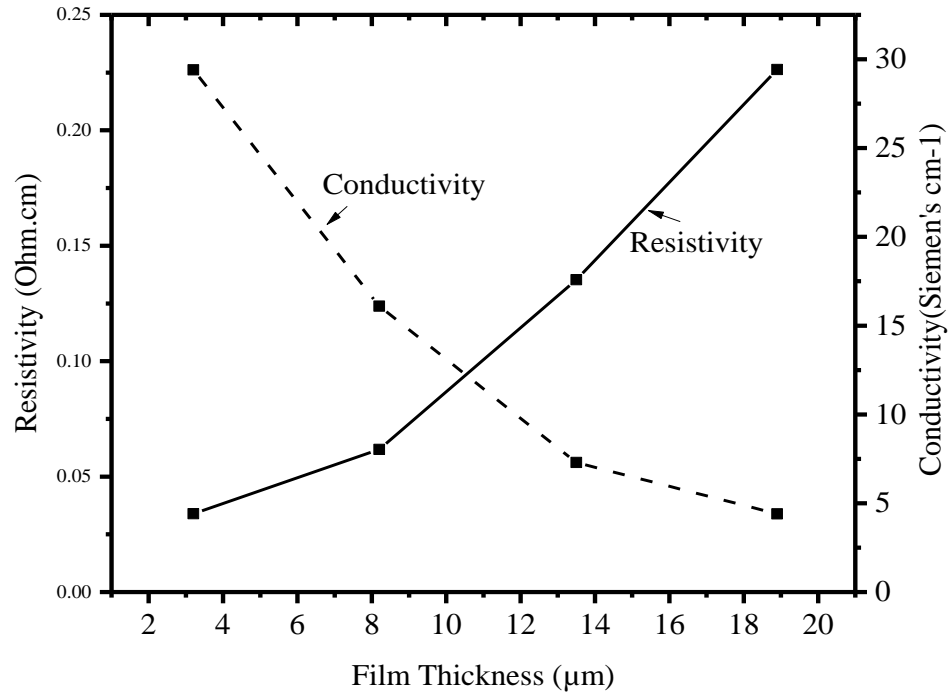


Figure 5.18: Resistivity and conductivity for TiO₂ thin films of various thicknesses

5.3.2 Effect of TiO₂ thin film porosity on resistivity and conductivity

The values of resistivity and their corresponding conductivity values for TiO₂ films (3.21 µm) at varying wt% carbon black are presented in table 5.5. The results show that resistivity increased with increase in porosity. On the other hand, conductivity decreased as the porosity of films increased. The artificial voids left the films with empty spaces occupied by carbon black before annealing. These voids tend to reduce electronic contacts among molecules of TiO₂. In this regard, as the porosity increased, the electronic contact among TiO₂ molecules reduced, hence conductivity decreased.

Table 5.5: Resistivity and conductivity of TiO₂ thin films (3.21 μm) with varying wt% carbon black

Carbo black (%)	Resistivity (10 ⁻³ Ω.cm)	Conductivity (Siemen's.cm ⁻¹)
0.5	2.60	384.61
1.0	2.84	352.11
1.5	9.67	103.41
2.0	19.08	52.41
3.0	28.33	35.29

As earlier explained in equation (5.1), conductivity is the inverse of resistivity therefore, it is logical to state that the increase in resistivity is the result of decrease in conductivity. Resistivity and conductivity dependence on porosity are graphically presented in figure 5.19. The results demonstrate clearly that conductivity and resistivity are inverses of each other.

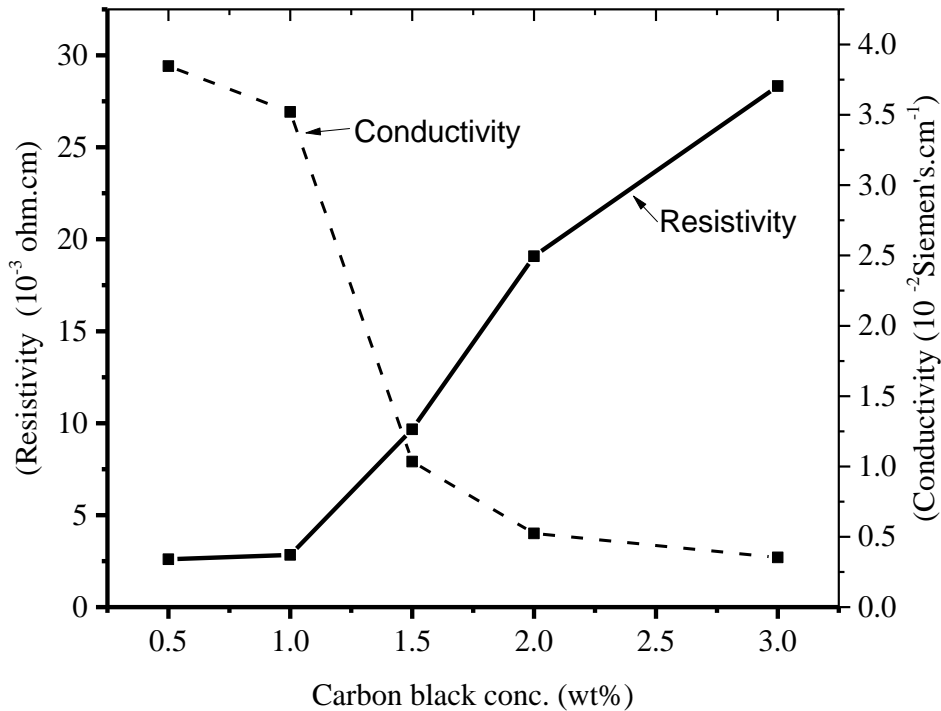


Figure 5.19: Resistivity and conductivity of TiO₂ thin films (3.21 μm) with different wt% of carbon black

5.4 Morphological and structural characterizations

5.4.1 Morphological characterizations (SEM and AFM)

Figure 2.20 shows the SEM images of TiO₂ films incorporated with 0 and 1.5 wt% carbon black. The film with 0 wt% carbon black shows a film that is crack-free and without artificial voids whereas, 1.5 wt% film shows voids on the surface. These are artificial pores created by the decomposition of carbon black upon the annealing of the film at 500 °C. This is a confirmation that carbon black really decomposed and left behind artificial pores.

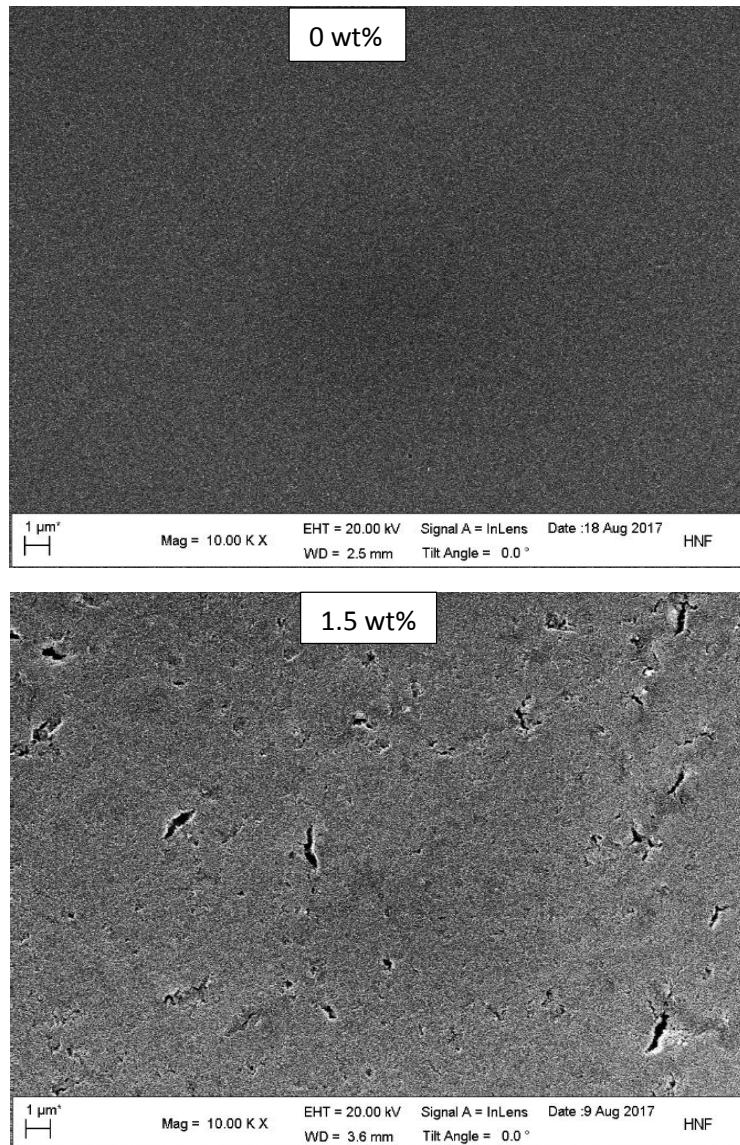


Figure 2.20: SEM images of TiO₂ 0 wt% and 1.5 wt% carbon black

SEM micrographs for films at varying wt % carbon black are presented in figure 5.21. Scanning electron microscopy (SEM) images show films that are crack-free, uniform and smooth on the surface. Samples exhibited nanocrystalline and nanoporous structure which consisted of nanoparticles. Examples of the voids left behind by the decomposition of carbon black are cycled in red. Image 0 wt% shows no artificial voids though there quite some pores which are characteristic properties of mesoporous TiO₂. There is a noticeable dark pigment in film 3.0 wt% due to incomplete decomposition of carbon black for its higher concentration in the film. Temperatures beyond 500 °C could decompose the carbon black completely but chances of phase change in TiO₂ was very high. The images revealed a corresponding increase in porosity with increase in carbon black concentration. Investigations reported earlier also revealed a similar trend with varying wt % acetylene black (Cho *et. al.*, 2013) and polystyrene spheres (Hore *et. al.*, 2005). In their investigations, artificial pores were observed in micrographs from SEM. The pores size increased with concentrations of either acetylene black or polystyrene spheres.

The artificial pores observed in these images support optical and electrical behavior discussed earlier in this chapter. These pores were responsible for the increased scattering ability in porous TiO₂. Light scattering was the factor responsible for the increased diffused reflectance observed in figure 5.7. In addition, these voids made photo-electrode to possess strong scattering capacity, a lot more of light intensity was reflected back to the inner TiO₂ photo-electrode, which enhanced the amount of light absorbed by the films hence the increased absorbance in the porous films as seen in figure 5.12. As observed in the SEM images, artificial voids increased with the rise in carbon black concentrations and the images show less contacts among TiO₂ molecules with higher carbon black concentrations.

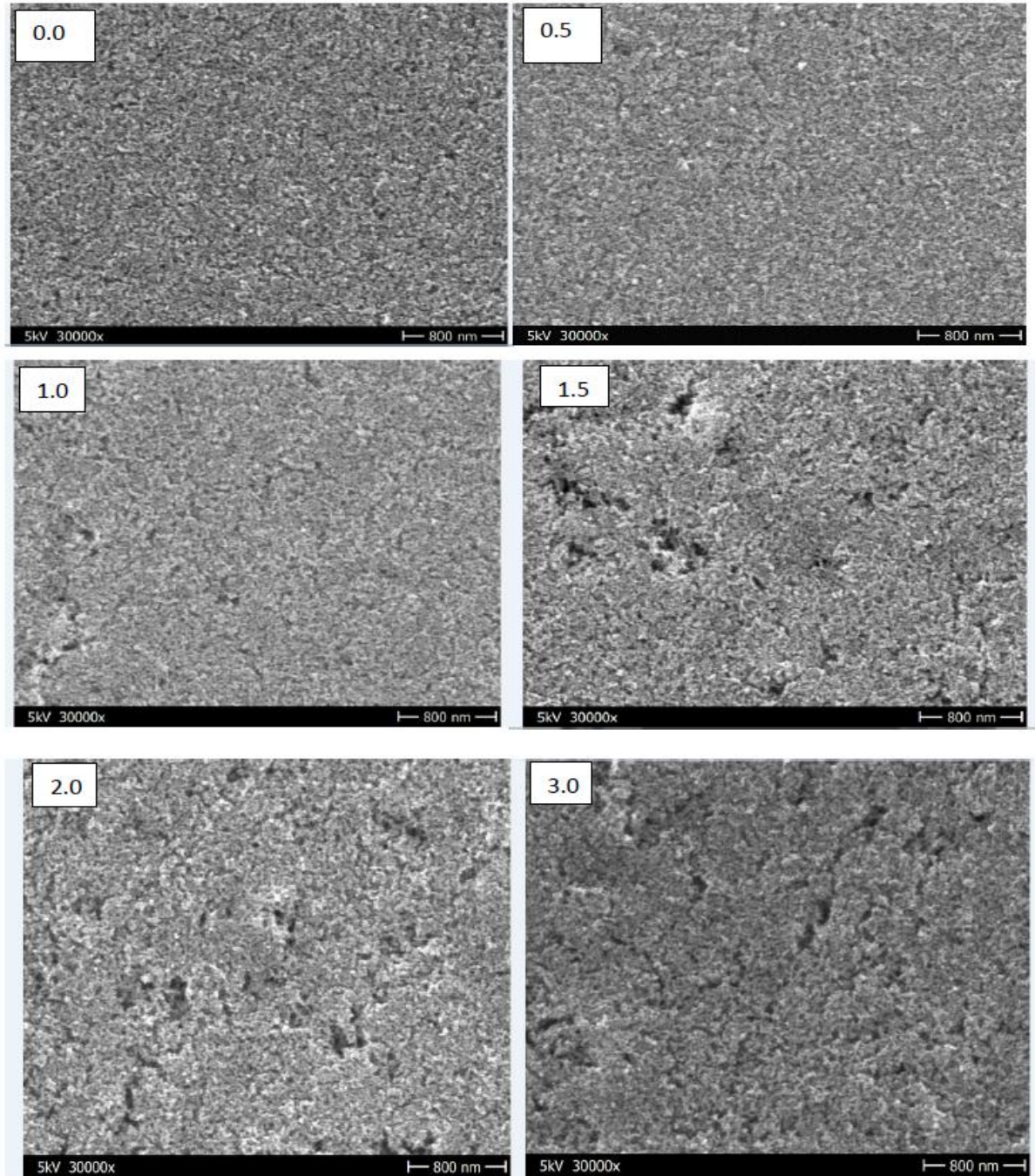


Figure 5.21: SEM micrographs for TiO₂ thin films with 0, 0.5, 1.0, 1.5, 2.0 and (f) 3 wt% carbon black.

Figure 5.22 shows the crystalline structure of TiO₂ film. This shows that the incorporation of the carbon has no effect on the crystalline nature of the nanoparticles and so also the purity of TiO₂ was not compromised.

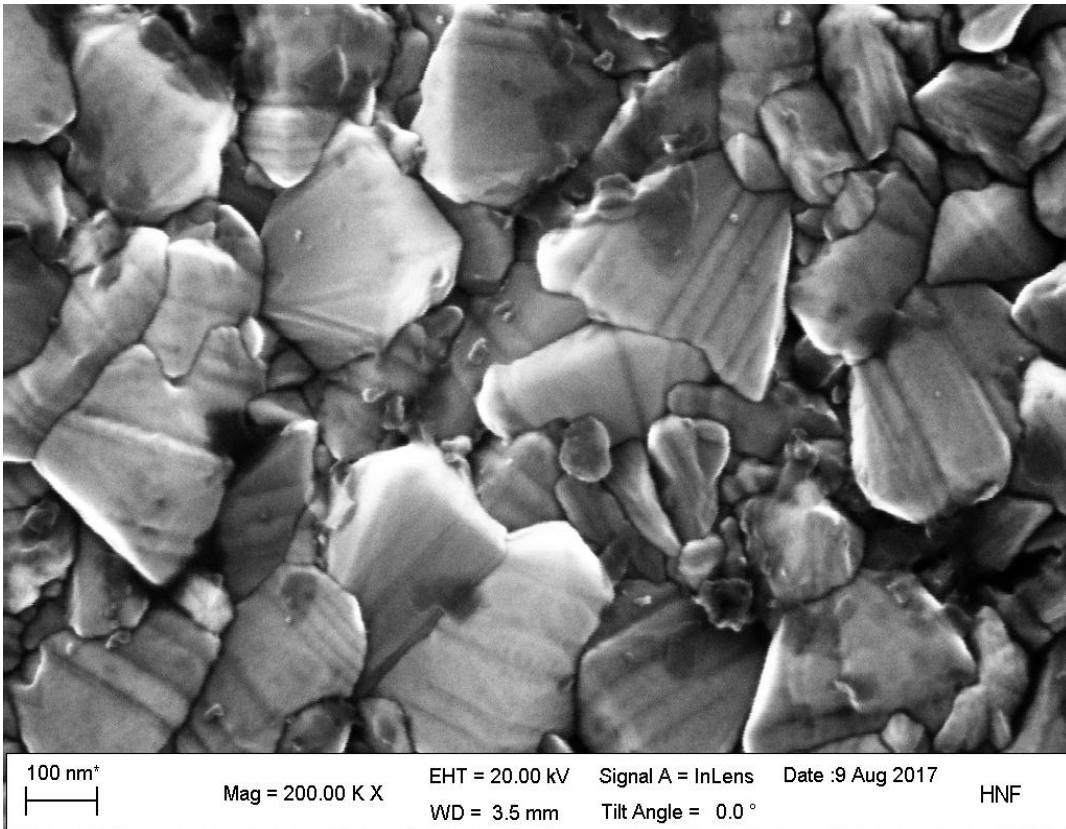


Figure 5.22: SEM micrograph for TiO₂ thin film with 1.5 wt% of carbon black.

AFM images are presented in figures 5.23 (a, b, c, d, e, and f). Images a, b, c, d, e and f represent 0, 0.5, 1.0, 1.5, 2.0 and 3.0 wt % respectively. Just like SEM images, the films are uniform, crack free and smooth on the surface. The films are nanocrystalline and nanoporous. The images show artificial pores created by the decomposition of carbon black. It can be seen that the images reveal clearly the influence of carbon black concentrations on porosity of the films. The images show that the higher the wt % carbon black, the higher the porosity. In image (a), there are no any artificial pores but the pores in images 0.5, 1.0, 1.5, 2.0 and 3.0 wt% are not just clearly visible but became more in size (number and dimension) as the wt% carbon black increased.

The AFM micrographs were in agreement with micrograph images from SEM in terms of porosity variation with carbon black concentrations.

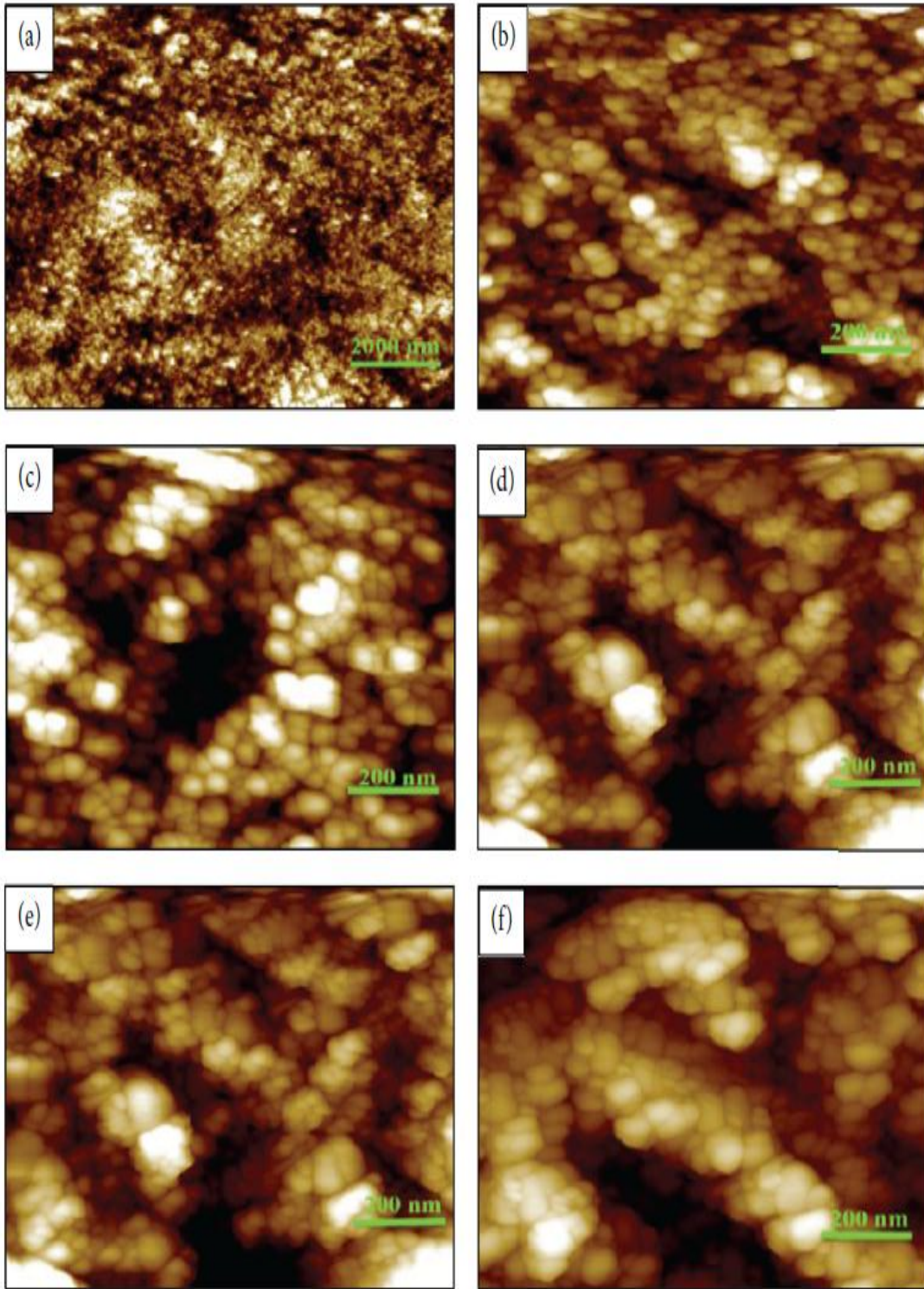


Figure 5.23: AFM images of TiO₂ thin films at varying wt % carbon black: (a) 0, (b) 0.5, (c) 1.0, (d) 1.5, (e) 2.0 and (f) 3.0

5.4.2 Structural characterizations (XRD)

X-ray diffraction (XRD) scans (Figure 5.24) show that the films produced were crystalline in nature (strong distinct peaks with different crystal orientations). Strong anatase peaks with crystal orientation directions (101) were observed for both films. The other peaks (004), (105), (211) and (213) are all for anatase phase (Swanson *et. al.*, 1968). The scans for the films from 0 and 1.5 wt% TiO₂ pastes were identical indicating that the carbon black really decomposed leaving just the voids without contaminating the films.

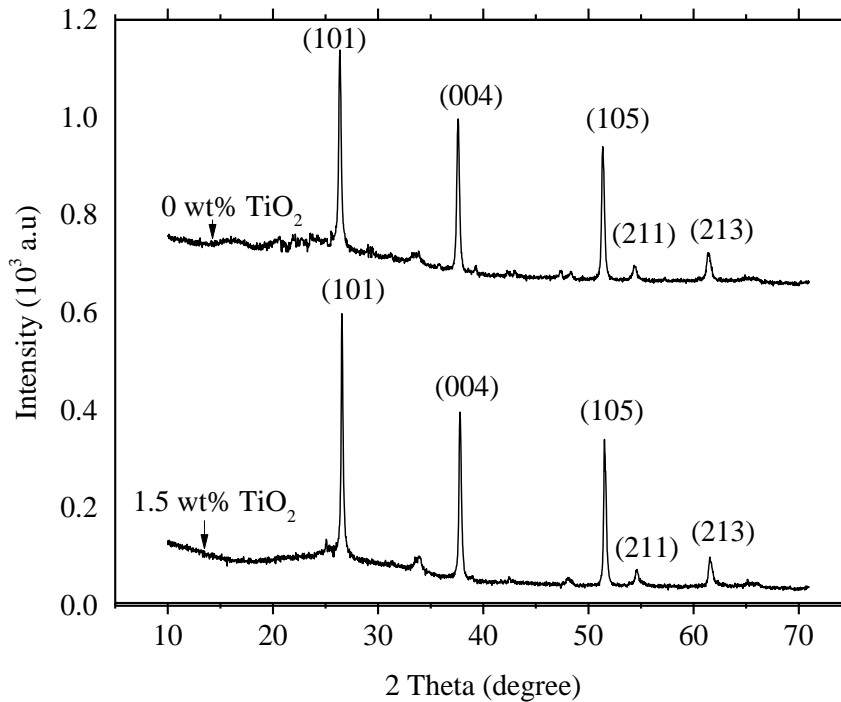


Figure 5.24: X-Ray diffraction pattern for TiO₂ thin films (13.52) at 0 and 1.5 wt% carbon black

Table 5.6 shows the peak list and particle size for TiO₂ thin film. Analysis of the peaks of XRD scans for both films using Scherer's formula show that anatase particles had particle sizes ranging from 19 nm to 28.98 nm. Though the nanoparticle size which is another key parameter for DSSC was found to a bit big, the charge injection efficiency is lowered with the decrease of the particle size due to reduced diffusion length (Nakade *et. al.*, 2003).

Table 5.6: Table showing peak list and particle size for TiO₂ film

Peak position (2 Theta)	h k l	Type	FWMH (2 Th.)	d-spacing (Å)	Particle size (nm)
26.577	1 0 1	Anatase	0.146	3.35495	28.98
37.810	0 0 4	Anatase	0.201	2.38025	24.36
51.580	1 0 5	Anatase	0.171	1.77133	24.22
54.605	2 1 1	Anatase	0.204	1.68089	21.64
61.610	2 1 3	Anatase	0.268	1.50607	21.36

5.5 Solar cells characterization

5.5.1 Effect of film thickness on *I-V* characteristics of DSSC

Figure 5.25 shows the *I-V* characteristics of solar cells at different film thickness under the intensity of 100 mW cm⁻². The films were sensitized with N719 dye. It was observed that open-circuit current density J_{sc} , increased with increase in film thickness (from 3.21 μm to 13.53 μm). This is attributed to the fact that thicker films adsorb more dye as observed earlier in the absorbance spectra of films in figure 5.10. More photon absorption is a consequence of higher dye adsorption which eventually yield to higher photocurrent generation. Previous investigations on film thickness of TiO₂ based DSSC revealed dye adsorption capacity of films increase with rise in film thickness (Wang *et. al.*, 2004). Increase in surface area as a result of the rise in film thickness provided more anchoring sites for dye molecules.

Table 5.7 shows the photovoltaic parameters of DSSC with film thickness of 3.2, 8.2, 13.5 and 18.9 μm. It was observed that J_{sc} increased as the films became thicker up to 13.5 μm and decreased afterwards. The increase in J_{sc} is as result of enhanced dye loading ability of the TiO₂ films with increase in film thickness. However, the cell with TiO₂ film thickness of 18.9 μm had a J_{sc} of 7.5 mA/cm² which is lower than the cell with TiO₂ film thickness of 13.5 μm which had J_{sc} of 8.2 mA/cm².

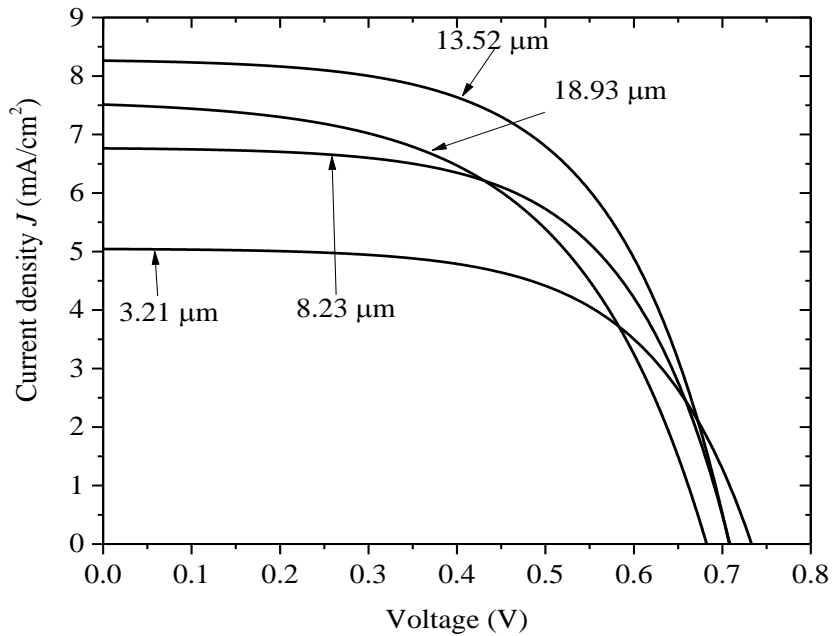


Figure 5.25: J-V characteristics for DSSC at varying film thickness.

This is attributable to low transmittance in film of thickness 18.9 μm as observed in figure 5.1 earlier. This low transmittance reduced the incident light intensity on the N719 dye and hence the decreased photocurrent. Research on the influence of TiO_2 film thickness on photovoltaic properties has provided lower transmittance in thicker films as reason for decrease in J_{sc} (Kao *et. al.*, 2009). In their findings, 13.5 μm was found to be the optimum thickness. Optimum film thickness was also reported to be within 5-20 μm (O'Regan and Grätzel, 1991; Grätzel, 2007) and this strongly corroborate the finding in this study.

Table 5.7: Cell parameters dependence on film thicknesses

Film thickness (μm)	J_{sc} (mA/cm^2)	V_{oc} (V)	FF	η (%)
3.21	5.0	0.731	0.634	2.4
8.23	6.7	0.714	0.630	3.0
13.52	8.2	0.711	0.604	3.5
18.93	7.5	0.687	0.544	2.8

Figure 5.26 shows the systematic dependence of photovoltaic parameters of DSSC at thickness of 3.21, 8.23, 13.52 and 18.93 μm .

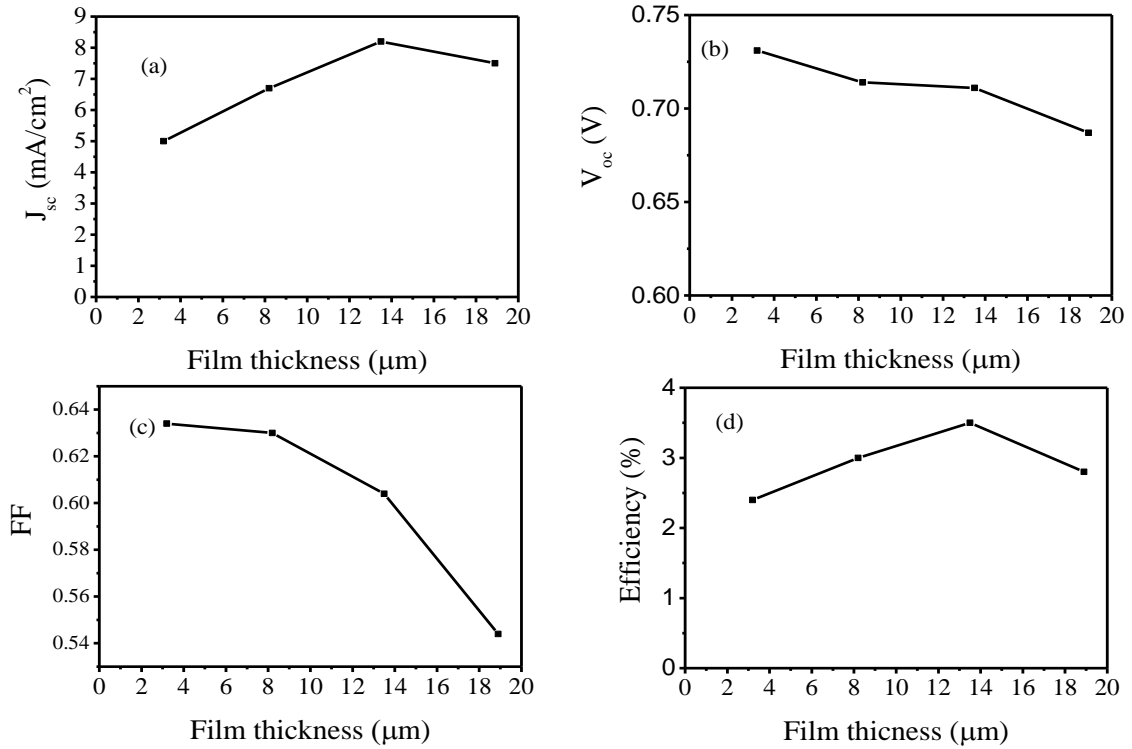


Figure 5.26: Dependence of photovoltaic parameters; (a) J_{sc} , (b) V_{oc} , (c), FF and (d) η on film thickness

Though the thickness dependence is also a function of particle size and surface structure; for example, optimal thickness for 20nm particles is half of that obtained for the 42 nm particles (Ito *et. al.*, 2009), previous investigations revealed that a typical film thickness for DSSC is 5–20 μm (Nazeeruddin *et. al.*, 2001) which is in agreement with this result. Contrary to the trend observed in the case of J_{sc} , it was found that due to enhanced dye adsorption with increase in film thickness, more electrons were produced under irradiation, hence the recombination of the photogenerated electrons at the surface of the TiO_2 films with oxidized species such as I_3^- in the electrolyte increased (M K Nazeeruddin *et. al.*, 1993) resulting to decrease in V_{oc} and FF as the film thickness increased. Other previous investigations also gave reason for decrease of V_{oc} with increase in TiO_2 film thickness as long diffusion of distance for the photoelectron to transport to the electrode hence

improving the probability of recombination (Meen *et al.*, 2014; Escalante *et al.*, 2013). It is also worthy to mention the contrary report of some researchers that V_{oc} increase with increase in film thickness (Kao *et al.*, 2009) though in extremely thin films. However in their case, the film thicknesses were in few microns which could be the reason why V_{oc} could still improve with film thickness.

5.5.2 Effect of electrolyte concentration on I - V characteristics of DSSC

The J - V curves of DSSCs against redox concentration of electrolyte is shown in figure 5.27. The cells were fabricated using N719 dye and had same film thickness of 13.5 (optimum).

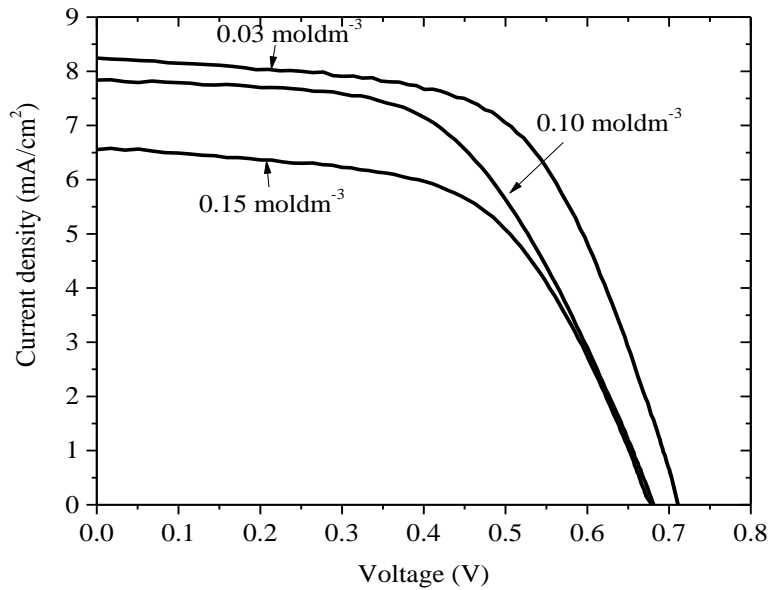


Figure 5.27: J - V characteristics for DSSC at different redox (I^-/I_3^-) concentrations.

Table 5.8 shows photovoltaic parameters of cells and figure 5.26 shows the dependence of J_{sc} and V_{oc} on the I^-/I_3^- concentration in electrolyte. The cells fabricated for these measurements had the same film thickness of 13.5 μm . It can be seen that 0.03 mol dm^{-3} concentration has the highest J_{sc} (8.2 mA cm^{-2}). J_{sc} decreased to 7.8 mA cm^{-2} and further to 6.5 mA cm^{-2} when I^-/I_3^- concentration was increased to 0.1 mol dm^{-3} and 0.15 mol dm^{-3} , respectively. The decrease of J_{sc} with increase in redox concentration is because of increase in viscosity of the solution, which reduces ion mobility in the solution, hence the lower J_{sc} . Similarly, V_{oc} decreased from 0.734 V to 0.679 V as the redox concentration

increased from 0.03 mol dm⁻³ to 0.15 mol dm⁻³, respectively. V_{oc} for DSSC with an iodine redox electrolyte is given as (Hara *et. al.*, 2001)

$$V_{oc} = \frac{kT}{e} \ln\left(\frac{I_{inj}}{n_{cb}k_{et}I_3^-}\right) \quad (5.2)$$

where I_{inj} is injection current from the dye molecule to the semiconductor, n_{cb} electron density, on the conduction band of semiconductor, and k_{et} is the rate constant of reduction of I_3^- to I^- (back electron transfer reaction as in equation (5.8) (Hara *et. al.*, 2001)

0



As seen in equation (5.2), V_{oc} decreases as back electron transfer increases. Therefore the decrease in V_{oc} with increase in I^-/I_3^- concentration is due to the enhanced back electron transfer reaction (Zhang *et. al.*, 2014). The results show that 0.03 mol dm⁻³ is the maximum optimum redox concentration for an iodide/triiodide electrolyte.

Table 5.8: Photovoltaic parameters versus redox (I^-/I_3^-) concentration in iodide/triiodide electrolyte

Redox conc. (mol/dm ³)	J_{sc} (mA/cm ²)	V_{oc} (V)	FF	η (%)
0.03	8.2	0.711	0.604	3.5
0.10	7.8	0.681	0.553	2.9
0.15	6.5	0.679	0.578	2.6

The systematic dependence of J_{sc} and V_{oc} on the I^-/I_3^- concentration in electrolyte is presented in figure 5.28

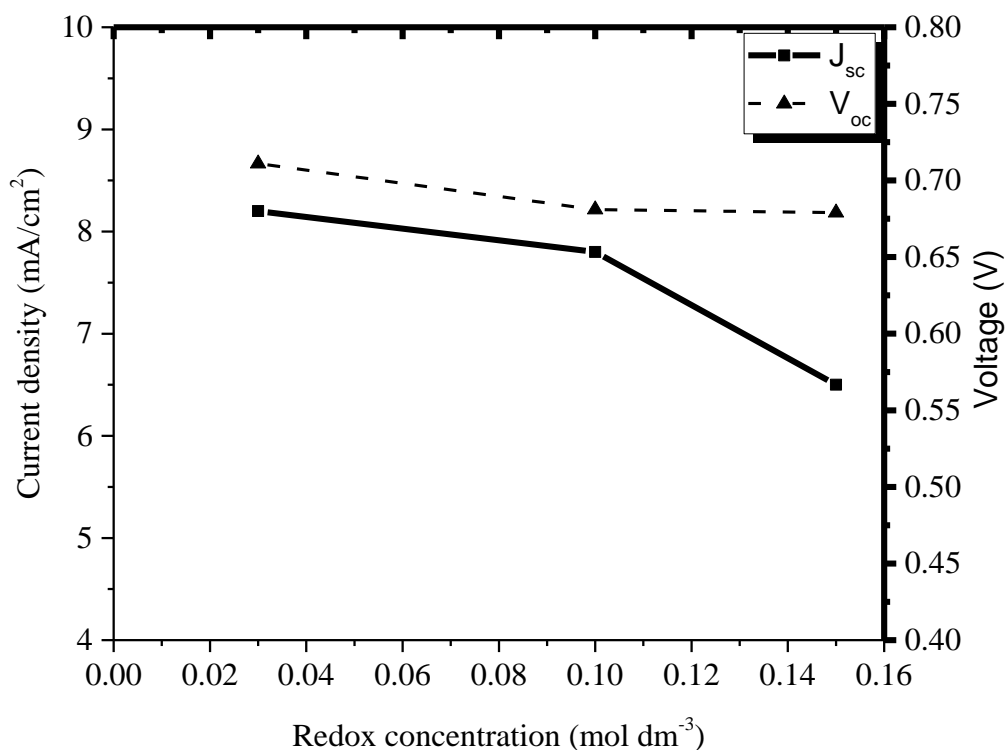


Figure 5.28: Dependence of J_{sc} and V_{oc} on the redox (I^-/I_3^-) concentration in iodide/tri-iodide electrolyte

5.5.3 Effect of light scattering (multi-reflection) on I - V characteristics of DSSC

The J - V curves of DSSC with and without double illumination is shown in figure 5.29. The cells were both fabricated using N749 dye and had the same optimum film thickness of 13.52 μm . The results show that the current density of the DSSC improved when a mirror was placed beneath the platinum electrode. Employing a mirror at the back of the Pt counter electrode of the cell changed the direction of propagation of the light and was reflected back to the Pt conductive glass. The light went through the Pt conductive glass through the electrolyte to the photoanode and increased the light absorption of the dye. This was responsible for the improvement of the photocurrent from 3.61 to 4.81 mA/cm^2 . Therefore the performance of the cell improved and the conversion efficiency increased from 1.42% to 1.83% as displayed in table 5.9. As seen in table 5.10, the V_{oc} also improved from 0.636 to 0.639 V. Since no other parameter was altered in the cells except for the employment of

the mirror, it means that the improvement in V_{oc} could be attributed to the increase photocurrent. From the equation,

$$V_{oc} = \frac{b}{q} T \ln \left(\frac{I_{ph}}{I_o} + 1 \right) \quad (5.4)$$

V_{oc} depends on I_{ph} therefore the increase in photocurrent by mirror is responsible for the improvement in the V_{oc} .

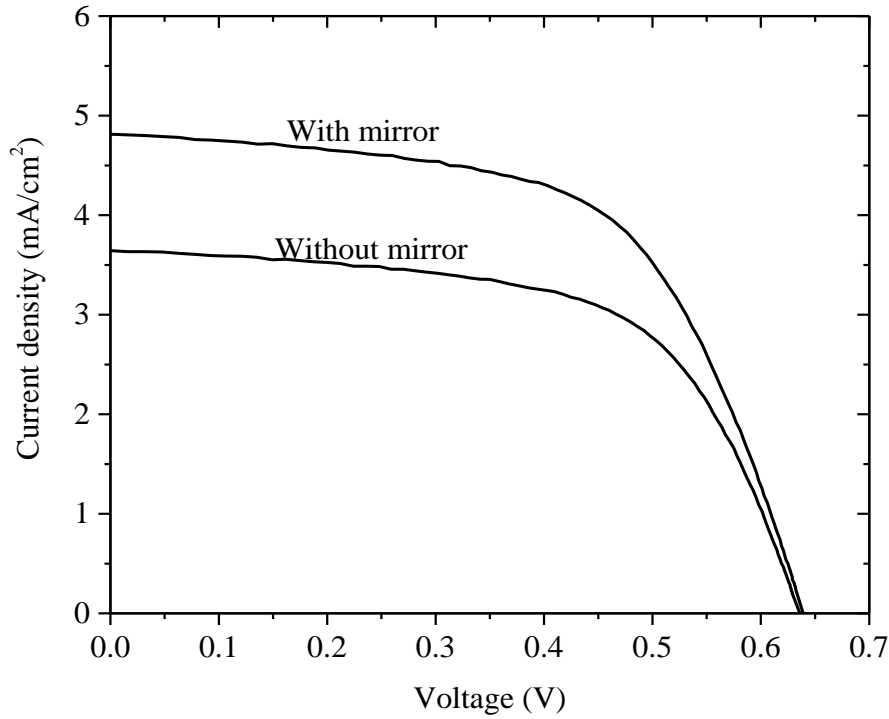


Figure 5.29: J-V characteristics for DSSC with and without reflection

Table 5.9: Dependence of cell parameters on multiple light scattering

Cell	Current density (mA/cm ²)	V_{oc} (V)	FF	Efficiency η (%)
Without mirror	3.65	0.636	0.607	1.42
With mirror	4.81	0.639	0.594	1.83

5.5.4 Effect of TiO₂ film porosity on the *I-V* characteristics of DSSC

Figure 5.30 shows the *I-V* characteristics for cells with films of different porosity. The result shows that photocurrent generated by these cells increased from 6.6 mA/cm² to a maximum value of 9.9 mA/cm² as the wt % carbon black increased from 0.5 wt% to 1.5 wt % respectively. The increase in photocurrent is a result of multi light scattering and increase in photon absorption due to artificial pores created (Cho *et. al.*, 2013). Artificial pores absorb more dye quantity hence higher photocurrent is generated. However, photocurrent began to depreciate as the increase in porosity continued. Photocurrent dropped to 1.4 mA/cm² at 3.0 wt % which is the least value recorded. This is because the increase in porosity leads to decrease in conductivity (as observed in figure 5.19) of the films hence less current generated. In addition, increasing porosity generates less current due to the reduction in the mass of TiO₂ per square centimeter of film as well as the effective TiO₂ surface per square centimeter (Barbe *et. al.*, 1997). Less surface area leads to a lower density of dye molecules adsorbed.

In table 5.10 which shows the photovoltaic parameters of cells with respect to films porosity, it is observed that open circuit voltage (V_{oc}) followed the same trend as the photocurrent. The V_{oc} increased up to the maximum value of 0.734 V at 1.5 wt % and thereafter began to decline until it got to its minimum value of 0.614 at 3 wt %. This is because the V_{oc} largely depends on the injection current (I_{inj}) from dye to semiconductor as in equation 5.7 (Hara *et. al.*, 2001). Since the TiO₂ mass reduction as a result of increased porosity reduces the injection current, the V_{oc} also reduces. Other investigations have also revealed similar trends as regards the variations of porosity with photovoltaic properties of dye sensitized solar cells (Pham *et. al.*, 2012; Cho *et. al.*, 2013). The dependence of Photovoltaic parameters on film porosity is presented in table 5.10.

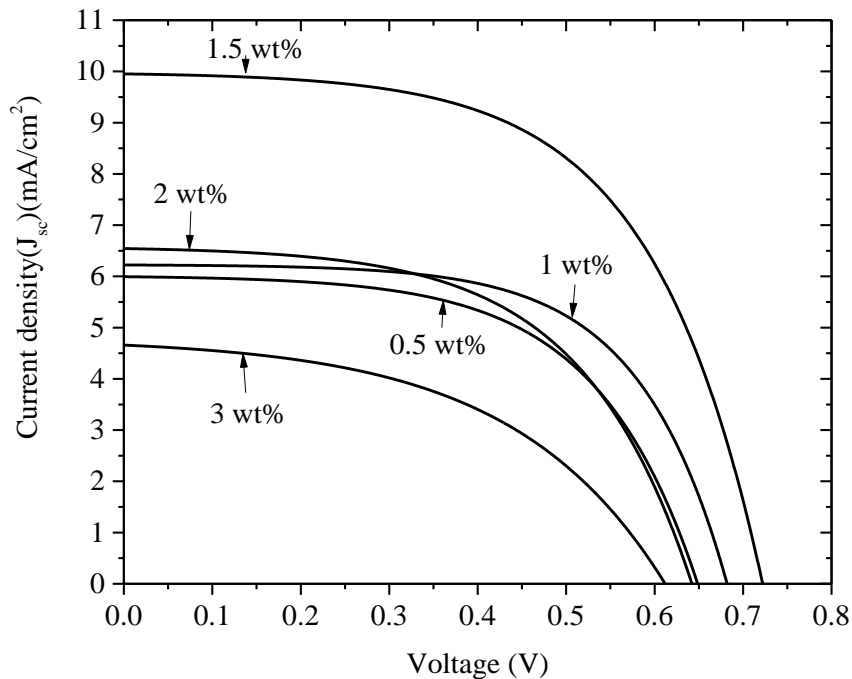


Figure 5.30: J-V characteristics for DSSC at varying concentrations of carbon black

Table 5.10: Parameters for DSSC at varying films porosity

wt % carbon black	J_{sc} (mA/cm ²)	V_{oc} (V)	FF	η (%)
0.5	6.1	0.653	0.571	2.3
1.0	6.4	0.687	0.599	2.6
1.5	9.9	0.734	0.592	4.3
2.0	6.7	0.647	0.551	2.4
3.0	4.7	0.614	0.482	1.4

The dependence of the overall cell efficiency on the porosity of films is presented in figure 31. The efficiency increased from 2.3 % at 0.5 wt % to a maximum 4.3% at 1.5 wt % and declined to 1.4% at 3.0 wt %. The concentration, 1.5 wt % carbon black was found to be the optimum for incorporation into the TiO₂ paste as clearly demonstrated in figure 5.31.

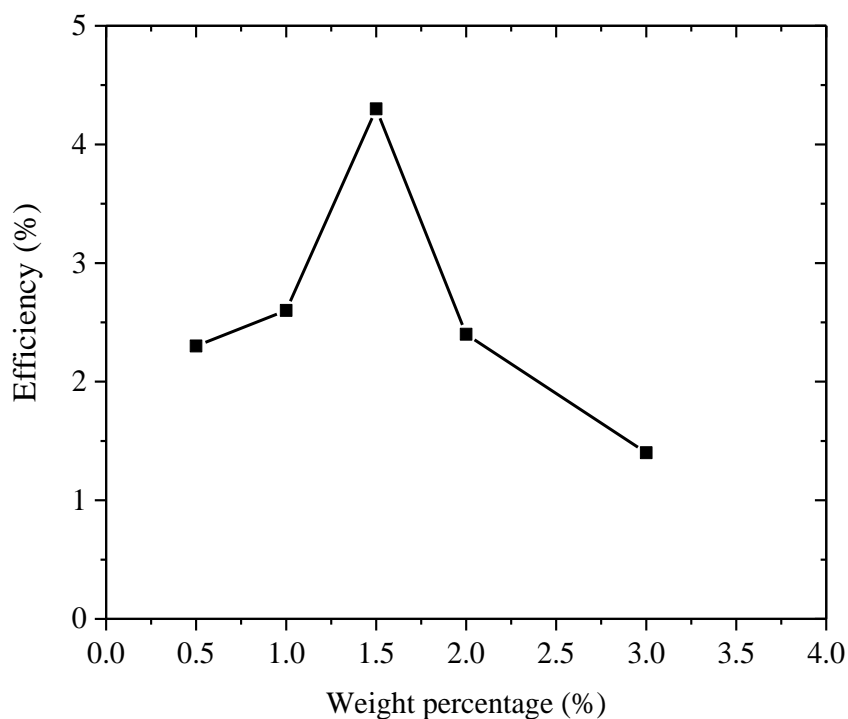


Figure 5.31: Dependence of cell efficiency on the porosity of films

The J-V characteristics of the best DSSCs with and without carbon black are presented in figure 5.32. For better comparison, the best of these cells are plotted together and it can be seen that the J_{sc} and V_{oc} increased from 8.2 mA/cm², 0.711 V and 3.5 % to 9.9 mA/cm², 0.734 V and 4.3% respectively due to porosity enhancement by the incorporation 1.5 wt % carbon black. The increase in efficiency represents 22.8 % which surpassed that reported in (Pham et. al., 2012; Cho et. al., 2013). Table 5.11 shows the photovoltaic parameters for best DSSCs with and without carbon black

Table 5.11: Photovoltaic parameters for best DSSCs with and without carbon black

Cell	J_{sc} (mA/cm ²)	V_{oc} (V)	FF	η (%)
0 wt% TiO ₂	8.2	0.711	0.604	3.5
1.5 wt% TiO ₂	9.9	0.734	0.592	4.3

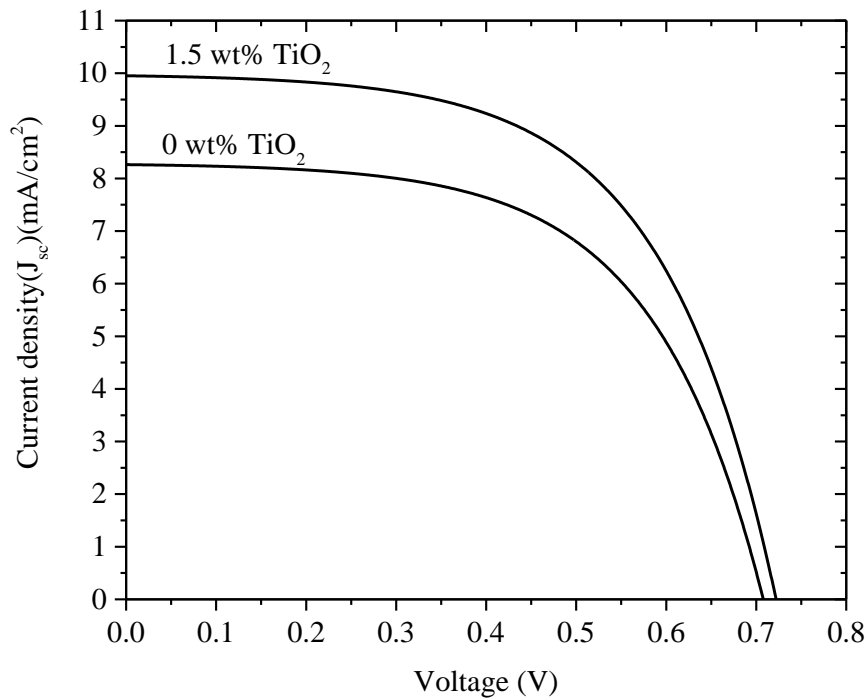


Figure 5.32: J-V characteristics for the best 0 wt% and 1.5 wt% carbon black based TiO₂ DSSCs

5.6 Electrochemical impedance spectroscopy (EIS) of DSSC

The Nyquist plots of DSSC based on the TiO₂ films of different thicknesses are shown in figure 5.33. The semicircles are related to charge transfer resistance at the FTO/TiO₂ (R_{FT}) or TiO₂/dye/electrode interfaces (R_{TDE}) (Fabregat-Santiago *et. al.*, 2007). In the case of the variation in thicknesses of electrodes, the interfacial resistance (R_{FT}) increases as the films become thicker. This is for the reason that thicker TiO₂ film has more trap states which block the movement of photo-generated electrons from TiO₂ layer to the FTO glass (Choi *et. al.*, 2012). Usually, a smaller diameter corresponds to lower interfacial resistance and lower interfacial charge recombination rate. The minimum R_{FT} is observed in 3.2 μm which is least in thickness. Investigations of *EIS* in TiO₂ based thin films of varying thicknesses have revealed the dependence of impedance on film thickness (Zhang *et. al.*, 2014). It therefore means that in the optimization of electrode thickness, impedance is also

considered. This finding also support the fact that highly thick films are not good for applications in dye sensitized solar cells even though they improve dye loading.

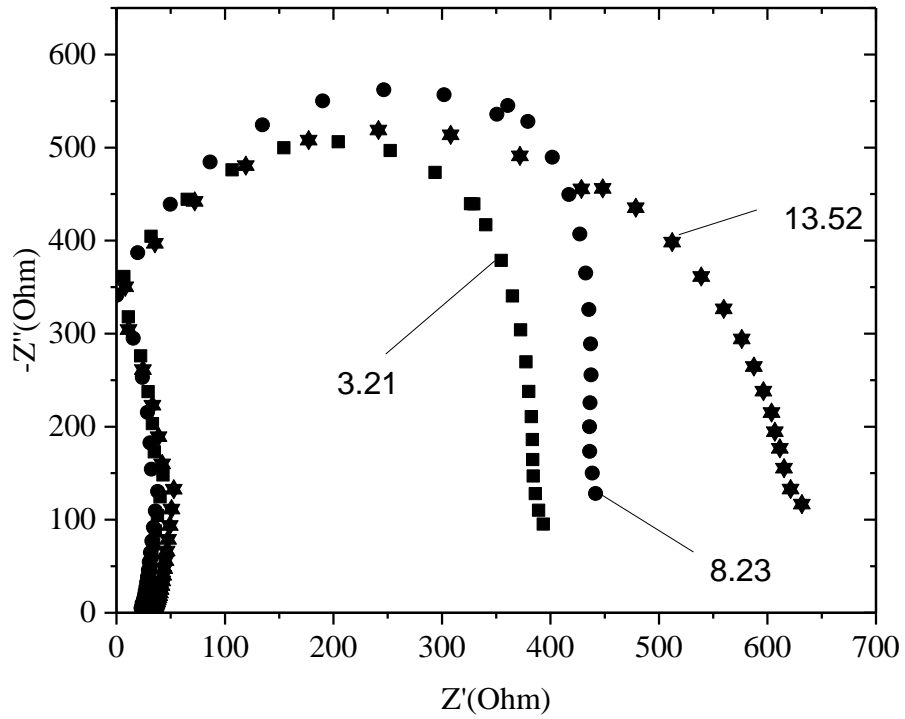


Figure 5.33: Nyquist plots of DSSCs based on film electrodes of different thicknesses.

CHAPTER SIX

CONCLUSION AND SUGGESTIONS FOR FURTHER STUDIES

6.1 Conclusion

Dye sensitized electrochemical solar cells employing TiO₂ thin films with and without carbon black have been fabricated by screen printing method. In addition, solar cells with varying thicknesses of TiO₂ films and different redox concentration of electrolyte have also been fabricated by screen printing and characterized. Screen printing method was found to be fast, simple, cost effective and highly reproducible. This method has actually demonstrated reliability and viability for commercial up scaling for the reason that a large number of cells were coated at a single any print.

In the investigation of optical properties of TiO₂ thin films, the films were found to be generally transparent. This shows that the films are suitable for application in dye sensitized solar cells due to the high transparency range of between 57 and 79%. The transmission of light through the films in the visible region was found to become lower as the film thickness increases. It is so because the films get denser as they get thicker thereby attenuating the passage of light. Similarly, spectral transmittance of these films also become lower as the porosity of films increases due to multi light scattering. On the other hand, the UV-Vis reflectance spectrum became higher with increase in film thickness as a result multi light scattering by increased surface roughness and volume reflection across the film. Investigation of the effect of porosity on the reflectance of films revealed that the more the porosity, the higher the reflectance spectrum. Due to light trapping and delay in optical path length, absorption ability of the films was also found to increase with film thickness and porosity. Increase in absorbance of the films make them suitable for applications in dye sensitized solar cells due high photon absorption. Other parameters computed from these measured spectra also demonstrated strong dependence on film thickness and porosity. Refractive index increases with increase in both film thickness and porosity while band gap is only affected by film thickness as it remains the same with variation in pored size. Coating more than once result to composite films hence the densification gives rise to higher refractive indices with more coatings. Summarily,

porosity and thickness of films have strong influence on the optical properties of TiO₂ thin films.

Electrical characterization shows that the films are generally conductive, which is an important property of films applicable in solar cells. Conductivity of the films become lower as the porosity and film thickness increase. In the case of porosity, the electronic contact between molecules become low as porosity increases hence conductivity decreases. The case of film thickness is attributed to increase in collisions between molecules as thickness increases. The thicker the films, the more the electrons, hence the more the collisions which result to higher resistivity of the films. Other the other hand, resistivity of the films become higher as film thickness and porosity increase. 1.5 wt % and 13.5 μm have shown average values for both resistivity and conductivity, which are considered favorable in the case of optimization.

In the study of the structural properties of the films, it can be concluded that the films were all anatase and the incorporation of carbon black in the paste could not change the structure of films. The particle size also ranges between 21 and 28 nm. Though the nanoparticle size which is another key parameter for DSSC is a little bit high, the charge injection efficiency is lowered with the decrease of the particle size due to reduced diffusion length. This shows that carbon black except at 3.0 wt % is completely decomposed at the temperature of 500 °C. SEM micrographs revealed smooth and crack-free films made of nanoparticles. The images revealed how the pores increase as the carbon black concentration increases. The pores do not just increase in dimension but also in number. From the AFM images, it can be clearly deduced that the pore dimensions increase as the carbon black increases. It can therefore be concluded that porosity enhancement has no negative effect on the films.

In the study of the effect of film thickness, it can be concluded that photocurrent generation rises with increase in film thickness. The surface area which becomes larger with film thickness actually provides more anchoring sites for dyes hence higher photocurrent. However, the photocurrent declines as the films get thicker to the extent of reducing light intensity on to the cell. The optimum film thickness was found to be 13.5 μm . It produced

the highest short circuit photocurrent density and open circuit voltage as well as overall cell efficiency.

Furthermore, the effect of electrolyte concentration was also investigated. Redox concentration of electrolyte was investigated and found to have strong effect on the photovoltaic properties of solar cell. The study revealed that redox (I/I_3) concentration influences the viscosity of the electrolyte which affects the ion mobility. Increase in redox concentration reduces ion mobility which in turn decreases the short circuit current density. In addition, redox concentration affects the back electron transfer reaction. In this case, the open circuit voltage becomes lower as the redox concentration increases. Summarily, as the redox concentration increases both short circuit current density and open circuit voltage decrease. 0.03 mol/dm^{-3} was found to be the optimum redox electrolyte concentration. This produced both the highest short circuit current density and open circuit voltage.

In the investigation of porosity effect, it can be concluded that porosity affect strongly the photovoltaic performance of dye sensitized solar cell. It was found that porosity affects dye absorption and hence photon absorption. Increase in porosity of film results to higher photocurrent generation. The study shows that as wt % carbon black increased, short circuit current density rose to the maximum and then dropped drastically to the lowest value at the highest wt % carbon black because of low conductivity. Similarly, the open circuit voltage rose to its maximum value and dropped to its least value with highest wt % of carbon black incorporated. It was found that at very high porosity, the TiO_2 mass density per square centimeter and surface area became so low that much current was no longer generated. Therefore an optimum value of 1.5 wt % carbon black was found. This concentration gave both the highest short circuit current density and open circuit voltage. So also the highest overall cell efficiency of 4.3 % was recorded.

Conclusively, the overall cell efficiency of dye sensitized solar cell based on normal TiO_2 thin film was 3.2 % while that based on pore enhanced TiO_2 film was found to be 4.3 %. In comparison, porosity enhancement resulted to 34.4 % increase in the overall efficiency.

This shows that a lot can be improved in the efficiency of a dye sensitized solar cell by improving on the porosity of films.

6.2 Suggestions for Further Studies

The study of dye sensitized solar cell remains clearly explorable both at fundamental and industrial levels. However, considering the work carried out in this thesis, the following areas require further investigations:

1. Charge transport in porous TiO₂:

Studies in the thesis have concluded based on overall cell efficiency that the optimum wt % carbon black and film thickness are 1.5 wt % and 13.5 μm respectively. However, there is still the need to investigate and understand the process of charge transport across the different film thickness and porosity. Negative effect on charge transport have been reported with thick films especially in dense electrolyte media. Therefore it is recommended that charge transport be investigated in dye sensitized solar cells based on porous TiO₂ films and cobalt complex.

2. Thermal gravimetric analysis of carbon black:

Though XRD and SEM results showed that except for 3.0 wt % carbon black, all the others were completely decomposed at the applied temperature, it is still necessary to carry out a thermo gravimetric analysis. This study will reveal the changes in the physical and chemical properties of carbon black as a function of increasing temperature (with constant heating rate). From this investigation, it can be concluded with precision the amount of temperature required to remove completely a particular amount of carbon black. This will not only guide energy usage, but prevents contamination of films.

3. Pore size and pore distribution characterization:

Variation in porosity as a result of the incorporation of varying wt % carbon black has been studied in this work. It was concluded from the SEM and AFM images that porosity increased with increase in carbon black concentration. However, detailed analysis is suggested to actually reveal the porosity in terms of numbers and also the distribution within the films with respect to carbon black concentration. Mere visual assessment of the images is inadequate.

REFERENCES

- Acharya, K. P., Khatri, H., Marsillac, S., Ullrich, B., Anzenbacher, P., & Zamkov, M. (2010). Pulsed Laser Deposition of Graphite Counter Electrodes for Dye-Sensitized Solar Cells. *Applied Physics Letters*, **97**, 201108–201111. <https://doi.org/10.1063/1.3518481>
- Aksay, S., & Altiocka, B. (2007). Effect of substrate temperature on some of the optical parameters of CuInS₂ films. *Physica Status Solidi (C)*, **4**(2), 585–588. <https://doi.org/10.1002/pssc.200673236>
- Albery, W John and Bartlett, N. P. (1984). The Transport and Kinetics of Photogenerated Carriers in Colloidal Semiconductor Electrode Particles. *Journal of the Electrochemical Society*, **131**(2), 315–325. <https://doi.org/10.1149/1.2115568>
- Andrade, L., Zakeeruddin, S. M., Nazeeruddin, M. K., Ribeiro, H. A., Mendes, A., & Grätzel, M. (2009). Influence of sodium cations of N3 dye on the photovoltaic performance and stability of dye-sensitized solar cells. *ChemPhysChem*, **10**(7), 1117–1124. <https://doi.org/10.1002/cphc.200900111>
- Arakawa, H., Yamaguchi, T., Takeuchi, A., Agatsuma, S., Tio, M. and Tio, T. (2008). Efficiency Improvement of Dye-Sensitized Solar Cell by Light Confined Effect. *2006 IEEE 4th World Conference on Photovoltaic Energy Conference*. <https://doi.org/10.1109/WCPEC.2006.279340>
- Avrutin, V., Izyumskaya, N., & Morko, H. (2011). Semiconductor solar cells: Recent progress in terrestrial applications. *Superlattices and Microstructures*, **49**(4), 337–364. <https://doi.org/10.1016/j.spmi.2010.12.011>
- Barbe, C. J., Arendse, F., Comte, P., Jirousek, M., Lenzmann, F., Shklover, V. and Grätzel, M. (1997). Nanocrystalline titanium oxide electrodes for photovoltaic applications. *Journal of American Ceramic Society*, **80**(12), 3157–3171. <https://doi.org/10.1111/j.1151-2916.1997.tb03245.x>
- Bard, A. J., & Faulkner, L. R. (2000). *Fundamentals and Applications* (2nd edition). New York: *Wiley and Sons*. ISBN 0-471-04372-9
- Belaidi, A., Dittrich, T., Kieven, D., Tornow, J., Schwarzburg, K., & Lux-Steiner, M. (2008). Influence of the local absorber layer thickness on the performance of ZnO nanorod solar cells. *Physica Status Solidi - Rapid Research Letters*, **2**(4), 172–174. <https://doi.org/10.1002/pssr.200802092>
- Benanti, T. L., & Venkataraman, D. (2006). Organic solar cells: An overview focusing on active layer morphology. *Photosynthesis Research*, **87**(1), 73–81. <https://doi.org/10.1007/s11120-005-6397-9>

- Bird, G. (1839). Observations on the application of heliographic or photogenic drawing to botanical purposes; with an account of an economic mode of preparing the paper. *Journal of the Franklin Institute of the State of Pennsylvania, and Mechanics Register*, **24**(3), 202. <https://doi.org/10.1021/ar900141y>
- Bourdon, J. (1965). Spectral Sensitization of Chemical Effects in Solids. *Journal of Physical Chemistry*, **69**(3), 705. <https://doi.org/10.1021/j100887a001>
- Cai, N., Moon, S., Zakeeruddin, S. M., & Grätzel, M. (2011). An Organic D- π -A Dye for Record Efficiency Solid-State Sensitized Heterojunction Solar Cells. *Nano Letters*, **11**, 1452–1456. <https://doi.org/10.1021/nl104034e>
- Calzolari, A., Ruini, A., Catellani, A., Fisica, D., Emilia, R., & Modena, I. (2011). Anchor Group versus Conjugation : Toward the Gap-State Engineering of Functionalized ZnO (1010) Surface for Optoelectronic Applications. *Journal of the American Chemical Society*, **133**, 5893–5899. <https://doi.org/10.1021/ja1101008>
- Chapin, D. M., Fuller, C. S., & Pearson, G. L. (1954). A new silicon p-n junction photocell for converting solar radiation into electrical power [3]. *Journal of Applied Physics*, **25**(5), 676–677. <https://doi.org/10.1063/1.1721711>
- Chen, D., Huang, F., Cheng, Y. B., & Caruso, R. A. (2009). Mesoporous anatase TiO₂ beads with high surface areas and controllable pore sizes: A superior candidate for high-performance dye-sensitized solar cells. *Advanced Materials*, **21**(21), 2206–2210. <https://doi.org/10.1002/adma.200802603>
- Cho, T.-Y., Han, C.-W., Jun, Y., & Yoon, S.-G. (2013). Formation of artificial pores in nano-TiO₂ photo-electrode films using acetylene-black for high-efficiency, dye-sensitized solar cells. *Scientific Reports*, **3**, 1496. <https://doi.org/10.1038/srep01496>
- Chuangchote, S., Sagawa, T., Yoshikawa, S., Chuangchote, S., Sagawa, T., & Yoshikawa, S. (2013). Efficient dye-sensitized solar cells using electrospun TiO₂ nanofibers as a light harvesting layer. *Applied Physics Letters*, **33310**, 2012–2015. <https://doi.org/10.1063/1.2958347>
- Daguerre, L. (1839). Practical Definition of Deguerotype. *Journal of the Franklin Institute*, 303. <https://doi.org/10.1021/ic0508371>
- Duonghond, D., Serpone, N., & Grätzel, M. (1984). Integrated Systems for Water Cleavage by Visible Light; Sensitization of TiO₂ Particles by Surface Derivatization with Ruthenium Complexes. *Helvetica Chimica Acta*, **67**(4), 1012–1018. <https://doi.org/10.1002/hlca.19840670413>

- Escalante-Quijano, R., García-Rodríguez, R., Heredia-Cervera, B. E., Gómez-Ortíz, N., Villanueva-Cab, J., & Oskam, G. (2013). Influence of TiO₂ Film Thickness on the Performance of Dye-Sensitized Solar Cells: Relation between Optimum Film Thickness and Electron Diffusion Length. *Energy and Environment us*, **2**(4), 280–286. <https://doi.org/10.1166/eef.2014.1064>
- ExxonMobil Energy outlook. (2012). Retrieved December 27, 2016, from <http://www.geoexpro.com/articles/2012/09>
- Ferber, J and Luther, J. (1998). Computer simulations of light scattering and absorption in dye-sensitized solar cells. *Solar Energy Materials and Solar Cells*, **54**, 265–275. PII: S 0 9 27- 0 2 48(98)0 007 8-6
- Ferrere, S., Zaban, A., and Gregg, B. A. (1997). Dye Sensitization of Nanocrystalline Tin Oxide by Perylene Derivatives. *Journal of Physical Chemistry B*, **5647**(97), 4490–4493.
- Fujishima, A and Honda, K. (1971). Electrochemical Evidence for the Mechanism of the Primary State of Photosynthesis. *Bulletin of the Chemical Society of Japan*, **44**, 1148-1150. <https://doi.org/10.1246/bcsj.44.1148>
- Geiger, T., Kuster, S., Yum, J. H., Moon, S. J., Nazeeruddin, M. K., Grätzel, M. and Nüesch, F. (2009). Molecular Design of Unsymmetrical Squaraine Dyes for High Efficiency Conversion of Low Energy Photons into Electrons using TiO₂ Nanocrystalline Films. *Advanced Functional Materials*, **19**(17), 2720–2727. <https://doi.org/10.1002/adfm.200900231>
- Ghrairi, N., and Bouaicha, M. (2012). Structural, Morphological, and Optical Properties of TiO₂ Thin Films Synthesized by the Electrophoretic Deposition Technique. *Nanoscale Research Letters*, **7**(1), 357. <https://doi.org/10.1186/1556-276X-7-357>
- Grätzel, M. (2001). Photoelectrochemical Cells. *Insight Review Articles*, **414**, 338-344. www.nature.com
- Grätzel, M. (2000). Perspectives for Dye -sensitized Nanocrystalline Solar Cells. *Progress in Photovoltaics Research and Applications*, **8**(1), 171–185.
- Grätzel, M. (2003). Dye-sensitized solar cells. *Journal of Photochemistry and Photobiology C: Photochemistry Reviews*, **4**(2), 145–153. [https://doi.org/10.1016/S1389-5567\(03\)00026-1](https://doi.org/10.1016/S1389-5567(03)00026-1)
- Grätzel, M. (2005). Solar Energy Conversion by Dye-Sensitized Photovoltaic Cells. *Inorganic Chemistry* **44**(20), 6841–6851. <https://doi.org/10.1021/ic0508371>
- Grätzel, M. (2009). Recent Advances in sensitized Mesoscopic Solar Cells. *Accounts of Chemical Research*, **42**(11), 1788–1798. <https://doi.org/10.1021/ar900141y>
- Green, M. A. (2006). Third Generation Photovoltaics. *Springer -Verlag Berlin Heidelberg, Netherlands*. ISSN: 1437-0379

- Green, M.A., Emery, K., Hishikawa, Y., Warta, W. and Dunlop, D. D. (2016). Solar Cells Utilizing Small Molecular Weight Organic Semiconductors. *Progress in Photovoltaic: Res. Appl.*, **24**, 3–11. <https://doi.org/10.1002/pip2728>
- Greene, L. E., Law, M., Yuhas, B. D., & Yang, P. (2007). ZnO - TiO₂ Core - Shell Nanorod / P3HT Solar Cells. *Journal of Physical Chemistry C*, **111**(50), 18451–18456. <https://doi.org/10.1021/jp077593l>
- Hagfeldt, A., and Grätzel, M. (1995). Light-Induced Redox Reactions in Nanocrystalline Systems. *Chemical Reviews*, **95**, 49–68. PII: 0009-2665/95/0795-0049\$15.50/0
- Hagfeldt A., Boschloo, G., Sun L., Kloo L. and P. H. (2010). Dye-sensitized Solar Cells. *Chemical Reviews*, **110**(11), 6595–6663. <https://doi.org/10.1016/B978-0-12-374774-7.00007-8>
- Hamadani, M., Gravand, A., Farangi, M., and Jabbari, V. (2011). The Effect of the Thickness of Nanoporous TiO₂ Film on the Performance of Nanocrystalline Dye-Sensitized Solar Cell. *SASTech 5th Symposium on Advances in Science in Technology* (pp. 1–9). <https://doi.org/10.1016/j.solmat.2005.07.002>
- Hao, S., Wu, J., Fan, L., Huang, Y., Lin, J. and Wei, Y. (2004). The Influence of Acid Treatment of TiO₂ Porous Film Electrode on Photoelectric Performance of Dye-sensitized Solar Cell. *Solar Energy*, **76**(6), 745–750. <https://doi.org/10.1016/j.solener.2003.12.010>
- Hattori, S., Wada, Y., Yanagida, S., & Fukuzumi, S. (2005). Blue Copper Model Complexes with Distorted Tetragonal Geometry Acting as Effective Electron-Transfer Mediators in Dye-sensitized Solar Cells. *Journal of the American Chemical Society*, **127**(26), 9648–9654. <https://doi.org/10.1021/ja0506814>
- Hauch, A. and Georg, A. (2001). Diffusion in the Electrolyte and Charge-transfer Reaction at the Platinum Electrode in Dye-sensitized Solar Cells. *Electrochimica Acta*, **46**(22), 3457–3466. [https://doi.org/10.1016/S0013-4686\(01\)00540-0](https://doi.org/10.1016/S0013-4686(01)00540-0)
- Hore, S., Nitz, P., Vetter, C., Prahl, C., Niggemann, M., and Kern, R. (2005). Scattering Spherical Voids in Nanocrystalline TiO₂- enhancement of Efficiency in Dye-Sensitized Solar Cells. *Chemical Communications (Cambridge, England)*, **(15)**, 2011–2013. <https://doi.org/10.1039/b418658n>
- Hore, S., Vetter, C., Kern, R., Smit, H., and Hirsch, A. (2006). Influence of scattering layers on efficiency of dye-sensitized solar cells. *Solar Energy Materials and Solar Cells* **90**, 1176–1188. <https://doi.org/10.1016/j.solmat.2005.07.002>
- Horiuchi, T., Miura, H., Uchida, S., Paper, M., Limited, M., and Exciter, X. (2003). Highly-efficient Metal-free Organic Dyes for Dye-sensitized solar cells. *Chemical Communications*, **24**, 3036–3037. <https://doi.org/10.1016/j.jphotochem.2003.12.018>

- Huang, Z., Liu, X., Li, K., Li, D., Luo, Y., Li, H., Song, W., Chen, L. and Meng, Q. (2007). Application of Carbon Materials as Counter Electrodes of Dye-Sensitized Solar Cells. *Electrochemistry Communications*, **9**, 596–598. <https://doi.org/10.1016/j.elecom.2006.10.028>
- Huang, C.Y., Hsu, Y.C., Chen, J.G., Surnarayanan, V., Lee, K. C. H. (2006). The Effects of Hydrothermal Temperature and Thickness of TiO₂ Film on the Performance of a Dye-Sensitized Solar Cell. *Solar Energy Materials and Solar Cells*, **90**, 2391–2397. <https://doi.org/10.1016/j.solmat.2006.03.012>
- Hyung, S., Kim, J., Sik, H., Koh, H., Lee, J. and Sung, Y. (2008). Chemistry Influence of Light Scattering Particles in the TiO₂ Photoelectrode for Solid-State Dye-Sensitized Solar Cell. *Journal of Photochemistry and Photobiology A*, **200**, 294–300. <https://doi.org/10.1016/j.jphotochem.2008.08.010>
- Intergovernmental Panel on Climate Change. (2014). Climate Change 2014: Mitigation of Climate Change: Working Group III Contribution to the Fifth Assessment Report of the Intergovernmental Panel on. *New York: Cambridge University Press*. <http://www.ipcc.ch/index.htm>
- Ito, S., Nazeeruddin, M. K., Zakeeruddin, S. M., Péchy, P., Comte, P., Grätzel, M., Mizuno, T., Tanaka, A. and Koyanagi, T. (2009). Study of Dye-Sensitized Solar Cells by Scanning Electron Micrograph Observation and Thickness Optimization of Porous TiO₂ Electrodes. *International Journal of Photoenergy*, **2009**(4), 12–14. <https://doi.org/10.1155/2009/517609>
- Jena, A., Mohanty, S. P., Kumar, P., Naduvath, Johns Gondane, V., Lekha, P., Das, J., Narula, H.K., Malik, S. and Bhargava, P. (2012). Dye Sensitized Solar Cells : A Review Dye Sensitized Solar Cells : A Review. *Transactions of the Indian Ceramic Society*, **71**(1), 1–16. <https://doi.org/10.1080/0371750X.2012.689503>
- Kang, T.-S., Smith, A., Taylor, B. and Durstock, M. (2009). Fabrication of Highly-ordered TiO₂ Nanotube Arrays and their use in Dye-Sensitized Solar Cells. *Nano Letters*, **9**(2), 601–606. <https://doi.org/10.1021/nl802818d>
- Kangarlou, H., and Rafizadeh, S. (2012). Influence of Thickness on Structural and Optical Properties of Titanium Oxide Thin Layers. *Scanning Probe Microscopy-Physical Property Characterization at Nanoscale*. Intech. www.intechopen.com
- Kao, M. C., Chen, H. Z., Young, S. L., Kung, C. Y., and Lin, C. C. (2009). The Effects of the Thickness of TiO₂ Films on The Performance Of Dye-Sensitized Solar Cells. *Thin Solid Films*, **517**(17), 5096–5099. <https://doi.org/10.1016/j.tsf.2009.03.102>
- Kay, A., and Grätzel, M. (1996). Low Cost Photovoltaic Modules Based on Dye Sensitized Nanocrystalline Titanium Dioxide and Carbon Powder. *Solar Energy Materials Solar Cells*, **44**(1), 99–117. PII: S0927-0248(96)00063-3.

- Kay, A., Grätzel and Grätzel, M. (2002). Article Dye-Sensitized Core – Shell Nanocrystals : Improved Efficiency of Mesoporous Tin Oxide Electrodes Coated with a Thin Layer of an Insulating Oxide. *Chemical Materials*, **14**, 2930–2935. <https://doi.org/10.1021/cm0115968>
- Kelly, C. A., Farzad, F., Thompson, D. W., Stipkala, J. M., and Meyer, G. J. (1999). Cation-controlled Interfacial Charge Injection in Sensitized Nanocrystalline TiO₂. *Langmuir*, **15**(20), 7047–7054. <https://doi.org/10.1021/la990617y>
- Kim, S. Y. (1996). Simultaneous Determination of Refractive Index, Extinction Coefficient, and Void Distribution of Titanium Dioxide Thin Film by Optical Methods. *Applied Optics*, **35**(34), 6703–7. <https://doi.org/10.1364/AO.35.006703>
- Kittel, C. (1996). Introduction to Solid State Physics. 7th Edition, New York, USA: *John Wiley and Sons*.
- Kong, F., Dai, S., and Wang, K. (2007). Review of Recent Progress in Dye-Sensitized Solar Cells. *Advances in Optoelectronics*. **2007**, 13 pages. <https://doi.org/10.1155/2007/75384>
- Kumari, J. M. K. W., Sanjeevadharsini, N. and Dissanayake, M. A. K. L. (2016). The Effect of TiO₂ Photoanode Film Thickness on Photovoltaic Properties of Dye-Sensitized Solar Cells. *Ceylon Journal of Science*, **45**(1), 33–41. [https://doi.org/10.1016/0013-4686\(80\)80054-5](https://doi.org/10.1016/0013-4686(80)80054-5)
- Lee, S., Jun, Y., Kim, K. and Kim, D. (2001). Modification Of Electrodes in Nanocrystalline Dye-Sensitized. *Solar Energy Materials and Solar Cells*, **65**, 193–200. PII: S 0 9 2 7 - 0 2 4 8 (0 0) 0 0 0 9 5 – 7
- Listorti, A., O’Regan, B. and Durrant J.R. (2011). Electron Transfer in Dye-Sensitized Solar Cells. *Chemistry of Materials*, **23**, 3381–3399. <https://doi.org/10.1021/cm200651e>
- Liu, H., Avrutin, V., Izyumskaya, N., Özgr, Ü. and Morkoç, H. (2010). Transparent Conducting Oxides for Electrode Applications in Light Emitting and Absorbing Devices. *Superlattices and Microstructures*, **48**(5), 458–484. <https://doi.org/10.1016/j.spmi.2010.08.011>
- Ma, X., Hua, J., Wu, W., Jin, Y., Meng, F., Zhan, W., and Tian, H. (2008). A High-Efficiency Cyanine Dye for Dye-Sensitized Solar Cells. *Tetrahedron*, **64**(2), 345–350. <https://doi.org/10.1016/j.tet.2007.10.094>
- Malliga, P., Pandiarajan, J., Prithivikumaran, N. and Neyvasagam, K. (2014). Influence of Film Thickness on Structural and Optical Properties of Sol – Gel Spin Coated TiO₂. *Thin Film*, **6**(1), 22–28. www.iosrjournals.org

- Mardare, D., Tasca, M., Delibas, M., & Rusu, G. I. (2000). Structural Properties and Optical Transmittance of TiO₂ r.f. Sputtered Thin Films. *Applied Surface Science*, **156**(1), 200–206. [https://doi.org/10.1016/S0169-4332\(99\)00508-5](https://doi.org/10.1016/S0169-4332(99)00508-5)
- Martinson, A., Elam, J., Hupp, J. and Pellin, M. (2007). ZnO Nanotube Based Dye-sensitized Solar Cells. *Nano Letters*, **7**(8), 2183–2187. <http://pubs.acs.org/doi/abs/10.1021/nl070160+>
- Mathew, S., Yella, A., Gao, P., Humphry-Baker, R., Curchod, B. F. E., Ashari-Astani, N., Tavernelli, I, Rothlisberger U., Nazeeruddin, M.K. and Grätzel, M. (2014). Dye-Sensitized Solar Cells With 13% Efficiency Achieved Through the Molecular Engineering of Porphyrin Sensitizers. *Nature Chemistry*, **6**(3), 242–247. <https://doi.org/10.1038/nchem.1861>
- Meen, T. H., Tsai, J. K., Tu, Y. S., Wu, T. C., Hsu, W. D., and Chang, S. (2014). Optimization of the Dye-Sensitized Solar Cell Performance by Mechanical Compression. *Nanoscale Research Letters*, **9**, 1–8. <http://www.nanoscalereslett.com/content/9/1/523>
- Memming, R. (1980). Solar Energy Conversion by Photoelectrochemical Processes. *Electrochimica Acta*, **25**, 77–88. [https://doi.org/10.1016/0013-4686\(80\)80054-5](https://doi.org/10.1016/0013-4686(80)80054-5)
- Miao, L., Tanemura, S., Tanemura, M., Lau, S. P. and Tay, B. K. (2007). Thickness-Dependent Optical Properties of ZnO Thin Films. *Journal of Materials Science: Materials in Electronics*, **18**(1), 343–346. <https://doi.org/10.1007/s10854-007-9243-3>
- Mishra, A., Fischer, M. K. R. and Bäuerle, P. (2009). Metal-Free Organic Dyes for Dye-Sensitized Solar Cells : From Structure : Property Relationships to Design Rules. *Angewandte Chemie*, **48**, 2474–2499. <https://doi.org/10.1002/anie.200804709>
- Murakoshi, K., Kogure, R., Wada, Y., & Yanagida, S. (1997). Solid State Dye-Sensitized TiO₂ Solar Cell with Polypyrrole as H₂O₂ Transport Layer. *Chemistry Letters*. <https://doi.org/10.1246/cl.1997.471>
- Nakade, S., Saito, Y., Kubo, W., Kitamura, T., Wada, Y. and Yanagida, S. (2003). Influence of TiO₂ Nanoparticle Size on Electron Diffusion and Recombination in Dye-Sensitized TiO₂ Solar Cells. *The Journal of Physical Chemistry B*, **107**(33), 8607–8611. <https://doi.org/10.1021/jp034773w>
- National Renewal Laboratory (2016). <https://www.nrel.gov/>.
- Nazeeruddin, M. K., Kay, A., Rodicio, I., Humhpry-Baker, R., Müller, E., Liska, P., Vlachopoulos, N. and Grätzel, M. (1993). Conversion of Light to Electricity by SCN⁻ on Nanocrystalline TiO₂ Electrodes. *Journal of American Chemical Society*, **115**(4), 6382–6390. <https://doi.org/10.1021/ja00067a063>

- Nazeeruddin, M. K., Péchy, P., & Grätzel, M. (1997). Efficient Panchromatic Sensitization of Nanocrystalline TiO₂ Films by a Black dye Based on a trithiocyanato-ruthenium complex. *Chemical Communications*, **1**(18), 1705–1706. <https://doi.org/10.1039/a703277c>
- Nazeeruddin, M.K., Pèchy, P., Renouard, T., Zakeeruddin, S.M., Baker, R.H., Comte, P., Liska, P., Cevey, L., Costa, E., Shklover, V., Spiccia, L., Deacon, G.B., Bignozzi, C.A. and Grätzel (2001). Engineering of Efficient Panchromatic Sensitizers for Nanocrystalline TiO₂-based Solar Cells. *Journal of American Chemical Society*, **123**, 1613-1624. <https://doi.org/10.1021/ja003299u>
- Nelson, J. (2003). Physics of Solar Cells. Imperial College, **30**, London: Imperial College. <https://doi.org/10.1149/1.2115568>
- Nelson, J. (2010). Lecture Notes for Winter College on Optics and Energy. ICTP, 2132(2).
- Nelson, K., & Deng, Y. (2008). Effect of polycrystalline structure of TiO₂ particles on the light scattering efficiency. *Journal of Colloid and Interface Science*, **319**, 130–139. <https://doi.org/10.1016/j.jcis.2007.09.037>
- Nelson, R. C. (1965). Minority Carrier Trapping and Dye Sensitization1. *Journal of Physical Chemistry*, **69**(1), 714–718. <https://doi.org/10.1021/j100887a002>
- O'Regan, B and Grätzel, M. (1991). A Low-cost High-efficiency Dye-sensitized Solar Cell based on Colloidal TiO₂ Thin Films. *Nature*, **353**, 737–740. <https://doi.org/10.1038/350055a0>
- Olsen, E., Hagen, G. and Lindquist, S.E. (2000). Dissolution of Platinum in Methoxy Propionitrile Containing LiI/I₂. *Solar Energy Materials and Solar Cells*, **63**(3), 267–273. [https://doi.org/10.1016/S0927-0248\(00\)00033-7](https://doi.org/10.1016/S0927-0248(00)00033-7)
- Oskam, G., Bergeron, B. V, Meyer, G. J. and Searson, P. C. (2001). Pseudohalogens for Dye-Sensitized TiO₂ Photoelectrochemical Cells. *Journal of Physical Chemistry B*, **105**, 6867–6873. [https://doi.org/10.1016/S0927-0248\(00\)00023-8](https://doi.org/10.1016/S0927-0248(00)00023-8)
- Pankove, J. I. (1990). Optical Processes in Semiconductors. *Dover Publications*, **41**(5), 2796–2807. ISBN: 1 3-638023-9
- Park, J., Barolo, C., Sauvage, F., Barbero, N., Benzi, C., Quagliotto, P., Coluccia, S., Censo, D. D., Grätzel, M., Nazeeruddin, M.K. and Viscardi, G. (2012). Symmetric vs. Asymmetric Squaraines as Photosensitisers in Mesoscopic Injection solar cells: A structure–property Relationship Study. *Chemical Communications*, **48**, 2782–2784. <https://doi.org/10.1039/c2cc17187b>
- Park, J., Viscardi, G., Barolo, C., and Barbero, N. (2013). Near-infrared Sensitization in Dye- sensitized Solar Cells. *Solar Energy Harvesting*, **67**(3), 129–135. <https://doi.org/10.2533/chimia.2013.129>

- Pham, T. T., Bessho, T., Mathews, N., Zakeeruddin, S. M., Lam, Y. M., Mhaisalkar, S. and Grätzel, M. (2012). Light Scattering Enhancement from Sub-micrometer Cavities in the Photoanode for Dye-sensitized Solar Cells. *Journal of Materials Chemistry*, **22**(32), 16201. <https://doi.org/10.1039/c2jm32401f>
- Pulker, H. K. (1984). Coatings on glass. *Thin Film Science and Technology*, **6**, 254.
- Ravirajan, P., Peir, A. M., Nazeeruddin, M. K., Graetzel, M., Bradley, D. D. C., Durrant, J. R. and Nelson, J. (2006). Hybrid Polymer / Zinc Oxide Photovoltaic Devices with Vertically Oriented ZnO Nanorods and an Amphiphilic Molecular Interface Layer Hybrid Polymer / Zinc Oxide Photovoltaic Devices with Vertically Oriented ZnO Nanorods and an Amphiphilic Molecular Interfa. *Journal of Physical Chemistry B*, **110**, 7635–7639. <https://doi.org/10.1021/jp0571372>
- Rommel, T., Gregory, R. and Baumert, B. (1999) Characterisation of Barium Strontium Titanate Films Using XRD. *International Centre for Diffraction Data*, 38-45
- Rensmo, H., Keis, K., Lindstrom, H., Sodergren, S., Solbrand, A., & A. Hagfeldt. (1997). High Light-to-energy Conversion Efficiencies for Solar Cells Based on Nanostructured (ZnO) Electrodes. *Journal of Physical Chemistry B*, **101**, 2598–2601. S1089-5647(96)02918-5
- Rodriguez, J., Gomez, M., Ederth, J., Niklasson, G. A., and Granqvist, C. G. (2000). Thickness Dependence of the Optical properties of Sputter Deposited Titanium Oxide Films. *Thin Solid Films*, **365**(1), 119–125.
- Rothenberger, G., Comte, P. and Grätzel, M. (1999). A Contribution to the Optical Design of Dye - sensitized Nanocrystalline Solar Cells. *Solar Energy Materials and Solar Cells*, **58**, 321–336. PII: S 0 9 2 7 - 0 2 4 8 (9 9) 0 0 0 1 5 -X
- Saito, Y., Kitamura, T., Wada, Y. and Yanagida, S. (2002). Poly (3, 4-ethylenedioxythiophene) as a Hole Conductor in Solid State Dye Sensitized Solar Cells. *Synthetic Metals*, **131**(1–3), 185–187. PII: S0379-6779(02)00198-4
- Sandler, M. W. (2002). Photography : New York: *Oxford University Express*. ISBN: 0-19-512608-4
- Santiago, F.F., Bisquert, J., Bisquert, J., Palomares, E., Otero, L., Kuang D., Zakeeruddin S.M. and Grätzel, M. (2007). Correlation between Photovoltaic Performance and Impedance Spectroscopy of Dye-Sensitized Solar Cells Based on Ionic Liquids. *Journal of Physical Chemistry C*, **111**(17), 6550–6560. <https://doi.org/10.1021/jp066178a>

- Sapp, S. A, Elliott, C. M., Contado, C., Caramori, S, and Bignozzi, C. A. (2002). Substituted Polypyridine Complexes of Cobalt (II / III) as Efficient Electron-Transfer Mediators in Dye-Sensitized Solar Cells Substituted Polypyridine Complexes of Cobalt (II / III) as Efficient Electron-Transfer Mediators in Dye-Sensitized Solar Cel. *Journal of American Chemical Society*, **124**, 11215–11222. <https://doi.org/10.1021/ja027355y>
- Sedghi, A. and Miankushki, H. N. (2015). The Effect of Drying and Thickness of TiO₂ Electrodes on the Photovoltaic Performance of Dye-Sensitized Solar Cells. *International Journal of Electrochemical Science*, **10**, 3354–3362.
- Sharma, R., Mane, R. S., Min, S. K. and Han, S. H. (2009). Optimization of growth of In₂O₃ nano-spheres thin films by electrodeposition for dye-sensitized solar cells. *Journal of Alloys and Compounds*, **479**(1–2), 840–843. <https://doi.org/10.1016/j.jallcom.2009.01.070>
- Shockley, W. & Queisser, H. J. (1961). Detailed Balance Limit of Efficiency of p- n Junction Solar Cells. *Journal of Applied Physics*, **32**(4),510. <https://doi.org/10.1063/1.1736034>
- Shockley, W., and Read, W. T. (1952). Statistics of the Recombinations of Holes and Electrons. *Physical Review*, **87**(5), 835. <https://doi.org/10.1103/PhysRev.87.835>
- Simiyu, J. (2010). Characterization of Anthocyanin Dyes and Investigation of Charge Transport in TiO₂ Dye Sensitized Solar Cells . *University of Nairobi Thesis*.
- Smestad, G., Bignozzi, C. and Argazzi, R. (1994). Testing of Dye-Sensitized TiO₂ Solar-Cells: Experimental Photocurrent Output and Conversion Efficiencies. *Solar Energy Materials and Solar Cells*, **32**(3), 259–272. 0927-0248/94/\$07.00
- Smestad, G. P. (1998). Education and Solar Conversion: *Solar Energy Materials and Solar Cells*, **55**(1–2), 157–178. [https://doi.org/10.1016/S0927-0248\(98\)00056-7](https://doi.org/10.1016/S0927-0248(98)00056-7)
- Snaith, H. J., and Ducati, C. (2010). SnO₂-Based Dye-sensitized Hybrid Solar Cells Exhibiting Near Unity Absorbed Photon-to-electron Conversion Efficiency. *Nano Letters*, **10**(4), 1259–1265. <https://doi.org/10.1021/nl903809r>
- Södergren, S., Hagfeldt, A. and Lindquist, S. (1994). Theoretical Models for the Action Spectrum and the Current-Voltage Characteristics of Microporous Semiconductor Films in Photoelectrochemical Cells. *Journal of Physical Chemistry*, **98**, 5552–5556. 0022-3654/94/2098-5552\$04.50/
- Somani, P. R., & Radhakrishnan, S. (2003). Sensitization Effect in Doped and Undoped State of Polypyrrole by Methylene Blue in Solid State Electrochemical Cells. *Chemical Physics Letters*, **379**(5–6), 401–405. <https://doi.org/10.1016/j.cplett.2003.08.053>

- Suryanarayana, C. and Norton, M. G. (1998). X-Ray Diffraction A Practical Approach. New York: *Plenum Press*. <https://doi.org/10.1007/978-1-4899-0148-4> ISBN
- Swanson, H.E., McMurdie, H.F., Morris, M.C and Evans, E. H. (1968) Standard X-ray Diffraction Powder Patterns. *United States National Bureau of Standards*
- Sze, S. M. (1981). Physics of Semiconductor Devices. New York: *Willey International Publishers Inc*. <https://doi.org/10.1021/ja00067a063>
- Tang, H., Berger, H., Schmid, P. E., Levy, F., Appliquee, D. P. and Polytechnique, E. (1994). *Solid State Communications*, **92**(3), 267–271. [https://doi.org/1098\(94\)00454-X](https://doi.org/1098(94)00454-X)
- Tributsch, H. (1971). Application of Electrochemical Kinetics to Photosynthesis and Oxidative Phosphorylation: The Redox Element Hypothesis and the Principle of Parametric Energy Coupling. *Journal of Bioenergetics*, **2**, 249–273. <https://doi.org/10.1007/BF01963823>
- Tsai, J. K., Hsu, W. D., Wu, T. C., Meen, T. H. and Chong, W. J. (2013). Effect of Compressed TiO₂ Nanoparticle Thin Film Thickness on the Performance of Dye-Sensitized Solar Cells. *Nanoscale Research Letters*, **8**(1), 459. <https://doi.org/10.1186/1556-276X-8-459>
- U.S Energy Information Administration. (2016). International Energy Outlook 2016. <http://www.eia.gov/forecasts/ieo/world.cfm>
- Usami, A. (1997). Theoretical Study of Application of Multiple Scattering of Light to a Dye-Sensitized Nanocrystalline Photoelectrochemical Cell. *Chemical Physics Letters*, **277**, 105–8. [https://doi.org/10.1016/S0009-2614\(97\)00878-6](https://doi.org/10.1016/S0009-2614(97)00878-6)
- Valdes, L.B., Member, I. (1954). Resistivity Measurements on Germanium for Transistors. *Proceedings of the I.R.E*, **29**, 420–427. <https://doi.org/10.2533/chimia.2013.129>
- Viet, A. Le, Jose, R., Reddy, M. V, Chowdari, B. V. R., & Ramakrishna, S. (2010). Nb₂O₅ Photoelectrodes for Dye-Sensitized Solar Cells : *Choice of the Polymorph*, **114**(49), 21795–21800. <https://doi.org/10.1021/jp106515k>
- Wang, H., & Hu, Y. H. (2012). Graphene as a Counter Electrode Material for Dye-Sensitized Solar Cells. *Energy and Environmental Science*, **5**(8), 8182–8188. <https://doi.org/10.1039/c2ee21905k>
- Wang, P., Zakeeruddin, S. M., Exnar, I. and Grätzel, M. (2002). High Efficiency Dye-sensitized Nanocrystalline Solar Cells Based on Ionic Liquid Polymer Gel Electrolyte. *Chemical Communications*, **8**(24), 2972–2973. <https://doi.org/10.1039/b209322g>
- Wang, P., Zakeeruddin, S. M., Moser, J.-E., Humphry-Baker, R., & Grätzel, M. (2004). A Solvent-Free, SeCN⁻/(SeCN)³⁻-Based Ionic Liquid Electrolyte for High-

- Efficiency Dye-Sensitized Nanocrystalline Solar Cells. *Journal of the American Chemical Society*, **126**(23), 7164–7165. <https://doi.org/10.1039/b209322g>
- Wang, Z. S., Kawauchi, H., Kashima, T., & Arakawa, H. (2004). Significant Influence of TiO₂ Photoelectrode Morphology on the Energy Conversion Efficiency of N719 Dye-Sensitized Solar Cell. *Coordination Chemistry Reviews*, **248**(13–14), 1381–1389. <https://doi.org/10.1016/j.ccr.2004.03.006>
- Weerasinghe, H. C., Huang, F., & Cheng, Y.-B. (2013). Fabrication of Flexible Dye Sensitized Solar Cells on Plastic Substrates. *Nano Energy*, **2**(2), 174–189. <https://doi.org/10.1016/j.nanoen.2012.10.004>
- Weisstein, Eric W. "Torque." *Eric Weisstein's World of Physics*. <http://scienceworld.wolfram.com/physics/Torque.html>.
- Wetstone, G., Thornton, K., Hinrichs-rahlwes, R., Sawyer, S., Sander, M., Taylor, Rodgers, D., Alers, M., Lehmann, H. and Eckhart, M. and Hales, D. (2016). UAE, Renewables Global Status Report.
- Williams, R. (1960). Bequerel photovoltaic Effect in Binary Compounds. *Journal of Chemical Physics*, **32**(5), 1505–1514. <https://doi.org/10.1063/1.1730950>
- Wu, W., Hua, J., Jin, Y., Zhan, W. and Tian, H. (2008). Photovoltaic Properties of Three New Cyanine Dyes for Dye-Sensitized Solar Cells. *Photochemical & Photobiological Sciences: Official Journal of the European Photochemistry Association and the European Society for Photobiology*, **129**, 10320–10321. <https://doi.org/10.1039/b712439b>
- Wu, X., Lu, G., & Wang, L. (2013). The Effect of Photoanode Thickness on the Performance Of Dye-Sensitized Solar Cells Containing TiO₂ Nanosheets with Exposed Reactive {001} Facets. *Journal of Materials Research*, **28**(3), 475–479. <https://doi.org/10.1557/jmr.2012.372>
- Wüfel, P. (2005). *Physics of Solar Cells: From Principles to New Concept*. Verlag: Willey VCH.
- Xu, Z., Zhang, F., Zhang, R.-J., Yu, X., Zhang, D.-X., Wang, Z.Y., Zheng, Y.X., Wang, S.Y., Zhao, S.B. and Chen, L.-Y. (2013). Thickness Dependent Optical Properties of Titanium Oxide Thin Films. *Applied Physics A Materials Science and Processing*. <https://doi.org/10.1007/s00339-013-7591-9>
- Yakuphanoglu, F., Sekerci, M., & Ozturk, O. F. (2004). The Determination of the Optical Constants Of Cu(II) Compound having 1-Chloro-2,3-O-Cyclohexylidinepropane Thin Film. *Optics Communications*, **239**(4–6), 275–280. <https://doi.org/10.1016/j.optcom.2004.05.038>

- Yang, L., Lin, Y., Jia, J., Xiao, X., Li, X., & Zhou, X. (2008). Light Harvesting Enhancement for Dye-Sensitized Solar Cells by Novel Anode Containing Cauliflower-like TiO₂ Spheres, 1 and 2. *Journal of Power Science*, **182**, 370–376. <https://doi.org/10.1016/j.jpowsour.2008.03.013>
- Yella, A., Lee, H.-W., Tsao, H. N., Yi, C., Chandiran, A. K., Nazeeruddin, M. K., Diao, E.W.G., Yeh, C.Y., Zakeeruddin, S.M. and Grätzel, M. (2011). Porphyrin-Sensitized Solar Cells with Cobalt (II/III)-Based Redox Electrolyte Exceed 12 Percent Efficiency. *Science*, **334**(6056), 629–634. <https://doi.org/10.1126/science.1209688>
- Yu, Z.V., Nick G. and Mikhail K.L. (2011). The Future of Metal–Organic Frameworks. *Dalton Transactions*, **40**, 10289–10303. <https://doi.org/10.1039/c1dt11184a>
- Yum, J.H., Walter, P., Huber, S., Rentsch, D., Geiger, T., Nüesch, F., Angelis, F.D. Grätzel, M. and Nazeeruddin. M.K. (2007). Efficient Far Red Sensitization of Nanocrystalline TiO₂ Films by an Unsymmetrical Squaraine Dye. *Journal of American Chemical. Society*, **129**, <https://doi.org/10320-10321e>.
- Zhang, C., Huang, Y., Huo, Z., Chen, S., and Dai, S. (2009). Photoelectrochemical Effects of Guanidinium Thiocyanate on Dye-Sensitized Solar Cell Performance and Stability. *Journal of Physical Chemistry C*, **113**(52), 21779–21783. <https://doi.org/10.1021/jp909732f>
- Zhang, H., Wang, W., Liu, H., Wang, R., Chen, Y. and Wang, Z. (2014). Effects of TiO₂ Film Thickness on Photovoltaic Properties of Dye- Sensitized Solar Cell and its Enhanced Performance by Graphene Combination. *Materials Research Bulletin*, **49**, 126–131. <https://doi.org/10.1016/j.materresbull.2013.08.058>
- Zhao, W., Jun Hou, Y., Song Wang, X., Wen Zhang, B., Cao, Y., Yang, R., Wang, W.B. and Xiao, X.R. (1999). Study on Squarylium Cyanine Dyes for Photoelectric Conversion. *Solar Energy Materials and Solar Cells*, **58**(2), 173–183. [https://doi.org/10.1016/S0927-0248\(98\)00201-3](https://doi.org/10.1016/S0927-0248(98)00201-3)
- Zhao, X., Lin, H., Li, X., and Li, J. (2011). The Application of Freestanding Titanate Nano Fiber Paper for Scattering Layers in Dye-Sensitized Solar Cells. *Materials Letters*, **65**(8), 1157–1160. <https://doi.org/10.1016/j.matlet.2011.01.022>
- Zukalová, M., Zuka, A., Kavan, L., Nazeeruddin, M. K., Liska, P. and Grätzel, M. (2005). Organized Mesoporous TiO₂ Films Exhibiting Greatly Enhanced Performance in Dye-Sensitized Solar Cells. *Nano Letters*, **5**(9), 1789–1792. <https://doi.org/10.1021/nl051401l>
- <https://www.gamry.com/application-notes/EIS/basics-of-electrochemical-impedance-spectroscopy/>

APPENDICES

Publication 1

Surface Review and Letters, Vol. 24, No. 5 (2017) 1750065 (7 pages)
© World Scientific Publishing Company
DOI: 10.1142/S0218625X17500652



EFFECTS OF TiO₂ FILM THICKNESS AND ELECTROLYTE CONCENTRATION ON PHOTOVOLTAIC PERFORMANCE OF DYE-SENSITIZED SOLAR CELL.

D. L. DOMTAU^{*,†,¶}, J. SIMIYU^{*}, E. O. AYIETA^{*}, L. O. NYAKITI^{‡,§},
B. MUTHOKA^{*} and J. M. MWABORA^{*}

^{*}Department of Physics,
University of Nairobi, Nairobi, Kenya

[†]Department of Physics,
University of Jos, Jos, Nigeria

[‡]Marine Engineering and Technology,
Texas A&M University, Galveston, Texas, USA

[§]Material Science and Engineering,
Texas A&M University, College Station, USA

[¶]domtaudinfa@gmail.com

Received 3 August 2016

Revised 3 October 2016

Accepted 19 October 2016

Published 1 December 2016

Effects of film thickness and electrolyte concentration on the photovoltaic performance of TiO₂-based dye-sensitized solar cell (DSSC) were studied. Nanocrystalline anatase TiO₂ thin films with varying thicknesses (3.2–18.9 μm) have been deposited on FTO/glass substrates by screen printing method as work electrodes for DSSC. The prepared samples were characterized by UV-Vis spectroscopy, Atomic Force Microscopy/Scanning Tunneling Microscopy (AFM/STM) and X-ray diffraction (XRD). The optimal thickness of the TiO₂ photoanode is 13.5 μm. Short-circuit photocurrent density (J_{sc}) increases with film thickness due to enlargement of surface area whereas open-circuit voltage decreases with increase in thickness due to increase in electron diffusion length to the electrode. However, the J_{sc} and V_{oc} of DSSC with a film thickness of 18.9 μm (7.5 mA/cm² and 0.687 V) are smaller than those of DSSC with a TiO₂ film thickness of 13.5 μm (9.9 mA/cm² and 0.734 V). This is because the increased thickness of TiO₂ thin film resulted in the decrease in the transmittance of TiO₂ thin films hence reducing the incident light intensity on the N719 dye. Photovoltaic performance also depends greatly on the redox couple concentration in iodide/triiodide. J_{sc} decreases as the redox concentration increases as a result of increased viscosity of the solution which lowers ion mobility. Similarly, V_{oc} decreases as the electrolyte concentration increases due to enhanced back electron transfer reaction. An optimum power conversion efficiency of 4.3% was obtained in a DSSC with the TiO₂ film thickness of 13.5 μm and redox concentration of 0.03 mol dm⁻³ under AM 1.5G illumination at 100 mW/cm².

Keywords: TiO₂ film thickness; electrolyte concentration; photovoltaic performance; dye sensitized solar cell; screen printing.

1750065-1

1. Introduction

TiO₂ films-based dye sensitized solar cells (DSSC) have continued to attract the attention of researchers since the pioneer work of O'Regan and Grätzel was reported in 1991 due to their simple mode of production and low cost comparable to the traditional silicon solar cells.¹⁻⁶ Till date, numerous research groups have been investigating DSSC in order to improve efficiency and stability.^{7,8} A typical DSSC comprises a dye sensitizer, a nanoporous metal oxide film coated on a transparent conductive glass substrate and a counter electrode. Dye molecules are adsorbed on the surface of the semiconductor metal oxide. When light is shun, photons are absorbed by dye molecules which get them excited and hence inject electrons into conduction band of the semiconductor yielding charge separation. Then the electrons migrate to the transparent charge collecting glass substrate, passing through an external connection to the opposite electrode.

The highest conversion efficiency for DSSC which was reported is 13%.⁹ The conversion efficiency is generally affected by factors such as morphology, textures and film thickness of TiO₂,¹⁰⁻¹² counter electrode,¹³ transmittance and conductivity of glass substrate, dye sensitizer and electrolyte solution⁹ among others. TiO₂ film plays a vital role in DSSC among the aforementioned factors. Different methods have been used to deposit TiO₂ thin films on fluorine-doped tin oxide (FTO) glass substrate. These methods include sol-gel method,¹² physical vapor deposition (PDV),¹⁴ chemical vapor method (CVD),¹⁵ liquid phase deposition,¹⁶ spin coating method,¹⁷ doctor blade method^{18,19} and screen printing technique.^{20,21} Of all these methods, screen printing technique remains the most patronized method for industrial preparation of TiO₂ electrodes because it is fast, high precision of film position and thickness control. Film thickness control in screen printing is easily achieved by paste composition and particle size, screen mesh size and number of coatings. Kao *et al.* 2009 reported the effects of film thickness on the performance of DSSC.²² They found J_{sc} and V_{oc} to depend on TiO₂ film thickness prepared by sol-gel method. However, the maximum film thickness was 2 μm which was not thick enough to give its comprehensive effect of the Photovoltaic properties. Zhang *et al.* 2014 also investigated the effects of TiO₂

film thickness on the performance of DSSC.²³ They reported a maximum thickness of 14.5 μm prepared by screen printing method. They found that film thickness had effect on the performance of DSSC. Some investigations have also been reported on the influence of redox species on the interfacial energetics of TiO₂-based DSSC.^{24,25} They reported the effect of I_3^- concentration on short circuit (J_{sc}) and open circuit voltage (V_{oc}) of the DSSC.

In this study, we reported how the variation of TiO₂ film-based photoanode thickness would influence the performance of DSSC and so also the effect of redox couple (I^-/I_3^-) concentration in electrolyte on the photovoltaic properties of DSSC. Screen printing method was used to deposit the TiO₂ films-based electrodes.

2. Experimental Details

2.1. Fabrication of photoanode

Transparent titanium dioxide (T/SP) paste and 2.2 mm thick glass substrate with a 15 Ω/sq FTO coating on one side were purchased from Solaronix. Transparent TiO₂ consists of about 18% wt of anatase particles between 15 nm and 20 nm, terpineol and organic binders. The glass substrates were rinsed in ultrasonic bath with acetone for 15 min, then with ethanol and distilled water and finally dried at 80°C. To study the influence of TiO₂ film thickness on the performance of the cells, the layers of TiO₂ films were varied from 1 to 4 beyond which the films failed to adhere to the substrates. The films were coated by screen printing method using 63T mesh size. Immediately, the TiO₂ film was printed on the FTO/glass, it was kept in dry air for 5 min after which it was transferred to a hot plate at 100°C for 5 min. This was repeated to get more layers for the desired thickness. The prepared films were annealed in a tube furnace at 500°C for 30 min in air. The calcination of the films is to enable the TiO₂ particles blend together for good electrical contact and mechanical adhesion to FTO/glass. As the films cooled down after annealing, they were removed from the furnace at 80°C and dipped in N719 dye solution purchased from Solaronix for 24 h in a sealed staining box. The sensitized films were removed, rinsed in ethanol and kept in dry clean air for 2 h to obtain photoanodes with an active area of 0.48 cm².

2.2. DSSCs assembly

In preparing the counter electrode, a 1 mm hole was drilled in the FTO/glass. The drilled electrodes were cleaned with distilled water, then ethanol for 15 min in an ultrasonic bath. After the contaminants were removed by heating in air for 15 min at 450°C, Pt catalyst was deposited on the drilled FTO/glass by screen printing of the platinum paste (Platisol, Solaronix) and heat treated again at 450°C for 30 min.

TiO₂ photoanodes of different thicknesses and Pt-counter electrodes were assembled in sandwich-type cells and sealed with a 60 μm thick thermoplastic sealing made of Surlyn by heating with a hot plate using mechanical pressure and temperature of 100°C. Iodide/tri-iodide redox electrolyte also purchased from Solaronix was dropped on the hole in the counter electrodes and injected into the cells by vac'n'fill syringe by vacuum backfilling. Finally, the holes in the counter electrodes were sealed using Surlyn and a microscopy cover glass.

Another set of DSSCs were again assembled following the procedure we just described except that the photoanode optimum thickness of 13.5 μm was maintained but redox (I^-/I_3^-) concentration in iodide/tri-iodide electrolyte (Solaronix) was varied as 0.03 mol dm⁻³, 0.1 mol dm⁻³ and 0.15 mol dm⁻³ to study the effect on the photovoltaic performance of the cells.

2.3. Measurement and characterization

The ultraviolet-visible (UV-Vis) transmittance and absorbance spectra of the samples were studied using Shimadzu UV-VIS-NIR Spectrophotometer (Solid-Spec-3700/3700DUV, Japan, Inc.). Film thickness of TiO₂ nanoparticle film was determined using a surface profiler (alpha-step IQ). The crystal structure and average particle size of the TiO₂ films were determined by X-ray diffraction (XRD) with Cu- α irradiation. The surface microstructural features of the films were characterized using scanning electron microscope (SEM). The photovoltaic characteristics of DSSCs were determined using a 500 W xenon lamp science tech solar simulator model SS equipped with a 1.5 AM G filter connected to a Keithley, 2400 model controlled by a computer. The measurement was carried out under 100 mW cm⁻² intensity and the DSSC active area was 0.48 cm².

3. Results and Discussions

SEM image of the TiO₂ film sample annealed at 500°C for 30 min is shown in Fig. 1. The image reveals a film that was crack-free, uniform and smooth on the surface. It also shows that the TiO₂ thin film possesses a nanocrystalline and nanoporous structure which consists of nanoparticles.

Figure 2 shows the XRD patterns of TiO₂ thin film deposited on FTO/glass substrate annealed at 500°C for 30 min. The TiO₂ film shows anatase structure with the preferred (101) orientation. The (101) peaks showed an excellent (101)-axis orientation to the FTO surface. The peaks are narrow and the intensity

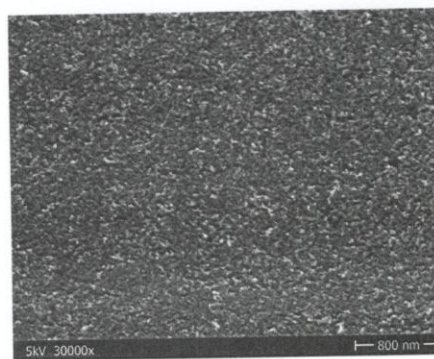


Fig. 1. SEM image of TiO₂ nanoparticle film.

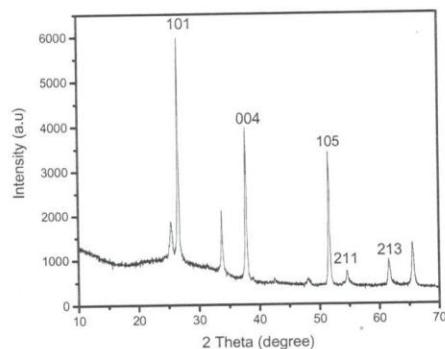


Fig. 2. XRD pattern of the TiO₂ sample annealed at 500°C for 30 min in air.

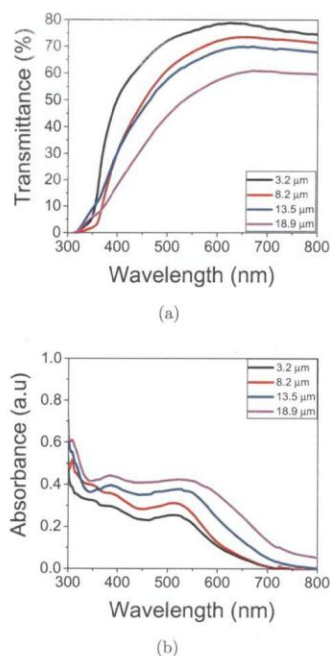


Fig. 3. (Color online) Optical spectra of TiO₂ films with various film thickness. (a) Transmittance and (b) absorbance.

of the films are very strong. The average grain size t was computed from the half-width of the XRD peaks using Scherer's relation:

$$t = \frac{k\lambda}{\beta \cos \theta} \quad (1)$$

where θ is the diffraction angle, λ is the average wavelength of X-ray, k is the shape factor, and β is half-maximum line breadth. 40 nm was obtained as the average grain size.

Figure 3(a) shows the UV-Visible optical transmittance spectra of the TiO₂ films with varying thicknesses (3.2, 8.2, 13.5 and 18.9 μm) between 300 nm and 800 nm in wavelength. It can be deduced that all the films are highly transparent in the visible range and falls rapidly in the UV range with absorption edge at 300 nm. Furthermore, the transmittance of the films becomes lower as the films get thicker. Average transmittance of film of thickness

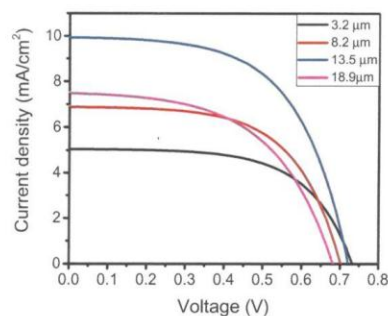


Fig. 4. (Color online) $J-V$ curves as a function of the film thickness of DSSCs under 100 mW/cm² (AM 1.5G) irradiation.

3.2, 8.2, 13.5 and 18.9 μm in the visible range was 79%, 74%, 69% and 60%, respectively. As films become thicker, they become more compact, more light is trapped and hence transmittance becomes lower. Our observations are in agreement with some previous work which reported the transmittance spectra of different films prepared by sol-gel method.^{22,26} These results are also in agreement with our previous investigations.²⁷ The absorbance spectra of the TiO₂ thin films dipped in N719 dye for 24 h are as shown in Fig. 3(b). It can be seen that absorbance increases as the films become thicker. Surface area of films increases with increase in film thickness, and the larger the surface area, the more the anchoring sites for the N719 dye molecules. Therefore, the more the N719 molecules are adsorbed, the more photons of light are absorbed.

Figure 4 shows $J-V$ curves as a function of the film thickness of DSSCs under the intensity of 100 mW cm⁻². Table 1 shows the various photovoltaic parameters of DSSC with different film thicknesses (3.2–18.9 μm) and Fig. 5 shows the dependence of photovoltaic parameters of DSSC on TiO₂ film thickness. We observed from the results that J_{sc} of DSSC increases with increase of the TiO₂ thin film thickness from 3.2 μm to 13.5 μm. The reason is that the thicker the TiO₂ thin film, the higher the adsorption of the N719 dye as seen in Fig. 3(b). The more the dye adsorption, the more the photon absorption, and hence, the more the photocurrent generated. It has been reported that the dye adsorption capacity of TiO₂ thin films are in direct proportion

Table 1. The photovoltaic performances of DSSCs fabricated with different thicknesses of TiO₂ thin films.

Film thickness (μm)	J_{sc} (mA/cm^2)	V_{oc} (V)	FF	η (%)
3.2	5.0	0.731	0.634	2.4
8.2	6.7	0.714	0.630	3.0
13.5	9.9	0.734	0.592	4.3
18.9	7.5	0.6877	0.544	2.8

with the film thickness²⁸ and plays a crucial role in the photovoltaic properties of DSSCs. Therefore, the improved J_{sc} with film thickness could be as a result of enhanced dye loading ability of the TiO₂ films with thicker films. However, the J_{sc} of DSSC with TiO₂ film thickness of 18.9 μm is 7.5 mA/cm^2 which is less than that of DSSC with TiO₂ film thickness of 13.5 μm with J_{sc} of 9.9 mA/cm^2 . This is as a result of the lower transmittance of the TiO₂ thin film with 18.9 μm (as seen in Fig. 3(a)) which reduced the

incident light intensity on the N719 dye. Previous investigations on TiO₂ film thickness effects on Photovoltaic performance have also revealed lower transmittance of thicker films as reason for decrease in J_{sc} .¹² In contrast, due to enhanced dye adsorption with increase in film thickness, more electrons were produced under irradiation, hence the recombination of the photogenerated electrons at the surface of the TiO₂ films with oxidized species such as I_3^- in the electrolyte increased²⁹ resulting in decrease in V_{oc} and FF as the film thickness increases. It is also pertinent to mention that some researchers have reported V_{oc} to increase with increase in film thickness.¹² However, the film thicknesses were in few microns which could be the reason why V_{oc} could still improve with film thickness. Previous investigations also revealed that V_{oc} decreases with increase in TiO₂ film thickness due to the long diffusion of distance for the photoelectron to transport to the electrode, hence improving the probability of recombination.^{30,31}

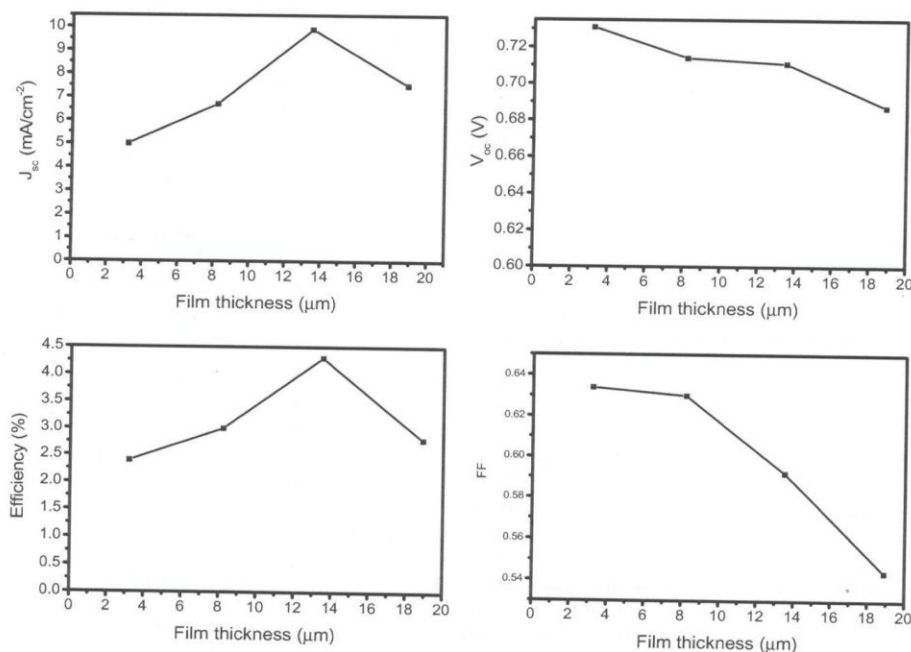


Fig. 5. Dependence of the photovoltaic parameters of DSSC on film thickness.

1750065-5

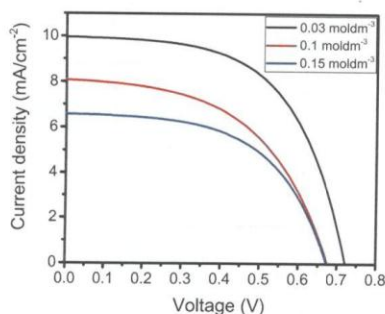


Fig. 6. (Color online) J - V curves of DSSC as a function of redox (I^-/I_3^-) concentration in iodide/tri-iodide electrolyte.

Table 2. Photovoltaic parameters of DSSC as a function of redox (I^-/I_3^-) concentration in iodide/tri-iodide electrolyte.

Redox (I^-/I_3^-) conc.	J_{sc} (mA/cm ²)	V_{oc} (V)	FF	η (%)
0.03 mol dm ⁻³	9.9	0.734	0.592	4.3
0.10 mol dm ⁻³	7.8	0.681	0.553	2.9
0.15 mol dm ⁻³	6.5	0.679	0.578	2.6

Figure 6 shows the J - V curves of DSSC as a function of redox couple concentration. Table 2 is a display of the photovoltaic parameters of the DSSC and Fig. 7 shows the dependence of J_{sc} and V_{oc} of TiO_2 -based DSSC on the I^-/I_3^- concentration in

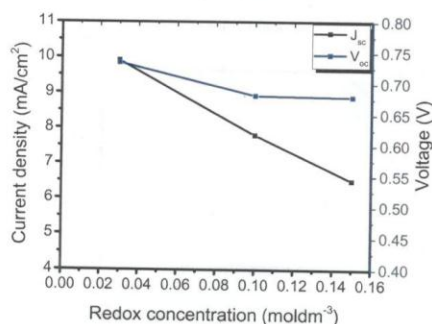
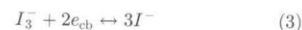


Fig. 7. (Color online) Dependence of J_{sc} and V_{oc} of TiO_2 -based DSSC on the redox (I^-/I_3^-) concentration in iodide/tri-iodide electrolyte.

electrolyte. It can be seen that 0.03 mol dm⁻³ concentration has the highest J_{sc} (9.9 mA cm⁻²). J_{sc} decreased to 7.8 mA cm⁻² and further to 6.5 mA cm⁻² when I^-/I_3^- concentration was increased to 0.1 mol dm⁻³ and 0.15 mol dm⁻³, respectively. The decrease of J_{sc} with increase in redox concentration is because of increase in viscosity of the solution, which reduces ion mobility in the solution, hence the lower J_{sc} . Similarly, V_{oc} decreased from 0.734 V to 0.679 V as the redox concentration increased from 0.03 mol dm⁻³ to 0.15 mol dm⁻³, respectively. V_{oc} for DSSC with an iodine redox electrolyte is given as

$$V_{oc} = \frac{kT}{e} \ln \left(\frac{I_{inj}}{n_{cb} k_{et} I_3^-} \right), \quad (2)$$

where I_{inj} is injection current from dye to semiconductor, n_{cb} electron density on the conduction band of semiconductor, and k_{et} is the rate constant of reduction of I_3^- to I^- (back electron transfer reaction as in Eq. (2))²⁵



As seen in Eq. (1) above, V_{oc} decreases as back electron transfer increases. Therefore, the decrease in V_{oc} with increase in I^-/I_3^- concentration is due to the enhanced back electron transfer reaction.²³ This shows that 0.03 mol dm⁻³ is the maximum optimum redox concentration for an iodide/triiodide electrolyte.

4. Conclusions

In summary, TiO_2 nanoparticles were deposited on FTO/glass by screen printing method. The TiO_2 films were found to be anatase, uniform and crack-free at the surface. The thicknesses of the films were determined as 3.2, 8.2, 13.5 and 18.9 μ m. The films were highly transparent and transmittance was found to become lower as the films become thicker. On the other hand, absorbance increases with increase in film thickness. This is because the thicker the films, the larger the surface area and hence the more anchoring sites for dye molecules. Photovoltaic performance of TiO_2 based dye sensitized solar cell depends greatly on the film thickness. It was observed that as the film thickness increases, the J_{sc} increases and subsequently decreases. J_{sc} increases with increase in film thickness due to enhanced dye adsorption as evident in absorbance spectra. The decrease in J_{sc} with further increase

in film thickness is as a result of low transmittance in thicker film which reduces the light intensity on the dye adsorbed semiconductor. The optimum film thickness obtained was 13.5 μm . V_{oc} and FF decreased consistently with increase in film thickness. It was also found that photovoltaic performance also greatly depends on the redox concentration. Both J_{sc} and V_{oc} decrease with increase in electrolyte concentration. The reduction in J_{sc} is as a result of the rise in viscosity of the electrolyte solution while decrease in V_{oc} is due to back electron transfer reaction. 0.3 mol dm⁻³ was found to be the optimum redox electrolyte concentration with cell efficiency of 4.3% at the optimum film thickness of 13.5 μm .

References

1. B. C. O'Regan and M. Grätzel, *Nature* **353** (1991) 737.
2. M. Grätzel, *Nature* **414** (2001) 338.
3. P. Ramasamy, M. Kang, H. Cha and J. Kim, *Mater. Res. Bull.* **48** (2013) 79.
4. S. K. Park, C. Chung, D. Kim, C. Kim, S. Lee and Y. S. Han, *Mater. Res. Bull.* **47** (2012) 2722.
5. L. Zhao, J. G. Yu, J. J. Fan, P. C. Zhai and S. M. Wang, *Electrochem. Commun.* **11** (2009) 2052.
6. N. Mir and M. Salavati-Niasari, *Mater. Res. Bull.* **48** (2013) 1660.
7. E. Guillén, F. Casanueva, J. A. Anta, A. Vega, G. Oskam, R. Alcántara, C. Fernández and J. M. Calleja, *J. Photochem. Photobiol. A: Chem.* **200** (2008) 364.
8. C. C. Ting and W. S. Chao, *Measurement* **43** (2010) 1623.
9. A. Yella, H. Lee, H. N. Tsao, C. Yi, A. K. Chandiran, M. Nazeeruddin, E. W. Diau, C. Yeh, S. M. Zakeeruddin and M. Grätzel, *Science* **334** (2011) 629.
10. H. Wang, Y. Liu, H. Huang, M. Zhong, H. Shen, Y. Wang and H. Yang, *Appl. Surf. Sci.* **255** (2009) 9020.
11. J. G. Yu, J. J. Fan and B. Cheng, *J. Power Sources* **196** (2011) 7891.
12. M. C. Kao, H. Z. Chen, S. L. Young, C. Y. Kung and C. C. Lin, *Thin Solid Films* **517** (2009) 5096.
13. W. J. Lee, E. Ramasamy, D. Y. Lee and J. S. Song, *Sol. Energy Mater. Sol. Cells* **92** (2008) 814.
14. S. C. Yang, D. J. Yang, J. Kim, J. M. Hong, H. G. Kim, I. D. Kim and H. Lee, *Adv. Mater.* **20** (2008) 1059.
15. J. P. Lu, J. Wang and R. Raj, *Thin Solid Films* **204** (1991) 13.
16. S. Nishimura, N. Abrams, B. A. Lewis, L. I. Halaoui, T. E. Mallouk, K. D. Benkstein, J. van de Lagemaat and A. J. Frank, *Am. J. Chem. Soc.* **125** (2003) 6306.
17. J. G. Lee, J. H. Cheon, H. S. Yang, D. K. Lee and J. H. Kim, *J. Nanosci. Nanotech.* **12** (2012) 6026.
18. J. G. Yu, Q. L. Li, J. J. Fan and B. Cheng, *Chem. Commun.* **47** (2011) 9161.
19. J. Li, L. Zhao, S. M. Wang, J. H. Hu, B. H. Dong, H. B. Lu, L. Wan and P. Wang, *Mater. Res. Bull.* **48** (2013) 2566.
20. T. Charinpanitkul, P. Lorturn, W. Ratismith, N. Viriya-empikul, G. Tumcharern and J. Wilcox, *Mater. Res. Bull.* **46** (2011) 1604.
21. S. Ito, P. Chen, P. Comte, M. K. Nazeeruddin, P. Liska, P. Pechy and M. Grätzel, *Prog. Photovoltaics* **15** (2007) 603.
22. M. C. Kao, H. Z. Chen, S. L. Young, C. Y. Kung and C. C. Lin, *Thin Solid Films* **517** (2009) 5096.
23. H. Zhang, W. Wang, H. Liu, R. Wang, Y. Chen and Z. Wang, *Mater. Res. Bull.* **49** (2014) 126.
24. Y. Liu, A. Hagfeldt, X.-R. Xiao and S.-E. Lindquist, *Sol. Energy Mater. Sol. Cells* **55** (1998) 267.
25. K. Hara, T. Horiguchi, T. Kinoshita, K. Sayama and H. Arakawa, *Sol. Energy Mater. Sol. Cells* **70** (2001) 151.
26. P. Malliga, J. Pandiarajan, N. Prithivikumaran and K. Neyvasagam, *J. Appl. Phys.* **6** (2014) 22.
27. D. L. Domtau, J. Simiyu, E. O. Ayieta, B. Muthoka and J. M. Mwabora, *J. Mater. Phys. Chem.* **4** (2016) 1.
28. Z. S. Wang, H. Kawauchi, T. Kashima and H. Arakawa, *Coord. Chem. Rev.* **248** (2004) 1381.
29. M. K. Nazeeruddin, A. Kay, I. Rodicio, R. Humphry-Barker, E. Mueller, P. Liska, N. Vlachopoulos and M. Grätzel, *J. Am. Chem. Soc.* **115** (1993) 6382.
30. J. K. Tsai, W. D. Hsu, T. C. Wu, T. H. Meen and W. J. Chong, *Nanoscale Res. Lett.* **8** (2013) 459.
31. R. Escalante, R. G. Rodriguez, B. E. H. Cervera, M. A. A. Frutis, N. G. Ortiz, J. V. Cab and G. Oskam, *Energy Environ. Focus* **2** (2013) 280.

Research Article

Influence of Pore Size on the Optical and Electrical Properties of Screen Printed TiO₂ Thin Films

Dinfa Luka Domtau,^{1,2} Justus Simiyu,¹ Elijah Omollo Ayieta,¹
Godwin Mwebeze Asimwe,¹ and Julius Mwakondo Mwabora¹

¹Department of Physics, University of Nairobi, Nairobi, Kenya

²Department of Physics, University of Jos, Jos, Nigeria

Correspondence should be addressed to Dinfa Luka Domtau; domtaudinfa@gmail.com

Received 8 July 2016; Revised 24 August 2016; Accepted 5 September 2016

Academic Editor: Kaveh Edalati

Copyright © 2016 Dinfa Luka Domtau et al. This is an open access article distributed under the Creative Commons Attribution License, which permits unrestricted use, distribution, and reproduction in any medium, provided the original work is properly cited.

Influence of pore size on the optical and electrical properties of TiO₂ thin films was studied. TiO₂ thin films with different weight percentages (wt%) of carbon black were deposited by screen printing method on fluorine doped tin oxide (FTO) coated on glass substrate. Carbon black decomposed on annealing and artificial pores were created in the films. All the films were 3.2 μm thick as measured by a surface profiler. UV-VIS-NIR spectrophotometer was used to study transmittance and reflectance spectra of the films in the photon wavelength of 300–900 nm while absorbance was studied in the range of 350–900 nm. Band gaps and refractive index of the films were studied using the spectra. Reflectance, absorbance, and refractive index were found to increase with concentrations of carbon black. There was no significant variation in band gaps of films with change in carbon black concentrations. Transmittance reduced as the concentration of carbon black in TiO₂ increased (i.e., increase in pore size). Currents and voltages (*I-V*) characteristics of the films were measured by a 4-point probe. Resistivity (ρ) and conductivity (σ) of the films were computed from the *I-V* values. It was observed that resistivity increased with carbon black concentrations while conductivity decreased as the pore size of the films increased.

1. Introduction

The interest of material scientists in titanium dioxide is on the increase due to its potentials in a wide range of industrial applications. TiO₂ with a wide band gap of 3.2 eV has attracted considerable interest because of the outstanding properties of its thin films such as electrical, optical, and chemical properties. These properties include high conductivity, high refractive index, and high transparency in the visible region. Thus TiO₂ is useful in applications such as photocatalyst [1], dye sensitized solar cells [2], chemical sensors [3–5], electrochromics [6], and electronic devices [7].

The quality of the TiO₂ film is influenced by the type of material and method used for film deposition and subsequent sintering procedure. The properties of the films such as surface area, roughness, and pore size and film thickness are responsible for its surface and electronic properties. Cho et al.

presented a simple architecture that achieves enhanced light scattering in TiO₂ films [8]. Polystyrene (PS) spheres of submicrometer size were incorporated into the TiO₂ paste resulting in photoanode with bimodal pore size distribution. The optical properties of the films were improved by the enhancement of the films' pore size. Furthermore, TiO₂ films with artificial pores formed using acetylene black to improve the light scattering films without a light scattering layer have also been fabricated [9]. The artificial films were found to improve the reflectance of the films. The dependence of optical properties of TiO₂ thin films has been reported to depend on pore size [10, 11]. Refractive index and electrical resistivity were found to depend on porosity of the films and bandgap was found to depend on annealing temperature and grain size. However, the effect of pore size on the optical and electrical properties of TiO₂ thin films especially for optimum applications in dye sensitized solar cells has not

been adequately explored. It has been reported that the substrate temperature [12–14], deposition rate [15, 16], and film thickness have important effects on the morphology and nanostructure of thin films. TiO₂ thin films have been deposited by various techniques: these include tape casting [17], screen printing [18–20], and electrophoretic deposition [21]. Of all the aforementioned, screen printing technique is simple, of low cost, and easily reproducible.

In this work, we created some size-varying artificial pores in TiO₂ thin films. This work seeks to provide information on the optical and electrical properties of pore size enhanced TiO₂ films that may find optimum applications in dye sensitized solar cells. We simply mixed carbon black powder with TiO₂ paste and deposited onto glass by screen printing method. The carbon black simply decomposed on annealing leaving behind voids in the films.

2. Experimental Details

The TiO₂ thin films were prepared using screen printing method as follows: commercially available TiO₂ paste purchased from Solaronix (Ti-Nanoxide T/SP) was used as original and control paste, into which varying weight percentages of carbon black would be added. TiO₂ anatase concentration is 18 wt%; particle size is of 18–20 nm and transparent. The carbon black powder was purchased from Alfa Aesar (acetylene, 100% compressed). 2 mm thick glass substrates with 15 Ω/sq. fluorine doped tin oxide (FTO) coating on one side purchased from Solaronix were ultrasonically cleaned in distilled water for 20 minutes, dipped in acetone for 20 minutes, and finally rinsed in distilled water.

Ti-Nanoxide T/SP was diluted in absolute ethanol and mixed with a magnetic stirrer bar for 30 minutes. Different weight percentages (0.5, 1, 1.5, 2, and 3 wt%) were added to the suspension. The suspension was dispersed with a sonication horn (digital Sonifier 450) to break any aggregates of nanoparticles. It was sonicated in pulses (2 s ON, 2 s OFF) to avoid temperature elevation for 30 minutes in intervals of 6 minutes and stirred for 5 minutes at each interval. The mixture was then transferred to a rotary evaporator at 80°C, 100 mbar. The paste was again homogenized by a grinder after the ethanol was evaporated. The mixture of TiO₂ paste and carbon black of different weight percentages of carbon black was coated (by screen printing method) one time each onto FTO/glass using a 63 T mesh. All the films were sintered in tube furnace at 500°C for 30 minutes in air. At this temperature, carbon black was completely burnt out leaving behind voids in the films.

The surface microstructural features of the films were characterized using Multimode 8-HR Atomic Force Microscopy/Scanning Tunneling Microscopy (AFM/STM) in tapping mode. Optical transmittance, reflectance, and absorbance spectra of TiO₂ thin films were studied using Shimadzu UV-VIS-NIR Spectrophotometer (SolidSpec-3700/3700DUV, Japan, Inc.) Film thickness was measured by a surface profiler (alpha-step IQ). Sheet resistances of the films were measured by Jandel RM3-AR 4-Point Probe.

3. Results and Discussions

The TiO₂ thin films prepared were incorporated with 0, 0.5, 1, 1.5, 2, and 3 wt% of carbon black. All the films were 3.2 μm of thickness to restrict the influence of film thickness on the samples. Figures 1(a), 1(b), 1(c), 1(d), 1(e), and 1(f) show the dependence of pore size on carbon black concentrations. Figures 1(a), 1(b), 1(c), 1(d), 1(e), and 1(f) were incorporated with 0, 0.5, 1, 1.5, 2, and 3 wt% of carbon black. It was observed that the higher the wt% of carbon black incorporated into the TiO₂ films the larger the sizes of voids left behind after the combustion of the carbon black. We also found that, beyond 3 wt%, carbon black does not burn out at the annealing temperature of 500°C. That is to say with any further addition of carbon with annealing temperature remaining the same, TiO₂ films will be contaminated; thus purity will be compromised.

Transmittance spectra of the films are as shown in Figure 2. 0 wt% TiO₂ thin film showed high transparency in the visible region and decreased sharply at the UV region but dropped steadily towards the NIR. The transmittance spectra have the highest value of 79%. It was observed that as the weight percentage of carbon black increased (i.e., as the pore size increased), the transmittance decreased. The film with the highest weight percentage of carbon black was the least transparent (39%). We observed that transmittance spectra in samples 2 wt% and 3 wt% dropped drastically as compared to other samples. Though the pore size in these samples also increased which resulted in drop in transmittance, the drastic drop could be due to residue of carbon black left behind. At such concentrations, 500°C is not sufficient to completely burn out carbon black; hence residue is responsible for light blockage.

Figure 3 shows the reflectance spectra of TiO₂ thin films with different weight percentages of carbon black. It was observed that reflectance increased with pore size. The increase in reflectance is a result of multiple light scattering by the pores created [9]. Otherwise, it also accounts for the decrease in the films transmittance as the pores increased.

Figure 4 shows absorbance spectra of TiO₂ thin films with varying weight percentages of carbon black. The absorption edge of TiO₂ as seen in Figure 3 is 300 nm. The step observed at 720 nm is a result of the change in detectors of the spectrophotometer. As the pores increased, absorbance increased due to increase in optical path length, optical light confinement, or light trapping [9]. The 0 wt% TiO₂ thin film has the least absorbance and film with the highest carbon black concentration has the highest absorbance. Our observations are in agreement with some previous investigations [8, 9].

From interband absorption theory, the optical band gap of TiO₂ films can be determined from the formula [22]

$$(\alpha h\nu)^m = A(h\nu - E_g), \quad (1)$$

where α is the absorption coefficient, A is a constant, $h\nu$ is photon energy (eV), and m is the transition coefficient. $m = 1/2$ and $3/2$ corresponds to direct allowed and direct forbidden transitions and $m = 2, 3$ corresponds to indirect

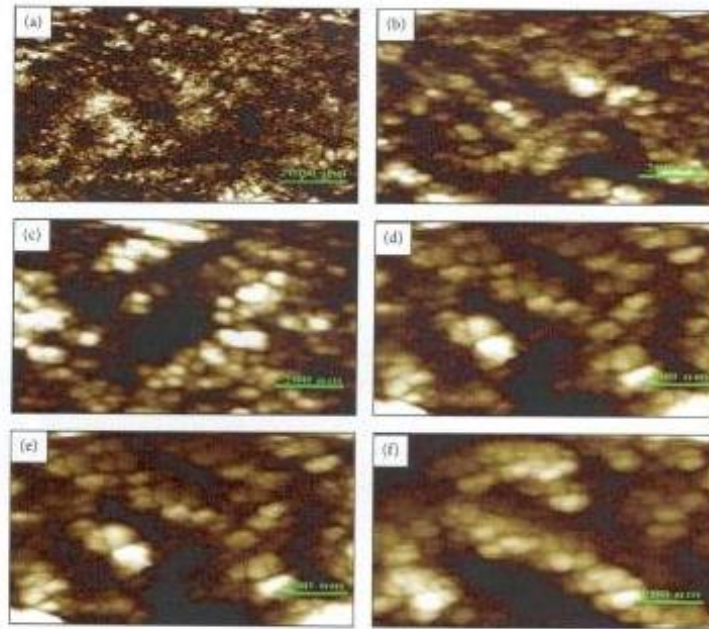


FIGURE 1: AFM/STM images of TiO₂ film with different wt% of carbon black.

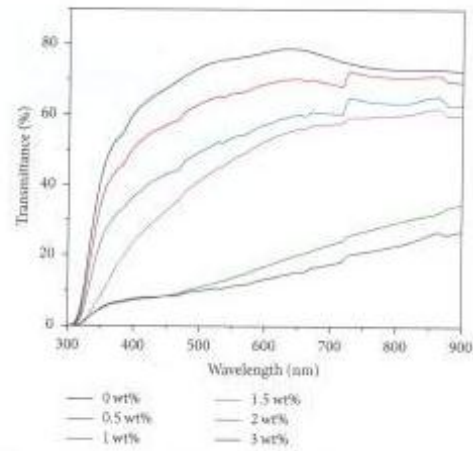


FIGURE 2: Transmittance spectra of TiO₂ thin films with different wt% of carbon black.

allowed and indirect forbidden transitions, respectively [22]. The absorption coefficient is thus calculated from the relation

$$\alpha = \frac{1}{d} \ln \left(\frac{1}{T} \right), \quad (2)$$

where d is the film thickness and T the transmittance of the film at each wavelength.

The optical band gaps were obtained from plotting Tauc's equation using $1/2$ for m and extrapolating the straight line part of the curve to $(\alpha h\nu)^{1/m} = 0$. It was observed that for all

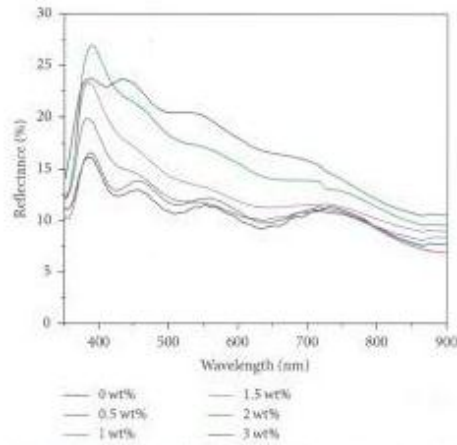


FIGURE 3: Reflectance spectra of TiO_2 thin films with varying wt% of carbon black.

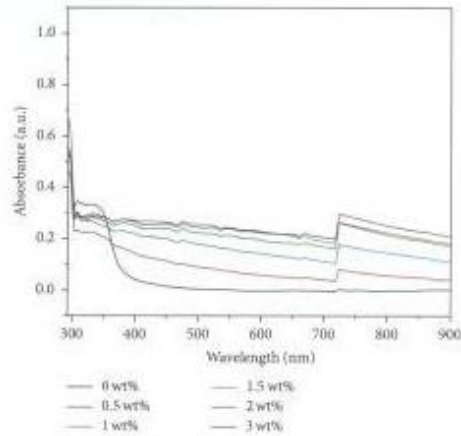


FIGURE 4: Absorbance of TiO_2 thin films with different wt% of carbon black.

the films, the best straight line is obtained for the value of m equal to $1/2$, which is typical of direct allowed transitions [22].

Figure 5 shows the band gaps of TiO_2 thin films with different weight percentages of carbon. We observed that pore size had no effect on band gaps as all the films despite their variations in pore size have a band gap of ≈ 3.8 eV.

The refractive index was computed using the relation [23]

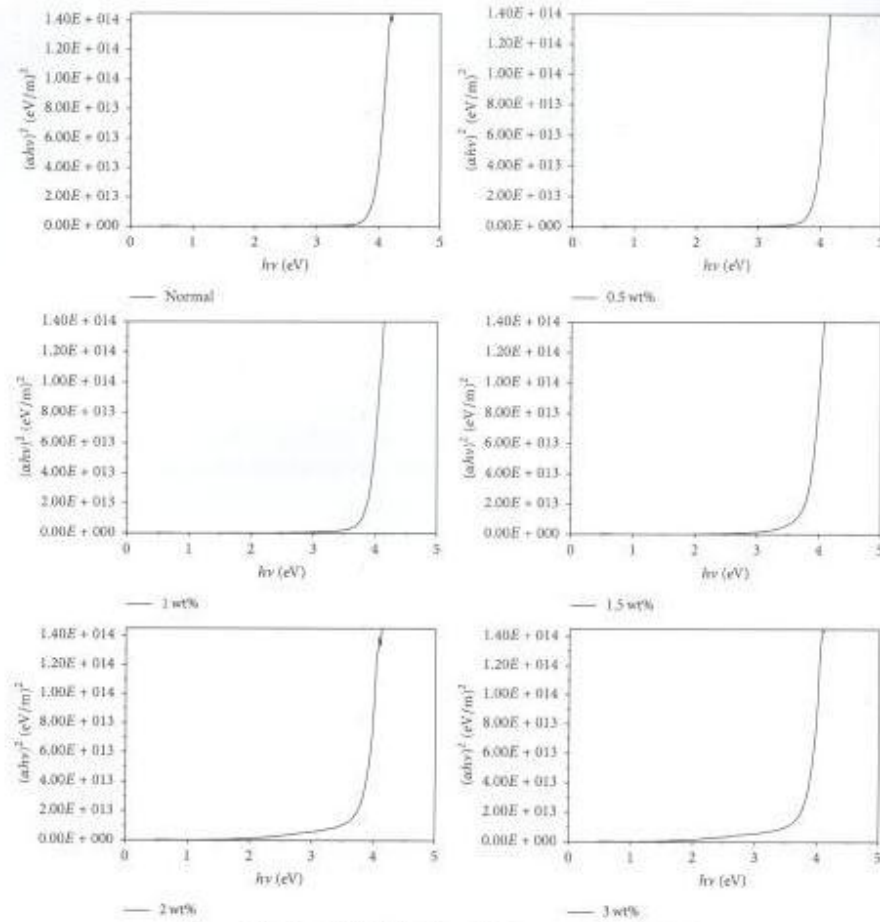
$$n = \frac{1+R}{1-R} + \left[\frac{4R}{(1-R)^2} - K^2 \right]^{1/2}, \quad (3)$$

where n is refractive index, R is reflectance, λ is wavelength, and K is the extinction coefficient given as

$$K = \frac{\alpha\lambda}{4\pi}. \quad (4)$$

The refractive indices of TiO_2 thin films of different wt% were obtained from (3) and plotted in Figure 6.

Figure 6 shows that refractive index increased with increase in pore size. 0 wt% TiO_2 film has the least refractive index within the visible range. Any other film with artificial pores has refractive index higher than the 0 wt% film and

FIGURE 5: Band gap of TiO₂ thin films with different wt% of carbon black.

that was how refractive index kept rising with increase in pore size. This is due to the fact that the increase in pore size increases light scattering and delay in light path or light trapping [9]. Refractive index increased from 1.4 (0 wt% TiO₂) to 1.8 (2 wt%) as the pore size increased. It shows that pore size truly has influence on the refractive index of TiO₂.

From the measured $I-V$ by a 4-point probe, electrical resistivity was calculated using the following equation since they are thin film samples:

$$\rho = \frac{\pi}{\ln 2} \frac{v}{I} \times \text{thickness}, \quad (5)$$

where ρ is resistivity, v is voltage, I is current, and $\pi/\ln 2 = 4.53$.

TABLE 1: Resistivity and conductivity of TiO₂ thin films with varying wt% of carbon black.

Weight ratio (%)	Resistivity ($\Omega\text{-cm}$)	Conductivity (Siemens $\cdot\text{cm}^{-2}$)
0.5	2.60×10^{-3}	384.61
1.0	2.84×10^{-3}	352.11
1.5	9.67×10^{-3}	103.41
2.0	19.08×10^{-3}	52.41
3.0	28.33×10^{-3}	35.29

The results are tabulated in Table 1.

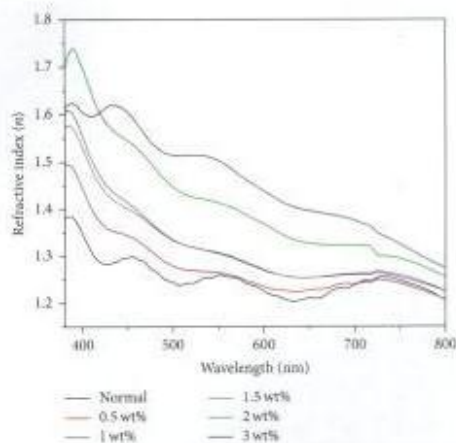


FIGURE 6: Refractive index of TiO_2 thin films with different wt% of carbon black.

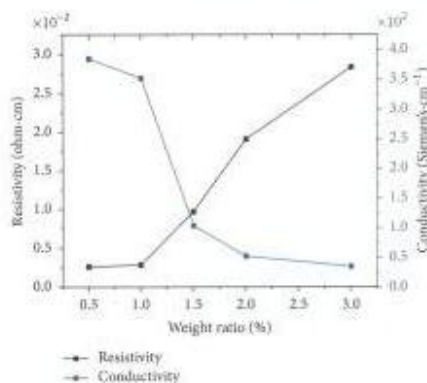


FIGURE 7: Resistivity and conductivity of TiO_2 thin films with different wt% of carbon black.

We found that resistivity decreased with increase in weight concentrations of carbon black.

Conductivity of TiO_2 thin films is the inverse of resistivity. Resistivity and conductivity are given by the relation

$$\sigma = \frac{1}{\rho} \quad (6)$$

where σ is conductivity. The values for conductivity are also tabulated in Table I. Figure 7 shows the resistivity and conductivity of TiO_2 thin films with different wt% of carbon black.

It was observed that conductivity decreased with increase in concentrations of carbon black. This is because the increase

in pore size reduces the electronic contact between TiO_2 particles. So, also as the electronic contacts between the molecules reduce, resistivity increases; hence the observation is shown in Figure 7. Resistivity increased from $2.6 \times 10^{-5} \Omega\text{-cm}$ to $28.3 \times 10^{-3} \Omega\text{-cm}$ while conductivity decreased from $384.61 \text{ Siemens}\cdot\text{cm}^{-1}$ to $35.29 \text{ Siemens}\cdot\text{cm}^{-1}$ as the pore size increased.

4. Conclusion

Titanium oxide thin films of $3.2 \mu\text{m}$ thickness (with and without) different wt% of carbon black were deposited on FTO/glass and then subjected to an annealing temperature of 500°C for 30 minutes. Carbon black was completely burnt out at this temperature and artificial pores were created. Pore size effect on the optical and electrical properties of the films were investigated. UV-VIS studies revealed that normal TiO_2 thin film is highly transparent in the visible region with a value of 79%. Transmittance decreased with increase in pore size while reflectance and absorbance increased as the pore size becomes larger. Refractive indices of the films also increased with increase in pore size of the films. However the band gap as calculated from the transmittance spectra remained constant with change in films' pore size. We also found that resistivity rose from $2.6 \times 10^{-5} \Omega\text{-cm}$ to $28.3 \times 10^{-3} \Omega\text{-cm}$ and conductivity dropped from $384.61 \text{ Siemens}\cdot\text{cm}^{-1}$ to $35.29 \text{ Siemens}\cdot\text{cm}^{-1}$ as pore size increased. These films will find useful applications in dye sensitized solar cells because of their increased light scattering ability and their high transmittance in the visible region. The high refractive index in the visible region is also important in solar cell applications. Pores created will also serve as good anchoring sites for dye molecules, thereby enhancing higher photocurrent generation. The relatively high conductivity of these films will also make them suitable for solar cells applications.

Competing Interests

The authors declare that they have no competing interests.

References

- [1] A. L. Linsebigler, G. Lu, and J. T. Yates Jr., "Photocatalysis on TiO_2 surfaces: principles, mechanisms, and selected results," *Chemical Reviews*, vol. 95, no. 3, pp. 735–758, 1995.
- [2] U. Bach, D. Lupo, P. Comte et al., "Solid-state dye-sensitized mesoporous TiO_2 solar cells with high photon-to-electron conversion efficiencies," *Nature*, vol. 395, no. 6702, pp. 583–585, 1998.
- [3] L. R. Skubal, N. K. Meshkov, and M. C. Vogt, "Detection and identification of gaseous organics using a TiO_2 sensor," *Journal of Photochemistry and Photobiology A: Chemistry*, vol. 148, no. 1–3, pp. 103–108, 2002.
- [4] S.-A. Gao, A.-P. Xian, L.-H. Cao, R.-C. Xie, and J.-K. Shang, "Influence of calcining temperature on photoresponse of TiO_2 film under nitrogen and oxygen in room temperature," *Sensors and Actuators B: Chemical*, vol. 134, no. 2, pp. 718–726, 2008.

- [5] D. Mardare, N. Ifimie, and D. Luca, "TiO₂ thin films as sensing gas materials," *Journal of Non-Crystalline Solids*, vol. 354, no. 35-39, pp. 4396-4400, 2008.
- [6] N. N. Dinh, N. Th. T. Oanh, P. D. Long, M. C. Bernard, and A. Hugot-Le Goff, "Electrochromic properties of TiO₂ anatase thin films prepared by a dipping sol-gel method," *Thin Solid Films*, vol. 423, no. 1, pp. 70-76, 2003.
- [7] N. Zhong, H. Shima, and H. Akinaga, "Mechanisms of the performance improvement of TiO_{2-x} based field-effect transistor using SiO₂ as gate insulator," *AIP Advances*, vol. 1, Article ID 032167, 8 pages, 2011.
- [8] T.-Y. Cho, C.-W. Han, Y. Jun, and S.-G. Yoon, "Formation of artificial pores in nano-TiO₂ photo-electrode films using acetylene-black for high-efficiency, dye-sensitized solar cells," *Scientific Reports*, vol. 3, article 1496, 2013.
- [9] T. Pham, T. Bessho, N. Mathews et al., "Light scattering enhancement from sub-micrometer cavities in the photoanode for dye-sensitized solar cells," *Journal of Materials Chemistry*, vol. 22, no. 32, pp. 16201-16204, 2012.
- [10] M. Bartic, I. Sacarescu, and V. Harabagiu, "Optical and electrical properties of TiO₂ thin films deposited by sol-gel method," *Revue Roumaine de Chimie*, vol. 58, no. 2-3, pp. 105-111, 2013.
- [11] F. Hanini, A. Bouabellou, Y. Bouachiba et al., "Structural, optical and electrical properties of TiO₂ thin films synthesized by sol-gel technique," *Journal of Engineering*, vol. 3, no. 11, pp. 21-28, 2013.
- [12] T. Ida and H. Toraya, "Deconvolution of the instrumental functions in powder X-ray diffractometry," *Journal of Applied Crystallography*, vol. 35, no. 1, pp. 58-68, 2002.
- [13] M. Cernanský, "Some practical aspects of the Fourier deconvolution," *Journal of Applied Crystallography*, vol. 16, pp. 103-112, 1983.
- [14] R. W. Cheary and A. Coelho, "Thin film analysis by X-ray scattering," *Journal of Applied Crystallography*, vol. 25, pp. 109-121, 1992.
- [15] S. A. Howard and R. L. Snyder, "X-ray characterization of materials," *Journal of Applied Crystallography*, vol. 22, pp. 238-243, 1989.
- [16] S. Enzo, G. Fagherazzi, A. Benedetti, and S. Polizzi, "A profile-fitting procedure for analysis of broadened X-ray diffraction peaks. I. methodology," *Journal of Applied Crystallography*, vol. 21, no. 5, pp. 536-542, 1988.
- [17] M. K. Nazeeruddin, A. Kay, I. Rodicio et al., "Conversion of light to electricity by cis-X2bis(2,2'-bipyridyl)-4,4'-dicarboxylate)ruthenium(II) charge-transfer sensitizers (X = Cl-, Br-, I-, CN-, and SCN-) on nanocrystalline titanium dioxide electrodes," *Journal of the American Chemical Society*, vol. 115, no. 14, pp. 6382-6390, 1993.
- [18] D. S. Tsoukleris and I. M. Arabatzis, "Environmental applications of solar energy," *Solar Energy*, vol. 79, pp. 422-430, 2005.
- [19] L. Ma, M. Liu, T. Peng, K. Fan, L. Lu, and K. Dai, "Fabrication and properties of meso-macroporous electrodes screen-printed from mesoporous titania nanoparticles for dye-sensitized solar cells," *Materials Chemistry and Physics*, vol. 118, pp. 477-483, 2009.
- [20] K. Fan, M. Liu, T. Peng, L. Ma, and K. Dai, "Effects of paste components on the properties of screen-printed porous TiO₂ film for dye-sensitized solar cells," *Renewable Energy*, vol. 35, no. 2, pp. 555-561, 2010.
- [21] T. Miyasaka, Y. Kijitori, T. N. Murakami, M. Kimura, and S. Uegusa, "Efficient nonsintering type dye-sensitized photocells based on electrophoretically deposited TiO₂ layers," *Chemistry Letters*, vol. 31, no. 12, pp. 1250-1251, 2002.
- [22] C. Kittel, *Introduction to Solid State Physics*, John Wiley and Sons, New York, NY, USA, 7th edition, 1996.
- [23] Q. Y. Cai, Y. Zheng, P. Mao et al., "Evolution of optical constants of silicon dioxide on silicon from ultrathin films to thick films," *Journal of Physics D: Applied Physics*, vol. 43, no. 44, Article ID 445302, 2010.

Optical and Electrical Properties Dependence on Thickness of Screen-Printed TiO₂ Thin Films

D.L. Domtau^{1,2*}, J. Simiyu¹, E.O. Ayieta¹, B. Muthoka¹, J. M. Mwabora¹

¹Department of Physics, University of Nairobi, Nairobi, Kenya

²Department of Physics, University of Jos, Jos, Nigeria

*Corresponding author: domtaudinf@gmail.com

Abstract Effect of film thickness on the optical and electrical properties of TiO₂ thin films were studied. Thin films of different thicknesses were deposited by screen printing method on fluorine doped tin oxide coated on glass substrate. The film thickness was determined by surface profile measurement. The thicknesses were 3.2, 8.2, 13.5 and 18.9 μm. Transmittance, reflectance and absorbance spectra were studied using UV-VIS-NIR spectrophotometer in the photon wavelength range of 300-1500 nm for transmittance and reflectance and 350-1200 nm for absorbance. Band gap and refractive index of the films were determined using these spectra. It was found that reflectance, absorbance, band gap and refractive index increased with film thickness while transmittance decreased with increase in thickness. I-V characteristics of the films were also measured by a 4-point probe. Electrical resistivity (ρ) and conductivity (σ) were calculated from the I-V values. Resistivity was found to increase with thickness while conductivity decreased with increase in film thickness.

Keywords: TiO₂ thin films, thickness, optical and electrical properties, screen printing

Cite This Article: D.L. Domtau, J. Simiyu, E.O. Ayieta, B. Muthoka, and J. M. Mwabora, "Optical and Electrical Properties Dependence on Thickness of Screen-Printed TiO₂ Thin Films." *Journal of Materials Physics and Chemistry*, vol. 4, no. 1 (2016): 1-3. doi: 10.12691/jmpc-4-1-1.

1. Introduction

Transparent conducting oxide (TCO) materials have greatly drawn the attention of material scientists as a result of their diverse industrial applications. Among these materials, TiO₂ remains the most promising in a number of research areas for its availability, chemical and physical stability, non-toxicity, high refractive index, efficient photo catalytic activity and low cost [1,2]. TiO₂ is a wide band gap semiconductor material which has been under far-reaching investigations due to its applications in diverse research fields namely dye sensitized solar cells [3] gas sensors [4] photo catalysts [5,6] wave guiding [7] antireflective coatings [8], dielectric [9] etc. Investigations have revealed that the optical performance of thin films can be strongly affected by film thickness [10,11]. There have been so many experimental reports on the dependence of optical properties for TiO₂ film [12,13,14,15], but not much has been reported on TiO₂ screen printed thin films and their optical and electrical properties dependence on film thickness.

In this study, we shall report the effect of film thickness on optical and electrical properties of TiO₂ thin films deposited by screen printing method.

2. Experimental Details

Thin films of TiO₂ were deposited from commercially available TiO₂ paste (Ti-Nanoxide T/SP) purchased from Solaronix. TiO₂ anatase concentration is 18wt%, particle

size of 18-20nm and transparent. 2.2mm thick glass substrates with 15Ω/sq fluorine doped tin oxide (FTO) coating on one side were ultrasonically cleaned in distilled water for 15 minutes, dipped in acetone for 15 minutes and finally rinsed in distilled water. TiO₂ films of 3.2, 8.2, 13.5 and 18.9 μm thickness were coated onto FTO/glass by screen printing method. The films were annealed at 500 °C for 30 minutes in a tube furnace. Optical transmittance, reflectance and absorbance spectra of TiO₂ thin films were studied using Shimadzu UV-VIS-NIR Spectrophotometer (SolidSpec-3700/3700DUV, Japan, Inc.) Film thickness was measured by a surface profiler (alpha-step IQ). Sheet resistance of the films were measured by Jandel RM3-AR 4-Point Probe.

3. Results and Discussions

The optical properties of TiO₂ screen printed films were found to be affected by the film thickness. The samples showed high transparency in the visible region and a sharp fall in the UV. Transmittance spectra as shown in Figure 1 (a) decreased with increase in film thickness. This is in agreement with some previous investigations [16]. It has an average value of 78% for the thickest film and an average value of 62% for thinnest film. Figure 1 (b) shows that reflectance increased with film thickness. The thickest film has the maximum reflectance and thinnest film has the least reflectance. All the films have their maximum transmittance and reflectance at the wavelength of about 400nm. Figure 1 (c) shows a generally low absorbance in all the films but there is still a dependence.

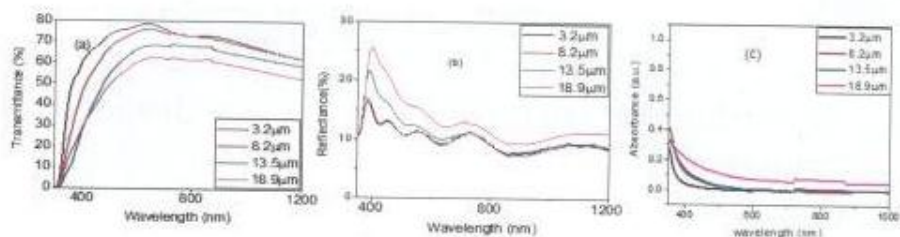


Figure 1. Transmittance, reflectance and absorbance spectra of TiO_2 films variation with film thickness

We found absorbance to increase with film thickness. All these trends are as a result of change in film density, light trapping or optical confinement and hence light

absorption of the films. Figure 2 (a) and Figure 2(b) show the dependence of band gap on film thickness of TiO_2 thin films.

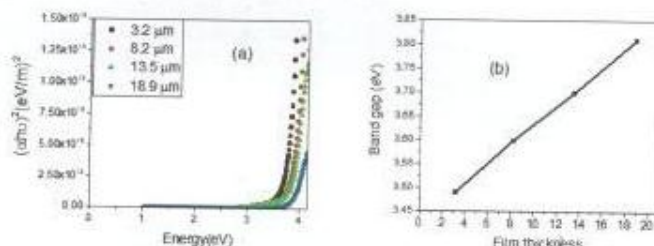


Figure 2. Band gap dependence on film thickness of TiO_2 thin films

Though band gap is an intrinsic property of a material which ordinarily should not be affected by film thickness, we found the optical band gap to increase slightly with film thickness due to dependence of absorption coefficient on film thickness [17]. The increase of band gap with film thickness is in agreement with similar observations by Granqvist et al. on TiO_2 films studied by combined reflectance, transmittance spectra, and Forouhi-Bloomer (FB) method [18]. The same observation with band gap was also reported for ZnO thin films [19]. Some investigations on temperature dependence of TiO_2 thin films on band gap also revealed that optical band gap increases with film thickness [20]. Band gap of the four films were estimated by Tauc's equation to be 3.5, 3.6, 3.7 and 3.8 eV. Though we found these optical band gaps to be a little higher than the theoretical values reported in literature, wide band gap lowers recombination in dye sensitized solar cells. The difference might be due to grain size, methods of preparation or impurities.

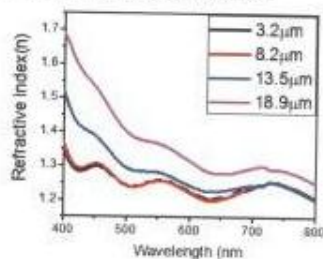


Figure 3. Refractive index versus wavelength of TiO_2 at different film thickness

The refractive indices of TiO_2 thin films of different thickness were calculated from the transmittance spectra and plotted in Figure 3.

From this figure, refractive indices increased with increase in film thickness, for example, the thickest film has the highest refractive index value whereas the thinnest film has the least value. The deposited TiO_2 thin film can be seen as a composite layer consisting of air and TiO_2 paste [21]. The volume ratio of air in the composite layer decreases with increase in film thickness [22]. Therefore the thicker layer is more compact, resulting in the increase in refractive index of the thin film. The dependence of refractive index with film thickness is in agreement with some previous similar investigations [23].

From the measured I-V by a 4 point-probe, electrical resistivity of the thin films was calculated and results are tabulated in Table 1.

Table 1. Resistivity and conductivity dependence on film thickness of TiO_2 thin films

Film Thickness (μm)	Resistivity (Ωcm)	Conductivity (Siemens cm^{-1})
3.2	3.39E-2	2.94E1
8.2	6.18E-2	1.61E1
13.5	1.353E-2	0.73E1
18.9	22.63E-2	0.44E1

We found that resistivity increased with film thickness. Conductivity of TiO_2 thin films is the reciprocal of resistivity. The values for conductivity are also tabulated in Table 1. It was found that conductivity decreased with increase in film thickness. The values obtained for both conductivity and resistivity are plotted in Figure 4.

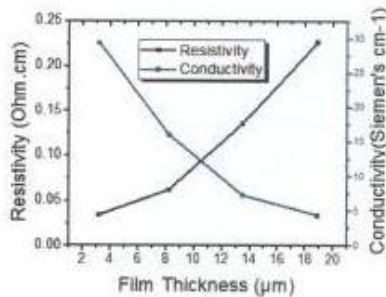


Figure 4. Resistivity and conductivity dependence on film thickness of TiO_2 thin films

As the film thickness increased, resistivity is raised from its least value to its highest value with the thickest film. Whereas for conductivity, increase in thickness decreased the value from its highest value to its least value with the thickest film.

4. Conclusion

TiO_2 thin films of different film thickness (3.2, 8.2, 13.5 and 18.9 μm) were deposited on glass substrate by screen printing method and annealed at 500°C for 30 minutes. Film thickness effect on optical and electrical properties of the films were investigated. UV-VIS-NIR spectrophotometer studies revealed that the films were highly transparent in the visible region and decreases with increase in film thickness. The transmittance values range between 62% and 78%. Reflectance and absorbance increased with film thickness. Reflectance varied between 25% and 15%. The computed band gap raised slightly from 3.5 to 3.8 eV with increase in film thickness. Refractive as determined from the studied spectra also increased with the film thickness showing its highest values at 400nm wavelength. Electrical resistivity was found to directly depend on film thickness while conductivity was the reverse.

References

- [1] M.E. Yang, Juan, Sen and J.M.F. Ferreira Hydrothd, *J. Am. Ceram. Soc.* 84(8), 2001, 1696-1706.
- [2] H. Ru-hin and G. Lian, *J. Mater. Res. Bull.*, 36, 2001, 1957-1965.
- [3] A. Otávio T. Patrocínio, Eucler B. Pamago, Roberto M. Paniago, Neyde Y. Murakami Iha, *Appl. Surf. Sci.* 254 (2008) 1874-1879.
- [4] Ibrahim A. Al-Homoudi, J.S. Thakur, R. Naik, G.W. Auner, G. Newaz, *Appl. Surf. Sci.* 253 (2007) 8607-8614.
- [5] M.R. Hoffmann, S.T. Martin, W. Choi, D.W. Bahnemann, *Chem. Rev.* 95 (1995) 69-96.
- [6] X.Z. Li, H. Liu, L.F. Cheng, H.J. Tong, *Environ. Sci. Technol.* 37 (2003) 3989-3994.
- [7] R. Mochiakh, F. Meriche, R. Kremer, R. Bensaha, B. Bouadine, A. Boudroua, *Optical Materials* 30 (2007) 645-651.
- [8] S.H. Jeong, J.K. Kim, B.S. Kim, S.H. Shim, B.T. Lee, *Vacuum* 76 (2004) 507-515.
- [9] Wenli Yang, Colin A. Wolden, *Thin Solid Films* 515 (2006) 1708-1713.
- [10] J. Rodriguez, M. Gomez, J. Ederth, G.A. Niklasson, C.G. Granqvist, *Thin Solid Films* 365(1), 119-125 (2000).
- [11] J.D. Deloach, C.R. Aita, *J. Vac. Sci. Technol. A* 16, 1963-1968 (1998).
- [12] H. Kangarlou, S. Rafizadeh, (Intech, Rijeka, 2012). ISBN: 978-953-51-0576-3. <http://www.intechopen.com/books/scanning-probe-microscopy-physical-property-characterization-nanoscale/influence-of-thickness-on-structural-and-optical-properties-of-titanium-oxide-thin-layers>.
- [13] M. Sreemany, S. Sen, *Mater. Res. Bull.* 42, 177-189 (2007).
- [14] F. Hamini, B. Bnouellou, Y. Bouachiba, F. Kerniche, A. Taabouche, M. Hemmissi, D. Lakhdari, *Journal of Engineering* 3(11), 21-28 (2013).
- [15] C. Kittel, "Introduction to Solid State Physics", 7th edition, John Wiley and Sons, New York 1996.
- [16] J. Rodriguez, M. Gomez, J. Ederth, G.A. Niklasson, C.G. Granqvist, *Thin Solid Films* 365(1), 119-125 (2000).
- [17] L. Miao, S. Tanemura, M. Tanemura, S.P. Lau, B.K. Tay, *J. Mater. Sci., Mater. Electron.* 18(1), 343-346 (2007).
- [18] S. Aksay and B. Atrioka, *Phys. Stat. Sol. (A)*, (2) 585-588.
- [19] Q.Y. Cai, Y.X. Zheng, P.H. Mao, R.J. Zhang, D.X. Zhang, M.H. Liu, L.Y. Chen, *J. Phys. D: Appl. Phys.* 43(44), 445302 (2010).
- [20] H.B. Wang, J.Y. Wang, J.H. Hong, Q.F. Wei, W.D. Gao, Z.F. Zhu, *J. Coat. Technol. Res.* 4(1), 101-106 (2007).
- [21] P.J. McMarr, J.R. Blanco, K. Vedam, R. Messier, L. Pilicere, *Appl. Phys. Lett.* 49, 328 (1986).
- [22] S. Lee, S. Choi, S.G. Oh, *J. Korean Phys. Soc.* 34(1), 93-96 (1999).
- [23] Z.J. Xu, F. Zhang, R.J. Zhang, X. Yu, D.X. Zhang, Z.Y. Wang, Y.X. Zheng, S.Y. Wang, H.B. Zhao, L.Y. Chen, *Applied Physics A Materials Science and Processing* Springer-Verlag Berlin Heidelberg 2013.